

ABSTRACT OF DISSERTATION

Aram Teymurazyan

The Graduate School

University of Kentucky

2008

PHOTON FLUX DETERMINATION FOR A PRECISION MEASUREMENT OF THE  
NEUTRAL PION LIFETIME

---

ABSTRACT OF DISSERTATION

---

A dissertation submitted in partial fulfillment of the  
requirements for the degree of Doctor of Philosophy in the  
College of Arts and Sciences  
at the University of Kentucky

By  
Aram Teymurazyan

Lexington, Kentucky

Director : Dr. Wolfgang Korsch, Professor of Physics and Astronomy

Lexington, Kentucky

2008

Copyright © Aram Teymurazyan 2008

## ABSTRACT OF DISSERTATION

### PHOTON FLUX DETERMINATION FOR A PRECISION MEASUREMENT OF THE NEUTRAL PION LIFETIME

The Jefferson Lab Hall B PrimEx Collaboration is using tagged photons to perform a 1.4% level measurement of the absolute cross section for the photo-production of neutral pions in the Coulomb field of a nucleus as a test of Chiral Perturbation Theory. Such a high precision pushes the limits of the photon tagging technique in regards to the determination of the absolute photon flux. A multifaceted approach to this problem has included measuring the absolute tagging ratios with a Total Absorption Counter (TAC) as well as relative tagging ratios with a Pair Spectrometer (PS), and determining the rate of the tagging counters using multi-hit TDC's and a clock trigger. This enables the determination of the absolute tagged photon flux for the PrimEx experiment with uncertainty of  $\sim 1.0\%$ , which is unprecedented.

In view of the stringent constraints on the required precision of the photon flux for this experiment, periodic measurements of the pair production cross section were performed throughout the run. In these measurements, both the photon energy and flux were determined by the Jefferson Lab Hall B tagger, and the electron-positron pairs were swept by a magnetic field and detected in the new 1728 channel hybrid calorimeter (HyCal). The pair production cross-section was extracted with an uncertainty of  $\sim 2\%$ , producing an agreement with theoretical calculations at the level of  $\sim 2\%$ . This measurement provided a unique opportunity to verify the photon flux determination procedure for the PrimEx experiment.

Finally, the photon flux determination procedure was used by the PrimEx collaboration to obtain the absolute normalization of the pion photo-production cross section, which allowed to extract neutral pion radiative width:  $\Gamma_{\pi^0 \rightarrow \gamma\gamma} = 7.93\text{eV} \pm 2.1\%(\text{stat.}) \pm 2.0\%(\text{sys.})$  (PRELIMINARY).

KEYWORDS : PrimEx, Neutral Pion Lifetime, Photon Tagging, Photon Flux, Lepton Pair Production

---

Student's Signature

---

Date

PHOTON FLUX DETERMINATION FOR A PRECISION MEASUREMENT OF THE  
NEUTRAL PION LIFETIME

By  
Aram Teymurazyan

---

Director of Dissertation

---

Director of Graduate Studies

---

## RULES FOR THE USE OF DISSERTATIONS

Unpublished dissertations submitted for the Doctor's degree and deposited in the University of Kentucky Library are as a rule open for inspection, but are to be used only with due regard to the rights of the authors. Bibliographical references may be noted, but quotations or summaries of parts may be published only with the premission of the author, and with the usual scholarly acknowledgements.

Extensive copying or publication of the dissertation in whole or in part also requires the consent of the Dean of the Graduate School of the University of Kentucky.

A library that borrows this dissertation for use by its patrons is expected to secure the signature of each user.

Name \_\_\_\_\_

Date

DISSERTATION

Aram Teymurazyan

The Graduate School

University of Kentucky

2008

PHOTON FLUX DETERMINATION FOR A PRECISION MEASUREMENT OF THE  
NEUTRAL PION LIFETIME

---

DISSERTATION

---

A dissertation submitted in partial fulfillment of the  
requirements for the degree of Doctor of Philosophy in the  
College of Arts and Sciences  
at the University of Kentucky

By  
Aram Teymurazyan

Lexington, Kentucky

Director : Dr. Wolfgang Korsch, Professor of Physics and Astronomy

Lexington, Kentucky

2008

Copyright © Aram Teymurazyan 2008



## ACKNOWLEDGEMENTS

I would like to express my gratitude and appreciation to Dr. Daniel Dale for his patient guidance and support during the years spent conducting the research and summarizing my work.

I would also like to thank members of the PrimEx collaboration for their useful discussions and guidance during my research at Thomas Jefferson National Accelerator Facility. In particular, I would like to thank Dr. David Lawrence for helping me to get acclimated to the PrimEx software, Dr. Mark Ito for the lengthy and useful discussions on design and the structure of the PFLUX software package at the early stages of its development, Dr. Dan Sober for sharing his expertise in analysis of TAC data and Dr. Eugene Pasyuk for providing his broad experience with analysis of data from tagged photon experiments at Jefferson Lab Hall-B.

I would like to thank my advisory committee Dr. Wolfgang Korsch, Dr. Steven Yates, Dr. Susan Gardner, Dr. Tim Gorringe and Dr. Arnold Stromberg for guidance, constructive criticism and comments.

Finally, I would like to thank my family and friends for their moral support and I would like to give a special thanks to Simona Felice for keeping me company and providing me with music during the long eight months of writing this dissertation.

## TABLE OF CONTENTS

ACKNOWLEDGEMENTS . . . . .	iii
LIST OF TABLES . . . . .	vi
LIST OF FIGURES . . . . .	viii
CHAPTER : 1 INTRODUCTION	1
1.1 Introduction . . . . .	1
1.2 Physics Motivation . . . . .	3
1.3 Previous Experiments . . . . .	5
1.4 The PrimEx Experiment . . . . .	9
CHAPTER : 2 EXPERIMENTAL SETUP	14
2.1 Beam Line Elements . . . . .	14
2.2 The TJNAF Hall-B Tagger . . . . .	18
2.3 The PrimEx Targets . . . . .	22
2.4 The Sweeping Dipole and the Pair Spectrometer . . . . .	22
2.5 The Hybrid Calorimeter (HyCal) . . . . .	26
2.6 Total Absorption Counter . . . . .	30
CHAPTER : 3 FLUX DETERMINATION IN PRIMEX	32
3.1 Principles of tagged yield normalization . . . . .	32
CHAPTER : 4 ABSOLUTE TAGGING RATIOS	37
4.1 Absolute calibration with total absorption counter . . . . .	37
4.2 TAC - Tagger coincidence and background determination . . . . .	38
4.3 Effects of incident electron beam intensity on absolute tagging ratios . . . . .	40
4.4 Effects of collimator size . . . . .	42
4.5 Effects of collimator position misalignment . . . . .	43
4.6 Effects of HyCal scraping due to beam mis-steering (uncollimated beam) . . . . .	45
4.7 Long and short term reproducibility with uncollimated beam . . . . .	49
4.8 Effects of the PS dipole field with collimated beam . . . . .	52
4.9 Absorption in the target . . . . .	54
4.10 Set of runs used to obtain the tagging ratios . . . . .	56
CHAPTER : 5 RELATIVE TAGGING RATIOS	59
5.1 Relative calibration with pair spectrometer . . . . .	59
5.2 PS-Tagger coincidence window and background determination . . . . .	59
5.3 Effect of Incident Electron Beam Intensity on Relative Tagging Ratios . . . . .	63
5.4 Run-to-Run Stability of Relative Tagging Ratios . . . . .	64
5.5 Inefficiency of Tagger . . . . .	67
5.6 Correction of Photon Flux for Affected Runs . . . . .	70

CHAPTER : 6 NUMBER OF PHOTONS PER RUN PER T-CHANNEL	75
6.1 Detector Rates, Electron Counting	75
6.2 Beam Trip Accounting	83
6.3 Photon flux per E-channel, ET matrix	88
6.4 Error Analysis	89
6.5 Summary	97
CHAPTER : 7 A PRECISION MEASUREMENT OF PAIR-PRODUCTION CROSS-SECTION	98
7.1 Motivation	98
7.2 Theoretical considerations	98
7.3 Measured quantities and data structure	102
7.4 Event selection	103
7.5 Simulation	109
7.5.1 Compton Background	112
7.5.2 Fiducial cuts	117
7.5.3 Energy losses in target and helium	119
7.6 Yield Extraction	120
7.7 Cross-Section	128
7.8 Error Evaluation and Summary	134
CHAPTER : 8 SUMMARY	142
APPENDIX A	
Error Propagation for a Ratio of Correlated Numbers	150
APPENDIX B	
Weighted Average	152
APPENDIX C	
DAQ Electronics and Trigger Setup	153
C.1 Lecroy 1877 multi-hit TDC	153
APPENDIX D	
Live2/Live1 problem	154
APPENDIX E	
PFLUX package, what it can do and how to use it	155
APPENDIX F	
Systematic Errors Due to Beam Instability	160
APPENDIX G	
Pair-Production Run Summary	163
BIBLIOGRAPHY	165
■	170

## LIST OF TABLES

1.1	Summary of major contributions to the projected experimental error for the PrimEx experiment. . . . .	13
4.1	Run summary of data used for tagging efficiency beam intensity ( <i>in</i> )dependence test. . . . .	42
4.2	Run summary of data used for tagging efficiency collimator size dependence test. . . . .	44
4.3	Run summary of data used for tagging efficiency collimator position dependence test. . . . .	45
4.4	Run summary of data used for the study of tagging efficiency dependence on the beam position. . . . .	49
4.5	Run summary of data used for tagging efficiency short term reproducibility test. . . . .	49
4.6	Run summary of data used for tagging efficiency long term reproducibility test. . . . .	51
4.7	Run summary of data used for tagging efficiency PS dipole field dependence test. . . . .	53
4.8	Run summary of data used for the study of photon absorption in the target with no collimator. . . . .	55
4.9	Run summary of data used for study of photon absorption in the target with 12.7 mm collimator. . . . .	58
4.10	The tagging ratios used in the photon flux determination. . . . .	58
5.1	Fit parameters for different T-counters, relative tagging ratio beam intensity ( <i>in</i> )dependence test . . . . .	64
5.2	The nominal values of $R_{rel}^i$ for runs with carbon target. . . . .	71
5.3	The correction factors for carbon target runs; groups 3 and 4. . . . .	72
5.4	The nominal values of $R_{rel}^i$ for runs with the lead target. . . . .	73
5.5	The correction factors for the lead target runs; groups 1 and 3. . . . .	74
6.1	Relative uncertainty in tagging efficiency due to HyCal scraping in case of beam mis-steering. . . . .	91
6.2	Relative uncertainty in tagging efficiency due to short and long term reproducibility. . . . .	91
6.3	Relative uncertainty in tagging efficiency due to collimator scraping in case of beam missteering . . . . .	92
7.1	Table of photon energy bins. . . . .	121
7.2	List of mean values and standard deviations of “tdiff” distributions for various T-channels. . . . .	122
7.3	Compton electron background scaling factor based on total photon flux in the run. . . . .	127
7.4	Total cross-section for pair-production calculated for the central values of the 10 energy bins. . . . .	129
7.5	Pair production cross-section integrated between $x_{min}$ and $x_{max}$ . . . . .	134
7.6	Statistical error for the $e^+e^-$ yields extracted between $x_{min}$ and $x_{max}$ . . . . .	135
7.7	Statistical error on the number of photons for pair-production runs. . . . .	136

7.8	Effect of detector resolution on $e^+e^-$ cross-section integrated between $x_{min} = 0.3$ and $x_{max} = 0.85$ .	138
7.9	Summary of errors integration region $0.3 < x < 0.85$ .	140
7.10	Summary of errors for integration region $0.4 < x < 0.76$ .	140
G.1	List of pair-production data runs.	163
G.2	Photon flux per energy bin for run # 5142.	163
G.3	Photon flux per energy bin for run # 5314.	164
G.4	Photon flux per energy bin for run # 5141.	164

## LIST OF FIGURES

1.1	The Primakoff effect . . . . .	2
1.2	The diagram for axial/triangle anomaly. . . . .	3
1.3	$\pi^0 \rightarrow 2\gamma$ decay width. The prediction of the axial anomaly is shown with a dashed line. The filled band denotes the result of NLO predictions with a $\pm 1\%$ error. The experimental results are for 1) the direct method [12]; 2,3 and 4) the Primakoff method [13, 14, 15]; 5) the expected error for the measurement by PrimEx collaboration arbitrarily projected on the LO prediction. . . . .	6
1.4	Differential cross-section for the pion photo-production on $^{12}_6C$ in forward direction. . . . .	12
2.1	Schematic of the PrimEx experimental setup beam line elements. . . . .	15
2.2	A typical photon beam profile obtained with the super-harp. . . . .	16
2.3	A typical electron beam profile obtained in a harp scan. . . . .	17
2.4	The overall schematic of the Hall B tagging system. The electron trajectories (red-dashed) are labeled according to the fraction of the incident energy that was transferred to the photon (blue-dashed). The schematic is adopted after Figure 1 in [25]. . . . .	19
2.5	Overlapping design of T-counters showing only the first 7 hodoscopes: (a) physical T-counters, (b) the T-channels defined through software coincidences. . . . .	21
2.6	Excitation curve measured for PS dipole magnet. . . . .	23
2.7	Layout of the pair spectrometer. Each arm consists of eight contiguous plastic scintillator hodoscopes in each row. . . . .	24
2.8	A schematic view of the pair spectrometer from the top showing the relative distances of the target, the magnet and the detectors. . . . .	24
2.9	A picture of the pair spectrometer hodoscopes mounted on aluminum frame, also the dipole and the exit vacuum window of the dipole on the background. . . . .	25
2.10	The lead tungstate ( $PbWO_4$ ) inset and the lead glass ( $PbO$ ) periphery of HyCal in a frame enclosure. . . . .	27
2.11	Schematic view of HyCal on the transporter. The shaded purple region depicts the lead tungstate modules and the light blue region depicts the lead glass modules. . . . .	28
2.12	HyCal energy resolution function obtained from “snake” calibration data. . . . .	29
2.13	Correlation of the photon energy and the TAC ADC counts. . . . .	31
4.1	The numbering scheme of the combined T-channels, only the first 7 counters are shown. . . . .	38
4.2	(a) Distribution of time differences for events reconstructed for Tagger and TAC. (b) a close up version of the first plot showing the $\pm 4.5$ ns timing window for coincidence events. . . . .	39
4.3	(top) Absolute tagging ratios plotted as a function of T-counter number for runs with different beam intensities, (bottom) The percent deviations from the mean for tagging ratio measurements made at different beam intensities for the first 11 T-counters. . . . .	41

4.4	(top) $R_{abs}$ measured for 3 different collimator sizes, (bottom) Percent deviation from the uncollimated value. . . . .	43
4.5	Collimator position vs. run number. . . . .	44
4.6	(top) $R_{abs}$ measured for five different collimator positions measured in inches. (bottom) Percent deviation from the measurement taken with collimator in its nominal position (7.02"). . . . .	46
4.7	(top) $R_{abs}$ measured for five different beam angles. (bottom) Percent deviation from the uncollimated value. . . . .	48
4.8	(top) $R_{abs}$ measured for four consecutive runs. (bottom) Percent deviation from the mean. . . . .	50
4.9	(top) $R_{abs}$ measured for three runs which were spread in time during our data taking. (bottom) Percent deviation from the mean. . . . .	52
4.10	(top) $R_{abs}$ measured for two runs which were taken with different settings of PS dipole magnet. (bottom) Percent deviation from the mean value. . . . .	54
4.11	(top) $R_{abs}$ measured for runs which were taken with target in and target out. (bottom) Percent deviation from the measurement obtained with physics target out; no photon collimation. . . . .	56
4.12	(top) $R_{abs}$ measured for runs which were taken with taget in and target out. (bottom) Percent deviation from the measurement obtained with physics target out; with photon collimation. . . . .	57
5.1	(a) Distribution of time differences for events reconstructed in Tagger and PS. (b) A close up of part (a) showing the $\pm 3.0$ ns timing coincidence window. . . . .	60
5.2	(a) Distribution of background events $Tagger \cdot PS$ timing spectra. (b) A close up of part (a) showing the 40ns timing window taken for measuring the background. . . . .	60
5.3	(a) Generated background timing spectra. (b) A close up of part (a) showing the $\pm 3$ ns coincidence region. . . . .	62
5.4	(a) Generated events, left background window. (b) Generated events, right background window. . . . .	63
5.5	(top) Measured $R_{rel}^i$ for T-counter #3 as a function of nominal electron beam current. (bottom) The percent deviations from the mean for tagging ratio measurements made at different beam intensities for the first eleven T-counters. . . . .	65
5.6	$R_{rel}^i$ measured for three different beam currents across the focal plane of the Tagger. The radiator thickness during these measurements was $2 \times 10^{-5} X_0$ . . . . .	66
5.7	Run-to-Run stability of $R_{rel}^{combined}$ - relative tagging ratio combined for eleven T-counters (a) carbon target. (b) lead target. . . . .	67
5.8	(a) Run dependence of $\sim \frac{\text{tagged } \gamma's}{\text{total } \gamma's}$ combined for eleven T-counters. (b) Run dependence of $\sim \frac{\text{total } \gamma's}{\text{total } e^{-}'s}$ combined for eleven T-counters. . . . .	68
5.9	$R_{relative}$ vs. beam current, combined for eleven T-counters and averaged for all runs with same current. The drop in relative tagging ratios reflects the change in number of electrons in the Tagger. . . . .	69
5.10	$\frac{\text{tagged } \gamma's}{\text{total } \gamma's}$ vs. beam current, combined for eleven T-counters and averaged for all runs with the same current, reflecting the loss of absolute efficiency of the Tagger. . . . .	70

5.11	$e^+e^-/e^-$ vs. beam current, combined for eleven T-counters and averaged for all runs with same current, reflecting the loss of absolute efficiency of the Tagger.	71
6.1	Trigger setup schematic	76
6.2	(a) Time spectrum of hits reconstructed for a single T-counter. (b) A close up of part (a) illustrating the drop off of the number of hits due to LIFO limit.	79
6.3	Timing spectrum of hits reconstructed for a single T-counter. These data were taken with clock triggers	81
6.4	DAQ dead-time per event for run 5159	84
6.5	A snap-shot of a screen in the experimental control room during the PrimEx run showing: beam current (green), $\gamma$ beam $X$ position after HyCal (blue), $\gamma$ beam $Y$ position after HyCal (light brown), $e^-$ beam $X$ position before radiator (dark brown) and $e^-$ beam $Y$ position before radiator (pink)	85
6.6	Fractional live-time for run 5159.	86
6.7	(a) Correlation of fractional live-time and number of electrons in T-counter #4. (b) A close up of part (a).	86
6.8	Number of counts in T-counter #5 per trigger recorded in a $7\ \mu\text{s}$ window for run 5159.	87
6.9	E - T matrix, showing the correlation of hits in T-counters to the hits in E-channels.	88
6.10	Distribution of number of hits per trigger event in T-counter #5 for run 5159.	95
7.1	Calculated energy spectrum of electrons in pair-production on $^{12}_6C$ for 5.46 GeV photons.	100
7.2	(a) Total cross-section for pair-production on $^{12}_6C$ for photons in energy region $4.91 - 5.46\text{GeV}$ . (b) Absolute cross-section for pair-production differential in fraction of energy of photon carried by the electron for $E_\gamma = 4.91\text{ GeV}$ and $E_\gamma = 5.46\text{ GeV}$ .	101
7.3	Schematic of a pair-production event as seen by the PrimEx experimental setup (top view).	102
7.4	(a) The various triggers and their absolute amount in a $e^+e^-$ production run #5142 are shown. (b) Only events triggered by HyCal-Tagger coincidence are selected.	104
7.5	(a) TDC spectra for various triggers in pair-production run #5142. (b) Reconstructed and calibrated (with respect to the HyCal-Tagger coincidence) times of various trigger signals.	105
7.6	The time difference between HyCal total sum signal and events reconstructed in the tagger. The $\pm 15\text{ns}$ coincidence window is also shown.	106
7.7	(a) The number of photons reconstructed in the Tagger per event. (b) The number of photons reconstructed in the Tagger per event that have the potential to be involved in the trigger.	107
7.8	(a) The energy difference for photons reconstructed in the Tagger with an accidental in the same T-channel. (b) The energy difference for photons reconstructed in the Tagger with accidental in different T-channel.	108
7.9	A visualisation of <i>GEANT4</i> model of PrimEx experimental setup. Pair-production events are also shown (top view).	110

7.10	(a) The distribution of $X$ and $Y$ coordinates and (b) the energy- $X$ position correlation for generated pair-production and Compton scattering events. . . . .	111
7.11	The distribution of $X$ coordinates for electrons with energies between 4.9 and 5.1 GeV (a) generated events and (b) data. . . . .	112
7.12	The distribution of $X$ coordinates for positrons with energies between 4.9 and 5.1 GeV (a) generated events and (b) data. . . . .	112
7.13	The distribution of $X$ and $Y$ coordinates for generated events in single arm regime: (a) $e^+e^-$ -production and (b) Compton events. . . . .	113
7.14	(a) Energy spectrum of the Compton electrons at PrimEx kinematics. (b) Distribution of $X$ -coordinates of Compton electrons at PrimEx kinematics and PS dipole field of $0.22 \text{ T} \times \text{m}$ . . . . .	114
7.15	(a) Energy spectrum and (b) distribution of $X$ -coordinates of generated Compton electrons and $e^+e^-$ pairs. . . . .	115
7.16	A sample distribution of $Z$ -coordinates of simulated pair-production vertices with respect to the center of the target. . . . .	116
7.17	Distribution of $Y$ coordinates of (a) electrons and (b) positrons from generated $e^+e^-$ -pairs. . . . .	117
7.18	(a) Distribution of $X$ coordinates for electrons and positrons with $ Y  > 5 \text{ cm}$ . (b) Energy spectrum of electrons and positrons from generated $e^+e^-$ -events where of $ Y  > 5 \text{ cm}$ . . . . .	118
7.19	(a) Energy losses of generated electron and positron pairs in the target and helium bag. (b) The correlation of energy losses and the $Z$ position of the conversion point in the target. . . . .	119
7.20	Energy spectrum of incident photons showing almost uniform distribution of $\gamma$ 's over the tagged energy range ( $4.874 - 5.494 \text{ GeV}$ ). . . . .	120
7.21	Tagger-HyCal time difference spectra for: (a) T-channel #3 and (b) for T-channel #12. . . . .	121
7.22	(a) Distribution of $X$ and $Y$ coordinates of clusters reconstructed in HyCal. (b) Correlation of energy and deflection in the magnetic field for clusters reconstructed in HyCal. . . . .	123
7.23	Distribution of $Y$ coordinates of clusters reconstructed in HyCal due to incident photons of various energy: (a) positrons and (b) electrons. . . . .	124
7.24	Distribution of $X$ coordinates of scattered photons in simulated Compton events. . . . .	125
7.25	(a) Energy spectra of the Compton electrons generated in a <i>GEANT4</i> simulation by incident photons in the energy range ( $4.874 - 5.494 \text{ GeV}$ ). The effect of detector resolution is shown by the blue histogram. (b) Energy distribution of Compton electrons for incident photon energy bins 2 and 10. . . . .	126
7.26	Energy spectrum of electrons before and after subtraction of Compton background. . . . .	127
7.27	Absolute cross-section for pair-production differential in fraction of energy of photon carried by the electron for $E_\gamma = 4.91 - 5.46 \text{ GeV}$ . The effect of energy losses in target and the helium bag is also shown as a blue histogram. . . . .	128
7.28	Percent deviation of the differential cross-section convoluted with energy losses and detector resolution from the calculated value. . . . .	130
7.29	Differential cross-section for $e^+e^-$ -production extracted on electron arm. . .	131

7.30 Differential cross-section for $e^+e^-$ -production run #5142 extracted on electron arm. . . . .	132
7.31 Differential cross-section for $e^+e^-$ -production run #5142 extracted on positron arm. . . . .	132
7.32 Differential cross-section for $e^+e^-$ -production run #5141 extracted on electron arm. . . . .	133
7.33 Differential cross-section for $e^+e^-$ -production run #5141 extracted on positron arm. . . . .	133
7.34 Simulated ratio of Compton and pair-production yields for $0.3 < x < 0.85$ . . . . .	137
8.1 The correlation between elasticity and the invariant mass for two clusters on the surface of HyCal at $\theta_{\pi^0} = 0.05^\circ$ . . . . .	145
8.2 Pion photo-production yield as a function of production angle: on (a) carbon target and (b) lead target. . . . .	148

## CHAPTER : 1 INTRODUCTION

### 1.1 Introduction

The Jefferson Lab Hall-B PrimEx collaboration is performing a  $\sim 1.4\%$  level measurement of the neutral pion lifetime which is calculable with high precision in the realm of low energy QCD and  $\chi$ PT as well as using a QCD sum rule approach [1, 2, 3].

The  $\pi^0$  is the lightest known hadron ( $m_{\pi^0} \simeq 135$  MeV) and primarily decays into two photons ( $\sim 98.8\%$  of the time) via the chiral anomaly. In 1951 H. Primakoff suggested the photo-production mechanism of neutral pions in the Coulomb field of a nucleus, *i.e.* the Primakoff effect (see Figure 1.1). Equivalent production ( $\gamma\gamma^* \rightarrow \pi^0$ ) and decay ( $\pi^0 \rightarrow \gamma\gamma$ ) mechanisms imply that the cross-section for the Primakoff process is inversely proportional to the neutral pion lifetime [4]. The PrimEx collaboration has used ( $\sim 5.5$  GeV) real photons to create  $\pi^0$ 's via the Primakoff effect. The energies and timing of the incident photons were determined using the Jefferson Lab Hall-B tagging facility. The two photons from the decay of the neutral pion were detected in a newly constructed state-of-the-art 1728 channel *Hybrid Calorimeter* (HyCal) thus allowing energy and angle reconstruction of the  $\pi^0$ . By measuring the differential cross-section for  $\pi^0$  photo-production on a nuclear target at small pion production angles one can extract the contribution of the Primakoff process, and thus the radiative width of the neutral pion.

The two photon decay of the  $\pi^0$  is a direct consequence of the axial anomaly. In the chiral limit, the radiative width  $\Gamma(\pi^0 \rightarrow 2\gamma)$  can be calculated exactly in leading order [5]. Recent theoretical calculations in  $\chi$ PT [2, 1] and in the QCD sum rule approach [3] predict a neutral pion radiative width of 8.1 eV ( $\pm 1.0\%$ ) and 7.93 eV ( $\pm 1.5\%$ ), respectively. Thus, a precision

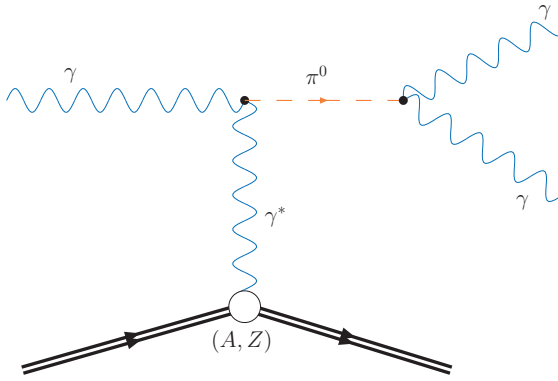


Figure 1.1: The Primakoff effect

measurement of the radiative width would arguably be one of the most fundamental tests of low energy QCD and Chiral Perturbation Theory possible with few GeV photons.

The present knowledge of the experimental value for  $\Gamma(\pi^0 \rightarrow 2\gamma)$  summarized in the PDG average, 7.84 eV ( $\pm 7.1\%$ ), is in reasonable agreement with theoretical predictions. However, the present quality of the experimental knowledge is not comparable with the precision of the theoretical prediction. The impressive precision of the theoretical results and the lack of an experimental value of comparable precision signify the need for a new, precise measurement of the neutral pion lifetime. The Jefferson Lab Hall-B PrimEx collaboration hopes to fill this important experimental gap by measuring the absolute cross-section for photo-production of  $\pi^0$ s in the Coulomb field of a nucleus with a precision of  $\sim 1.4\%$  and extracting the neutral pion lifetime. The largest contribution to the error on the pion lifetime extracted by the PrimEx experiment arises from the knowledge of the number of photons incident on the target. Such a high precision measurement of absolute cross-section demands knowledge of the absolute normalization of the experiment to  $\sim 1\%$  or better. The absolute photon flux determination,

which is the focus of the work presented in this dissertation, has not been previously attempted with such a precision at Jefferson Lab Hall-B, or to my knowledge anywhere else, which stresses the difficulty of the task.

## 1.2 Physics Motivation

The two-photon decay mode of the  $\pi^0$  manifests one of the most fundamental symmetry issues in QCD, namely, the anomalous breaking of a symmetry of the classical QCD Lagrangian by the quantum fluctuations of the quark fields coupling to a gauge field [5]. In the limit of massless quarks the QCD Lagrangian and all the orders of perturbation theory possess chiral symmetry; however, the presence of the axial-vector triangle diagram, such as shown on Figure 1.2, results in non-conservation of the axial-vector current associated with chiral transformation [6], [7]. This so-called axial anomaly, *i.e.*, non-conservation of the axial-vector current  $A_\mu^3 = \bar{q}I_3\gamma_\mu\gamma_5q$  due to coupling to the electromagnetic field, determines how a  $\pi^0$  decays to two photons. Here  $q = (u, d)$  and  $I_3$  is the third isospin generator.

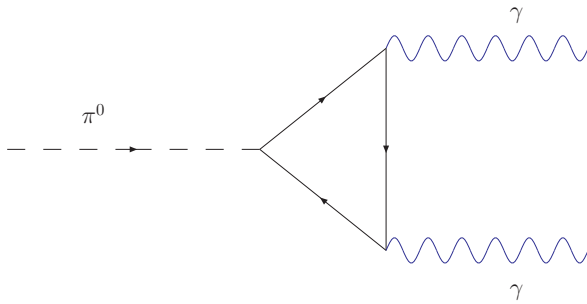


Figure 1.2: The diagram for axial/triangle anomaly.

In low energy QCD, assuming the  $u$  and  $d$  quark flavors are the only relevant degrees of

freedom, the form of the  $\pi^0$  decay amplitude predicted by the axial anomaly in the chiral limit ( $m_u = m_d = 0$ ) is [5], [8]:

$$A_{\gamma\gamma} = \frac{\alpha N_c}{3\pi F_\pi} \quad (1.1)$$

where  $\alpha$  is the electromagnetic coupling constant,  $N_c$  is the number of colors in QCD, and  $F_\pi$  is the pion decay constant.

This in turn gives a decay width of the neutral pion:

$$\Gamma_{\pi^0 \rightarrow \gamma\gamma} = \frac{m_\pi^3}{64\pi} |A_{\gamma\gamma}|^2 \quad (1.2)$$

where  $m_\pi$  is the mass of the  $\pi^0$ .

The decay amplitude given by Equation 1.1 is derived in the limit of massless quarks. However, as we know, the real world quark masses are not zero ( $m_u \sim 4$  MeV and  $m_d \sim 7$  MeV). This explicit breaking of the chiral symmetry leads to several corrections to the prediction by the axial anomaly. The most important one is a manifestation of the non-renormalization theorem of the anomaly due to Adler and Bardeen. It does not change the form of the amplitude given above, but only replaces the value of  $F_\pi$  in the chiral limit by the measured value determined from the  $\pi^+$  decay [1, 9, 10].

Taking the experimental value for  $F_{\pi^+} = 92.42 \pm 0.25$  MeV [11] and  $N_c = 3$ , the accepted value for the number of colors in the Standard Model, the theoretical prediction for pion decay width is  $\Gamma_{\pi^0 \rightarrow \gamma\gamma} = 7.729 \pm 0.044$  eV, where the uncertainty of  $\sim 0.6\%$  propagates directly from experiment.

A further correction to the  $\Gamma_{\pi^0 \rightarrow \gamma\gamma}$  due to the non-vanishing quark masses ( $m_u \neq m_d$ )

arises from the mixing of  $\pi^0$  with the  $\eta$  and  $\eta'$ . The magnitude of the effect has recently been evaluated by several authors with remarkable precision, who obtain neutral pion radiative widths of 8.08 eV ( $\pm 1.1\%$ ) [2], 8.1 eV ( $\pm 1.0\%$ ) [1] and 7.93 eV ( $\pm 1.5\%$ ) [3] respectively.

In conclusion, the theoretical value of  $\Gamma_{\pi^0 \rightarrow \gamma\gamma}$  is a fundamental prediction of low energy QCD, and in the chiral limit depends only on the number of colors. The higher order contributions to this decay (due to non-vanishing quark masses) are on the order of few percent and are calculable with a  $\sim 1\%$  accuracy. The current world average for the pion decay width carries an error bar of  $\sim 7.1\%$ , making a measurement of  $\Gamma_{\pi^0 \rightarrow \gamma\gamma}$  with a precision comparable to the theoretical uncertainties much needed. Thus the PrimEx experiment, with its proposed error bar of  $\sim 1.4\%$ , is one of the most fundamental measurements that can be performed with few GeV photons.

### 1.3 Previous Experiments

Figure 1.3 illustrates the state of the experimental knowledge of the pion radiative decay width, along with the projected goal of the PrimEx experiment. The predictions of the axial anomaly (see Equation 1.2) and the value obtained in NLO Chiral Perturbative Theory with the  $\pm 1\%$  theoretical uncertainty due to loop corrections are also shown on Figure 1.3. In the past, three experimental concepts have been used to measure the decay width of the  $\pi^0$  with varying degrees of success: the Direct Method,  $\gamma^* \gamma^*$ -collisions and the Primakoff method. A brief overview of each method, as well as a discussion of the state of the world data will be presented in this section.

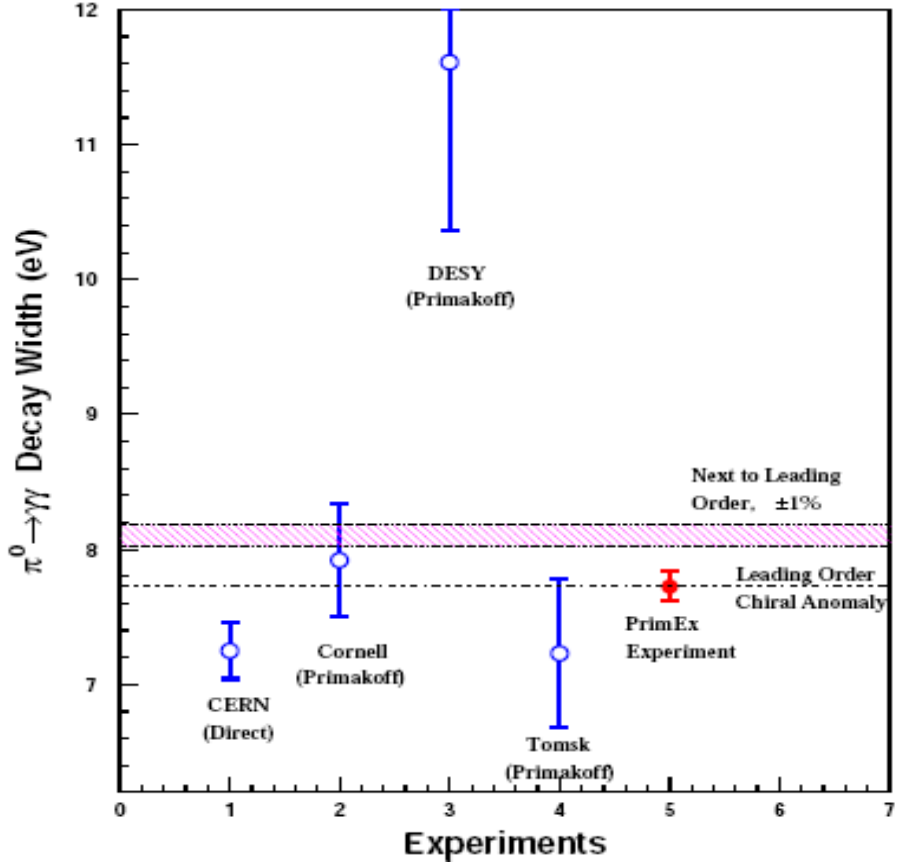


Figure 1.3:  $\pi^0 \rightarrow 2\gamma$  decay width. The prediction of the axial anomaly is shown with a dashed line. The filled band denotes the result of NLO predictions with a  $\pm 1\%$  error. The experimental results are for 1) the direct method [12]; 2,3 and 4) the Primakoff method [13, 14, 15]; 5) the expected error for the measurement by PrimEx collaboration arbitrarily projected on the LO prediction.

**Direct Method:** A measurement of the  $\pi^0$  lifetime can be made by observing the distance between the production and the decay points. Due to the short lifetime of the neutral pion,  $\tau \sim 10^{-16}$  s, one must utilize the relativistic time dilation to be able identify distinct production and decay points. This technique also requires a good knowledge of the energy distribution of the produced  $\pi^0$ s.

This so called Direct Method was used at the CERN PS in 1963 and reached a precision of 17% [16]. An improved version of this technique, a 1985 experiment at the CERN SPS, used a beam of 450 GeV protons incident on a tungsten foil to create relativistic  $\pi^0$ s. A second tungsten foil was used to convert the photons from the  $\pi^0 \rightarrow \gamma\gamma$  decay into electron-positron pairs. The distance between the two tungsten foils was made variable. For a large separation all of the pions decayed before the second converter foil and for small separation some of the pions decayed after the converter foil. By measuring the positron rates for three different foil distances ranging from 5 to 250  $\mu\text{m}$ , the group was able to extract a neutral pion radiative width of  $\Gamma_{\pi^0 \rightarrow \gamma\gamma} = 7.34 \text{ eV} \pm 2.45\% \pm 1.50\%$  [12]. The main contribution to the systematic error in this measurement comes from the uncertainty of the pion energy spectrum, which is assumed to be the arithmetic mean of the  $\pi^+$  and  $\pi^-$  spectra.

It should be noted that this experiment is the most precise measurement to date. However, the result reported by Atherton *et al.* [12] is three standard deviations away from the prediction of the recent theoretical calculations.

$\gamma^*\gamma^*$  collisions: A result for the neutral pion width has been published in 1988 by a group from DESY [17]. The  $\pi^0$ s were produced in electron-positron collisions, *i.e.*,  $e^+e^- \rightarrow e^+e^-\gamma^*\gamma^* \rightarrow e^+e^-\pi^0 \rightarrow e^+e^-\gamma\gamma$ . The collaboration used the Crystal Ball detector, made of 672 NaI crystals with 93% solid angle coverage to detect the photons from  $\pi^0$  decay created by quasi-real photons radiated by electrons and positrons from the collider. The systematic errors in this experiment arise from luminosity normalization, detector efficiencies, cosmic ray rejection and beam gas collisions. The Crystal Ball collaboration reported a pion decay width of  $\Gamma_{\pi^0 \rightarrow \gamma\gamma} = 7.7 \pm 0.5 \pm 0.5 \text{ eV}$

Note that the value obtained in this measurement agrees with the prediction of the axial anomaly and the PDG average, however it was not included in this average due to its large error [11].

**The Primakoff method :** A number of experiments utilized photo-production of neutral pions in the Coulomb field of a nucleus, *i.e.* the Primakoff effect, for pion lifetime measurement [13, 14, 15, 18].

In 1974 Brownman *et al.* measured the cross-section for the Primakoff process on several nuclei, with a bremsstrahlung photon beam of energy 4.4 and 6.6 GeV at Cornell, obtaining a pion decay width of  $\Gamma_{\pi^0 \rightarrow \gamma\gamma} = 8.02$  eV ( $\pm 5.24\%$ ). However this quoted uncertainty was questioned by [17, 19], who point out that it does not include contributions from luminosity or detection efficiency errors.

Groups from DESY [14] and Tomsk [15] used 1.5, 2.0 GeV and 1.1 GeV bremsstrahlung photon beams to measure the  $\pi^0$  decay width via the Primakoff effect, obtaining  $11.7 \pm 1.2$  eV and  $7.32 \pm 0.5$  eV respectively.

In conclusion, the theoretical prediction of  $\Gamma_{\pi^0 \rightarrow \gamma\gamma}$  based on the axial anomaly [5, 6] and the contributions from NLO (quark mass) terms provide a precision of  $\sim 1.0 - 1.5\%$  [1, 2, 3]. The experimental values of the  $\pi^0$  decay in general agree with the prediction of axial anomaly; however, the errors on individual measurements are quite large. There is also a noticeable scatter among the experimental values. The Direct Method provided the most precise measurement to date, but it is three standard deviations below that of the most recent theoretical calculations. The  $\gamma^* \gamma^*$ -collision method is susceptible to large systematic errors and the existing experiments utilizing the Primakoff effect yield results scattered in the range

of  $7.32 - 11.7$  eV. In view of the apparent deficiency in experimental data, a new measurement of the pion decay width with an uncertainty at the level of the theoretical calculations is required.

#### 1.4 The PrimEx Experiment

The PrimEx experiment was performed in Hall-B, of the Thomas Jefferson National Accelerator Facility. This experiment has a number of improvements and advantages over the previous measurements utilizing the Primakoff effect and brems-strahlung photon beams. In particular the Hall-B photon tagging facility provides: (1) a quasi-monochromatic tagged beam which enables a clean kinematical separation of the Primakoff mechanism from various background processes, also (2) the tagging technique, as will be shown, allows for a photon flux determination, *i.e.*, an absolute normalization of the cross-section, with a sub-percent precision. With error on the luminosity being one of the major issues in previous measurements using bremsstrahlung beams, a one percent photon flux determination is a major improvement. Also, the PrimEx collaboration has constructed a new state-of-the-art hybrid calorimeter which provides adequate energy and position resolution for a pion photo-production cross-section measurement at very forward angles ( $\sim 3 - 4^\circ$ ). The invariant mass and the pion angle are reconstructed by detecting, in the calorimeter, the two photons from the  $\pi^0 \rightarrow \gamma\gamma$  decay.

The PrimEx experiment used a quasi-monochromatic photons of energy  $\sim 4.9 - 5.5$  GeV from Jefferson Lab Hall-B photon tagging facility to produce neutral pions off of carbon and lead targets. By measuring the absolute cross-section for photo-production of  $\pi^0$ s in the Coulomb field of a nucleus, *i.e.*, the Primakoff effect, one can extract the two photon decay width of the neutral pion. For unpolarized photons, the differential cross-section for the

Primakoff process is [14]:

$$\frac{d^3\sigma_P}{d\Omega} = \Gamma_{\pi^0 \rightarrow \gamma\gamma} \frac{8\alpha Z^2}{m_{\pi^0}^3} \frac{\beta^3 E_\gamma^4}{Q^4} |F_{e.m.}(Q)|^2 \sin^2 \theta_{\pi^0} \quad (1.3)$$

where  $\Gamma_{\pi^0 \rightarrow \gamma\gamma}$  is the pion decay width,  $Z$  is the atomic number of the target nucleus,  $m_{\pi^0}$ ,  $\beta$ ,  $\theta_{\pi^0}$  are the mass, velocity and production angle of the pion,  $E_\gamma$  is the energy of the incident photon,  $Q$  is the momentum transfer to the nucleus, and  $F_{e.m.}(Q)$  is the nuclear electromagnetic form factor corrected for outgoing pion final state interactions.

The Primakoff effect is not the only mechanism for the  $\pi^0$  photo-production in the few GeV energy region; some care must be taken to properly identify and subtract the contributions from the competing processes. The full cross-section for pion photo-production in the forward direction (up to  $\sim 3 - 4^\circ$ ) is given by:

$$\frac{d^3\sigma}{d\Omega} = \frac{d^3\sigma_P}{d\Omega} + \frac{d^3\sigma_C}{d\Omega} + \frac{d^3\sigma_I}{d\Omega} + \sqrt{\frac{d^3\sigma_P}{d\Omega} \frac{d^3\sigma_C}{d\Omega}} \cos(\phi_1 + \phi_2) \quad (1.4)$$

here  $\frac{d^3\sigma_C}{d\Omega}$  is the nuclear coherent cross section[20, 21, 22]:

$$\frac{d^3\sigma_C}{d\Omega} = C \cdot A^2 |F_N(Q)|^2 \sin^2 \theta_{\pi^0} \quad (1.5)$$

and  $\frac{d^3\sigma_I}{d\Omega}$  is the incoherent cross section [23, 24]:

$$\frac{d^3\sigma_I}{d\Omega} = \xi A (1 - G(Q)) \frac{d^3\sigma_N}{d\Omega} \quad (1.6)$$

where  $A$  is the nucleon number,  $F_N(Q)$  is the form factor for the distribution of nuclear matter (corrected for pion final state interactions), the factor  $C \sin^2 \theta_{\pi^0}$  in Equation 1.5 is the square

of the spin and isospin independent part of the  $\pi^0$  photo-production amplitude on a single nucleon,  $\xi$  is the absorption factor for incoherently produced pions,  $(1 - G(Q))$  is a suppression factor, due to the Pauli exclusion principle, that reduces the cross section at small momentum transfers, and  $\frac{d^3\sigma_N}{d\Omega}$  is the cross-section for  $\pi^0$  photo-production on a single nucleon. The  $\phi_1$  in Equation 1.4 is the phase between the Primakoff and nuclear coherent amplitudes and the  $\phi_2$  is the phase shift of the outgoing pion due to final state interactions.

Figure 1.4 shows the angular behavior of the electromagnetic and nuclear  $\pi^0$  photoproduction cross-sections for  $^{12}_6C$  for forward angles and  $E_\gamma = 5.6$  GeV [20]. The amplitudes on this plot are normalized to data from [13].

The Primakoff process has distinct signatures which allow its separation from the background processes using kinematic considerations. For spin zero nuclei, the Primakoff cross-section: 1) is zero for pions emitted along the incident photon direction, 2) is forward peaked with a sharp maximum at  $\theta_{\pi^0} \sim m_{\pi^0}^2/2E_{\pi^0}^2$ , 3) is proportional to  $Z^2$  of the target nucleus and 4) has a peak value proportional to  $E_\gamma^4$ . The cross-section for coherent photo-production of  $\pi^0$ s off of nuclei is also zero at  $\theta_{\pi^0} = 0$  for spin zero targets, however it has a broad maximum outside of the angular region of the Primakoff process, and falls slower at larger angles (see Figure 1.4). The cross-section for incoherent pion production has a relatively smaller contribution and extends to even larger angles [23]. The PrimEx collaboration has taken an empirical approach to determine the contributions of coherent and incoherent mechanisms in the Primakoff region ( $\theta_{\pi^0} < \sim 0.8^\circ$ ). The data have been recorded at larger angles, up to  $4^\circ$ , enabling the extraction of the unknown parameters in the production mechanisms [21, 22, 23]. An invariant mass cut has been employed to suppress the accidental and correlated multi-photon backgrounds. Finally, data has been taken on two targets ( $^{12}_6C$  and  $^{208}_{82}Pb$ ) to verify

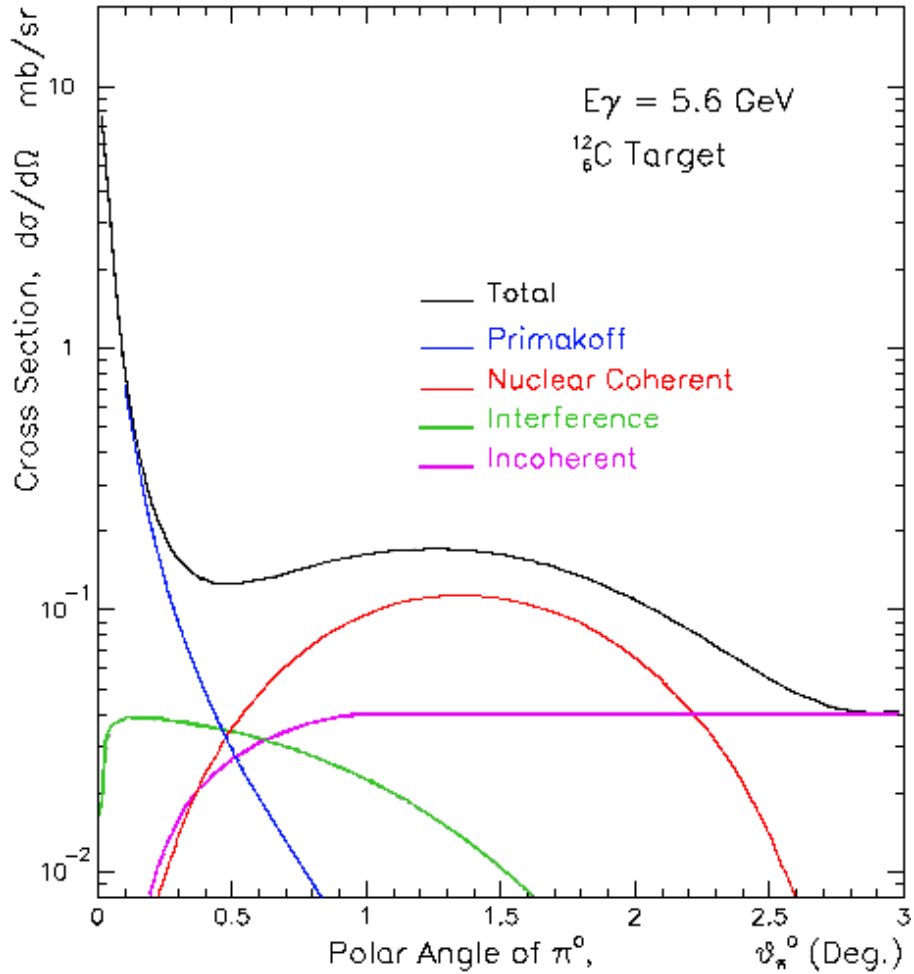


Figure 1.4: Differential cross-section for the pion photo-production on  $^{12}_6C$  in forward direction.

the  $Z$  dependence of the Primakoff cross-section and study the systematic effects of nuclear contributions to the Primakoff peak.

The ambitious goal, to measure the neutral pion lifetime with a precision of  $\sim 1.4\%$ , set out by the PrimEx collaboration demands an absolute normalization of the cross-section with an unprecedented precision of 1% or better (see Equation 3.1). Table 1.1 lists the major contributions to the projected error for the PrimEx experiment, and as one can see, the uncertainty

in the photon flux is the dominant component. To stress the importance of the special care required in the determination of the absolute normalization for the PrimEx experiment, it is worth noting that the cross-section normalization has been one of the major sources of systematic errors for previous experiments utilizing the Primakoff effect and bremsstrahlung photon beams.

Table 1.1: Summary of major contributions to the projected experimental error for the PrimEx experiment.

Statistical	0.40%
Target thickness	0.70%
Photon flux	1.00%
$\pi^0$ detector acceptance and misalignment	0.40%
Background subtraction	0.20%
Beam energy	0.10%
Distorted form factor calibration errors	0.40%
TOTAL ERROR (added in quadrature)	1.40%

The work presented in this dissertation describes the photon flux determination procedure for the PrimEx experiment, which achieved a sub-percent precision. It involves absolute calibration of the JLab Hall-B photon tagging facility against a total absorption counter, insitu relative monitoring of the photon flux with a pair spectrometer and an innovative approach of using multi-hit TDCs in conjunction with beam intensity unrelated clock triggers to measure the flux in the photon tagging system. Finally, the flux determination procedure is verified by measuring the absolute cross section of a well known QED process,  $e^+e^-$ -pair production.

## CHAPTER : 2 EXPERIMENTAL SETUP

### 2.1 Beam Line Elements

In order to fulfill the systematic uncertainty requirements of the PrimEx experiment, the following aspects of the beam-line instrumentation were considered and addressed:

- Electron beam energy, position, intensity and energy stability control.
- $\gamma$  beam intensity, position and profile control.
- Background control.
- Linearity and stability of the monitors with beam intensity.

Figure 2.1 presents detailed schematic of the PrimEx experimental setup. At Jefferson Lab Hall-B, photons are produced in a bremsstrahlung radiator by a 5.76 GeV electron beam and then pass through a 6 cm gap of the pole of the tagger magnet. In addition to the 8.6 mm collimator, the beam-line was outfitted with a 12.7 mm collimator, which served as the primary collimator for PrimEx. A  $0.73 \text{ T} \times \text{m}$  permanent magnet was introduced into the beam line for the purpose of removing charged particles created by the photon beam scraping the inside of the collimator. After the photon beam leaves the pole of the tagger magnet it travels through a 7.5 cm diameter beam pipe until it reaches the PrimEx physics target approximately 6.5 meters downstream of the radiator. The beam-line section upstream of and including the pair production luminosity monitor magnet was in vacuum, and the section from the exit window of the luminosity monitor dipole to the face of the calorimeter was enclosed in a helium bag.

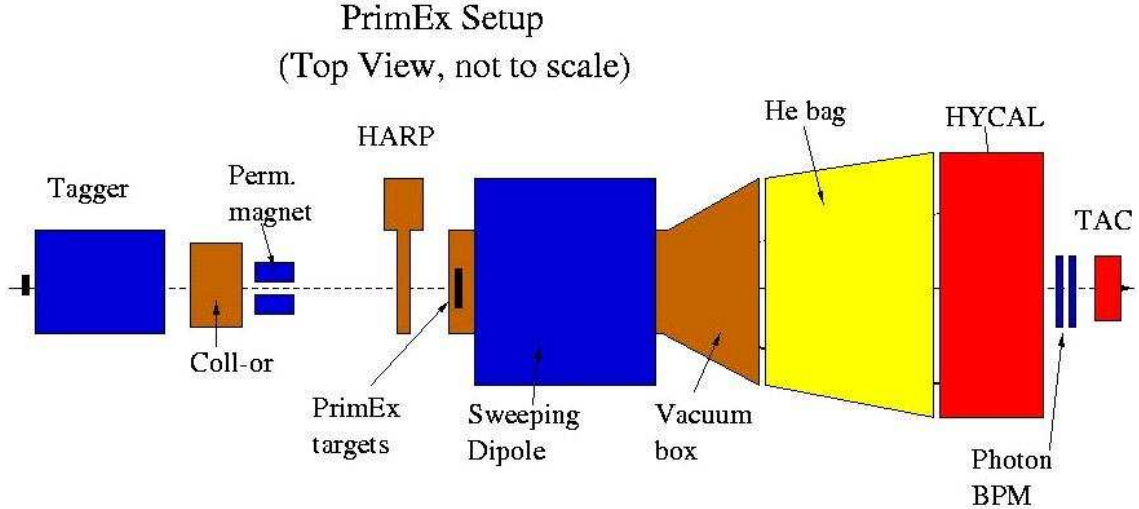


Figure 2.1: Schematic of the PrimEx experimental setup beam line elements.

A photon beam is established in Hall-B by centering the electron beam in the two beam position monitors (BPM) upstream of the radiator, and then checking the position of the post-bremsstrahlung beam on the beam dump screen below the tagger magnet. A super-harp scanner was installed in front of the Primakoff production targets to provide photon beam position and profile control at the position of the physics target (see Figure 2.2).

The main components of the super-harp are a fork with three tungsten wires, a stepper motor with an accuracy of motion of  $\sim 10 \mu\text{m}$  and a particle detector to record the rates of the secondary particles created by insertion of the tungsten wires into the photon beam. The scintillator telescopes of the Pair Spectrometer, which is described in detail in Section 2.4, are used as a particle detector for the super-harp. The fork supporting the tungsten wires is positioned and moves at  $45^\circ$  with respect to the horizontal axis and in the plane perpendicular to the beam line. The distance between the two arms of the fork is one inch. Three wires

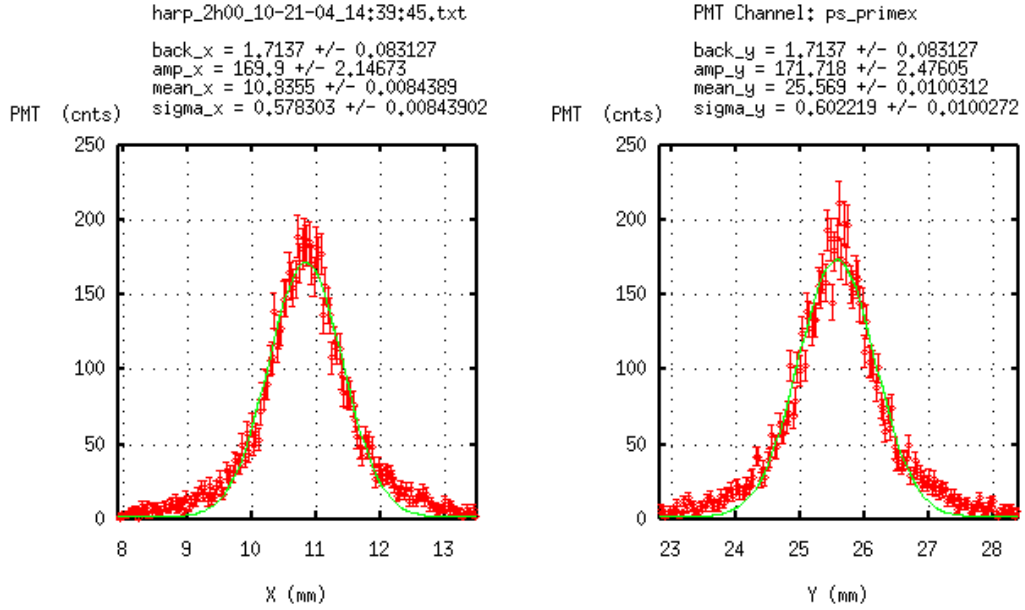


Figure 2.2: A typical photon beam profile obtained with the super-harp.

are positioned between the arms in such a way that the first and the third wires are vertical and move in the horizontal direction across the beam. The intermediate wire is horizontal and moves in the vertical direction when the fork advances at  $45^\circ$ . When a wire crosses the beam, beam particles scatter from the wire or produce  $e^+e^-$  pairs, which are analyzed in the magnetic field of the dipole magnet and detected in the scintillator telescopes in singles or coincidence mode. Using the information from the encoder, one can reconstruct the vertical and horizontal beam profile distributions.

Electron beam scans at the position of the radiator were carried out routinely with a device much like the super-harp (it uses thinner tungsten wires) and have shown no measurable halo (see Figure 2.3).

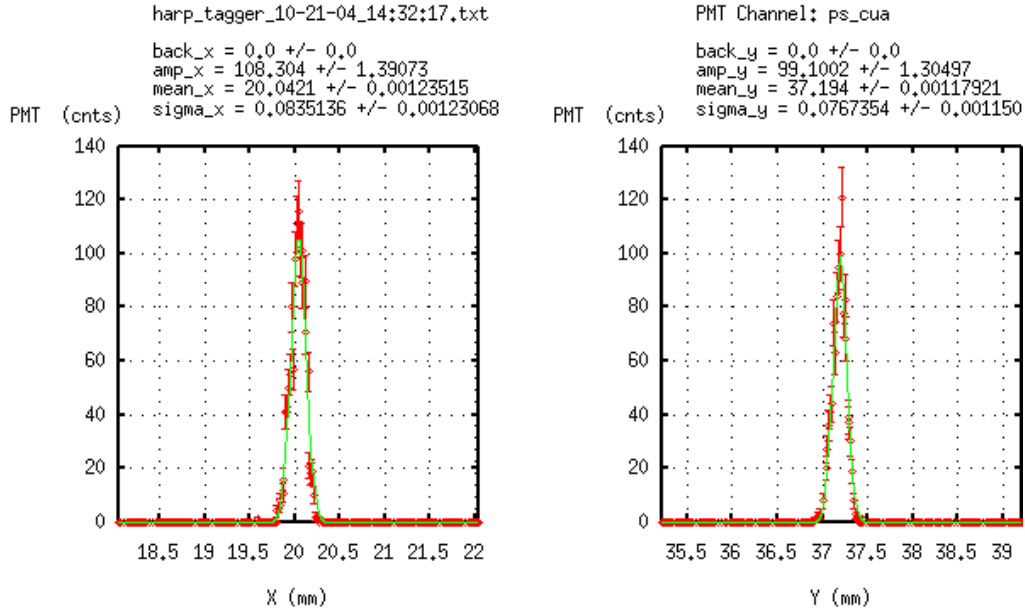


Figure 2.3: A typical electron beam profile obtained in a harp scan.

The main elements of the beam line for the PrimEx experiment include (1) the Jefferson Lab Hall-B photon tagger, (2) a collimator, (3) a permanent magnet, (4) super-harp scanner located in front of the physics targets, (5) 5% radiation length solid targets ( $^{12}C$  and  $^{208}Pb$ ), (6) a pair production luminosity monitor, which is located just downstream of the physics targets, (7) a hybrid electromagnetic calorimeter containing a high resolution insertion in the central region near the beam and (8) a total absorption lead-glass counter used in determination of the absolute normalization of the photon flux.

The subsequent sections describe in detail the Jefferson Lab Hall-B photon tagger, the pair production luminosity monitor, the novel electromagnetic hybrid calorimeter and the total absorption counter.

## 2.2 The TJNAF Hall-B Tagger

The Jefferson Lab (JLab) Hall-B photon experiments utilize the well known bremsstrahlung photon tagging technique to measure the energy and time information of incident photons in real photon induced reactions [25]. The electron beam of initial energy  $E_0$  (in the case of PrimEx  $E_0 = 5.76$  GeV) is incident upon a thin ( $3 \times 10^{-4}$ ,  $10^{-4}$  or  $10^{-5}$  rad. length) bremsstrahlung converter foil (the “radiator”). The electron loses energy in the electromagnetic field of the nucleus and in the process emits an energetic photon (braking radiation). The number of photons with energies in the interval  $k — k + dk$  is directly proportional to the  $Z^2$  of the radiator and is inversely proportional to the energy  $k$  of the photons [26]. Due to the relatively small mass of the electron the recoil energy transferred to the nucleus is negligible, so one can effectively write the energy conservation for the process as:

$$E_\gamma = E_0 - E_e \quad (2.1)$$

where  $E_\gamma$  is the energy of the bremsstrahlung photon and  $E_e$  is the energy of the secondary electron. The energy  $E_0$  of the electron incident on the radiator is defined by the accelerator, hence by measuring the energy of the post-bremsstrahlung electron one can determine the energy of the photon.

At energies above a few MeV both the secondary electrons and the radiated photons travel along the direction of the incident electron beam. The characteristic angle of the cone of photons is  $\theta_c = m_e c^2 / E_0$ . Even at the lowest possible energies at JLab ( $\sim 800$  MeV) the  $\theta_c$  is on the order of 1 mr.

Figure 2.4 is a schematic representation of the Jefferson Lab Hall-B photon tagger (the “tagger”). The main components of the tagger are a thin ( $\sim 10^{-4}$  rad. length) bremsstrahlung radiator, a dipole magnet capable of full field of 1.75 T and two rows of plastic scintillator hodoscopes, “E” – and “T” – counters (energy and timing counters).

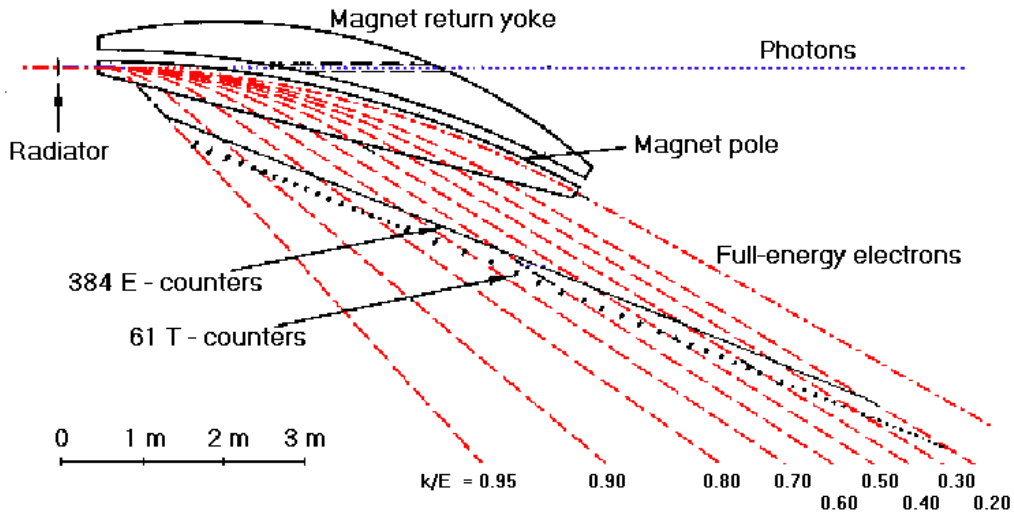


Figure 2.4: The overall schematic of the Hall B tagging system. The electron trajectories (red-dashed) are labeled according to the fraction of the incident energy that was transferred to the photon (blue-dashed). The schematic is adopted after Figure 1 in [25].

The photons produced in the radiator continue essentially straight ahead through the tagger, toward the target further downstream in the experimental hall. A collimation system, a 12.7 mm collimator in conjunction with a 0.73 T permanent magnet, is positioned just downstream of the tagger and centered on the photon beam line in order to further define the photon beam. Meanwhile, the electrons are separated from the photons by the tagger dipole magnet. The field setting of the magnet is adjusted to the incident beam energy to allow full energy

electrons which do not interact with the radiator to follow a circular arc inside the curved edge of the magnet pole and are directed into a shielded beam dump below the floor of the experimental hall.

The energy-degraded electrons are detected in the E- and T- counters that lie along a flat focal plane downstream from the straight edge of the magnet. The E-counters make-up a plane of 384 overlapping 4 mm thick scintillators. The E-counters are designed to have a variable width (from 6 mm to 18 mm) to cover approximately constant energy intervals of  $3 \times 10^{-3} E_0$ . Using the overlapping nature of the E-counters, 767 fine energy channels (E-channels) of width  $10^{-3} E_0$  are defined through software coincidences of adjacent E-counters [25].

In order to properly associate a tagged electron with a related downstream event, a timing resolution of 300 ps or better is provided by a row of T-counters located directly under the row of the E-counters. There are 61 T-counters in total. Each detector is 2 cm thick plastic scintillator read out with a photomultiplier at each end of each scintillator. T-counters have overlapping acceptances (of a few mm) to ensure that there are no inter-counter gaps. The overlapping design of the T-counters gives rise to 121 non-overlapping T-channels which are defined through a software coincidence for two adjacent detectors. The numbering schemes for T-counters and T-channels are presented on Figure 2.5<sup>1</sup>.

The focal plane of the Tagger is divided into two groups of T-counters. The first group of 19 counters covers the photon energy range from 77% to 95% of the incident electron energy, and the group of 42 remaining wider counters covers the range from 20% to 77%. The size of individual T-counters compensates for the  $1/k$  behavior of the bremsstrahlung cross-section. The width of each T-counter is chosen in such a fashion that it enables approximately the

---

<sup>1</sup>The same numbering scheme is applied to E-counters and E-channels.

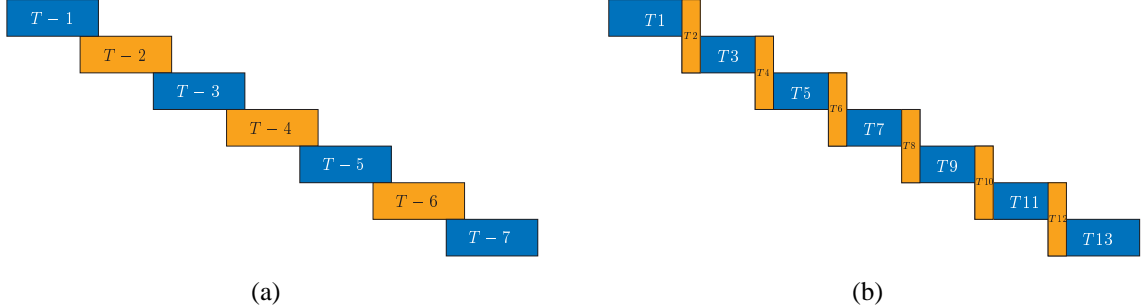


Figure 2.5: Overlapping design of T-counters showing only the first 7 hodoscopes: (a) physical T-counters, (b) the T-channels defined through software coincidences.

same counting rate for each detector within the same group. When all 61 T-counters are used, the total tagging rate can be as high as 50 MHz for the whole focal plane. The high-energy counters T1-T19, are proportionally smaller, and allow a tagging rate of up to 50 MHz in this region alone [25]. The PrimEx experiment used only the counters T1 through T11.

The use of the Jefferson Lab Hall-B photon tagging facility gives PrimEx multiple advantages over the previous experiments that were based on the Primakoff effect [13, 14, 15, 18]. As has been discussed in Section 1.1, the peak value and the angular distribution of the Primakoff cross section are strongly dependent on the energy of the  $\pi^0$ . The determination of the tagged photon flux on the experimental target is also enabled by the tagger (see Chapter 3). Thus a more accurate knowledge and control of the photon beam energy and the luminosity provides PrimEx with a greater control over systematic errors.

### 2.3 The PrimEx Targets

The PrimEx experiment used 5% radiation length  $^{12}C$  and  $^{208}Pb$  as  $\pi^0$  production targets. Using different targets in the experiment allows one to explore the  $Z$  dependence of the  $\pi^0 \rightarrow \gamma\gamma$  cross section and to better understand the physics backgrounds. When selecting the targets, things like purity of the target, knowledge of nuclear form factors and the ground state angular momentum are considered. For the sake of better understanding the systematics of the calibration reactions (pair production and Compton scattering) a 0.5% radiation length  $^9Be$  foil was installed on the target frame. The majority of the PrimEx  $\pi^0$  data were taken on the  $^{12}C$  target. A careful study of these targets (see [27]) has enabled the determination of the number of atoms per  $cm^2$  in the targets with an exceptional sub-percent precision. The number of atoms per unit area ( $N_{atoms}$ ) for the carbon target is  $1.066 \times 10^{23} \text{ cm}^{-2}$  ( $\pm 0.053\%$ ) and is  $4.569 \times 10^{21} \text{ cm}^{-2}$  ( $\pm 0.304\%$ ) for the  $^9Be$  target.

### 2.4 The Sweeping Dipole and the Pair Spectrometer

The **Pair Spectrometer (PS)** was constructed for the purpose of monitoring the relative tagged photon flux (for details please see Chapter 3). It consists of a  $1.6 \text{ T} \times \text{m}$  dipole magnet and two symmetric arms on each side of the beam line (beam left and beam right) and is designed to detect  $e^+e^-$  pairs produced in the physics target (the  $\pi^0$  production targets) by photons over the full tagged photon energy range of the experiment.

The dipole magnet was carefully mapped using an NMR probe. Using the information from these measurements an excitation curve was obtained (see Figure 2.6). A simple linear fit to the data gives the following current ( $I$ ) – field ( $B$ ) dependence:

$$I(A) = -0.6657 - 0.1537 \times B(\text{Gauss}). \quad (2.2)$$

A fast-degaussing procedure was developed which allows one to achieve a field reproducibility of better than  $10^{-4}$  Gauss.

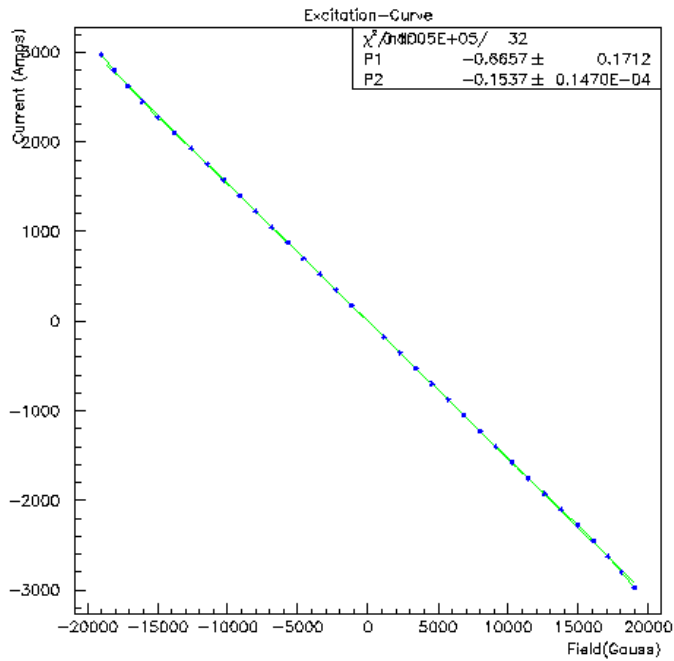


Figure 2.6: Excitation curve measured for PS dipole magnet.

Each arm of the pair spectrometer has two rows (front and back) of scintillator hodoscopes in sets of 8 making 32 detectors in total. Schematic views of the pair spectrometer are shown in Figures 2.7 and 2.8. The front detectors are located 140.1 cm downstream from the center of the dipole magnet and the back detectors are located 46.4 cm downstream from the front detectors (as shown on Figure 2.8). The distance of the middle of the detector plane of the front hodoscopes to the beamline is 25.6 cm and the distance of the middle of the detector plane of

back hodoscopes to the beamline is 34.0cm. The planes of front and back detectors make up a  $10.3^\circ$  angle with  $XY$  coordinate plane perpendicular to the beamline. The scintillators of the front hodoscopes are  $2.4 \times 7.5 \times 0.5$  cm $^3$  in size and are made of *BC420* plastic.

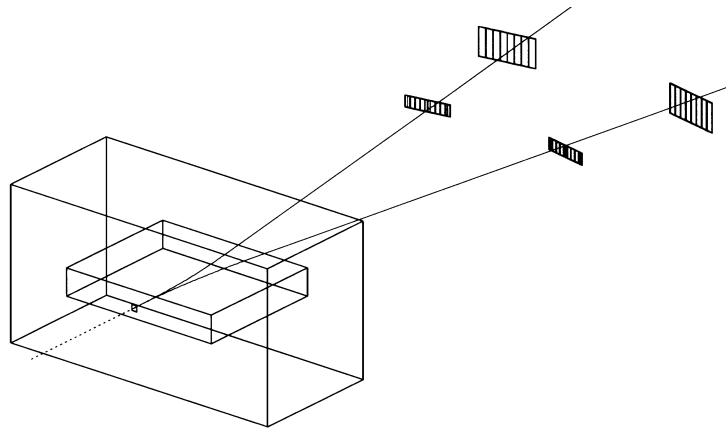


Figure 2.7: Layout of the pair spectrometer. Each arm consists of eight contiguous plastic scintillator hodoscopes in each row.

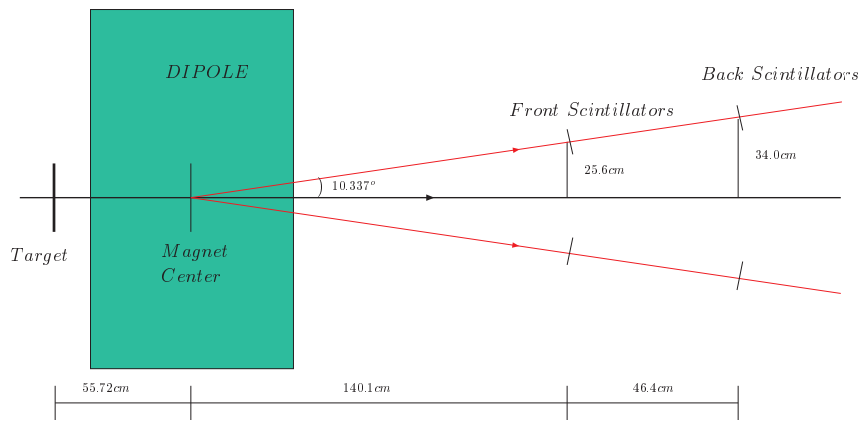


Figure 2.8: A schematic view of the pair spectrometer from the top showing the relative distances of the target, the magnet and the detectors.

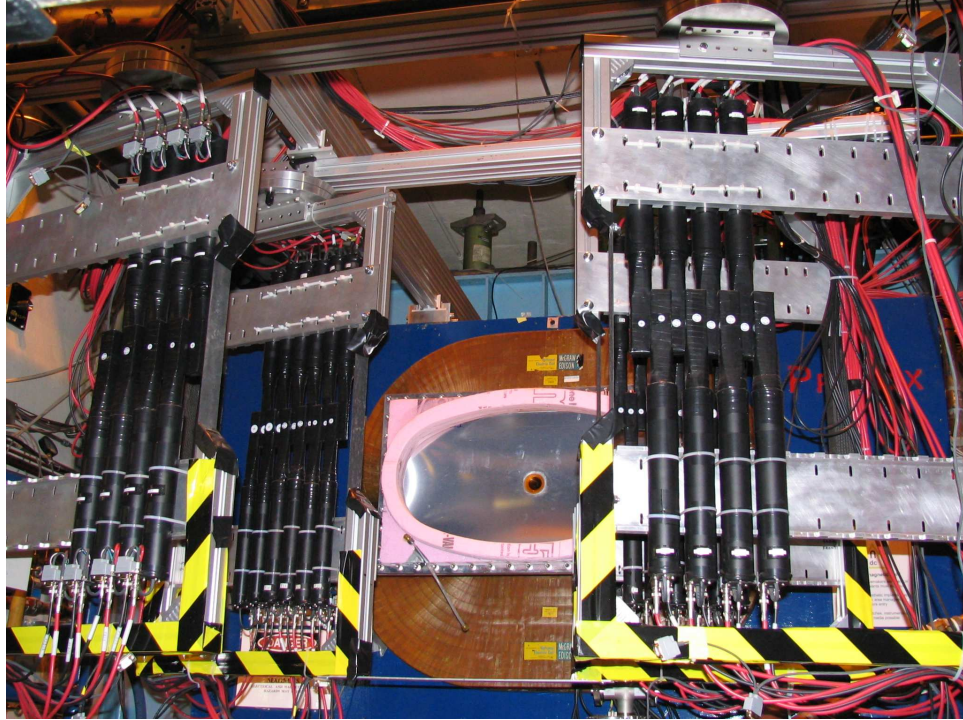


Figure 2.9: A picture of the pair spectrometer hodoscopes mounted on aluminum frame, also the dipole and the exit vacuum window of the dipole on the background.

The back detectors are  $3.1 \times 9.3 \times 2.0 \text{ cm}^3$  in size. The front scintillators were chosen to be thinner than the back scintillators to minimize the change in the trajectory of electrons and positrons due to multiple scattering. The relative widths of the detectors were chosen in such a way that to each  $i$ -th front detector correspond three back detectors  $i-1$ ,  $i$  and  $i+1$ . Each front and back detector was wrapped into four and five layers of  $\mu$ -metal, respectively, in order to shield them from the fringe field of the dipole magnet. A pair spectrometer event is defined by requiring a 4-fold timing coincidence between the two arms of the pair spectrometer (left-front  $\cdot$  left-back  $\cdot$  right-front  $\cdot$  right back) which greatly reduces the rate of accidental coincidences.

The dipole magnet is simultaneously a sweeping magnet used to make sure that during the production data taking we do not get charged particle background in the calorimeter. The scintillator hodoscopes are also used in the beam profile measurements with the super-harp.

## 2.5 The Hybrid Calorimeter (HyCal)

The two photons from the  $\pi^0$  decay are detected in a highly segmented **Hybrid Calorimeter (HyCal)**. HyCal is a two-dimensional matrix of radiators (see Figure 2.10) designed to provide precise measurements of position and energy of the detected particles. The inner part of the calorimeter is a  $34 \times 34$  array of 1152 lead–tungstate ( $PbWO_4$ ) crystals of dimensions  $2.075 \times 2.075 \times 21.2$  cm $^3$  with a  $(4.15 \times 4.15$  cm $^2$ ) central hole left open to enable the primary photon beam to pass through. The  $PbWO_4$  crystals have a radiation length of 0.89 cm and a Molière radius of 2.20 cm. The matrix of lead–tungstate crystals is surrounded by six layers of lead–glass ( $TF1$ ) modules. Each of 576 lead–glass modules is of dimensions  $3.815 \times 3.815 \times 34$  cm $^3$ . The  $TF1$  lead–glass has a Molière radius of 4.70 cm and a radiation length of 2.74 cm. The HyCal is  $119.0 \times 119.0$  cm $^2$  in the direction transverse to the beam and it is located about 7.32 meters downstream of the  $\pi^0$  production target.

In order to extract the Primakoff amplitude at the energies (4.87 – 5.49 GeV) used for this experiment, it is necessary to have sufficient resolution for the pion production angle. The high resolution crystal insertion of the HyCal detector is designed to improve the pion angular resolution. This resolution depends strongly on the decay photon energy and the position accuracy of the calorimeter. The dimensions of the modules in the direction transverse to the beam are optimized with respect to the Molière radius, so that the energy leakage into adjacent

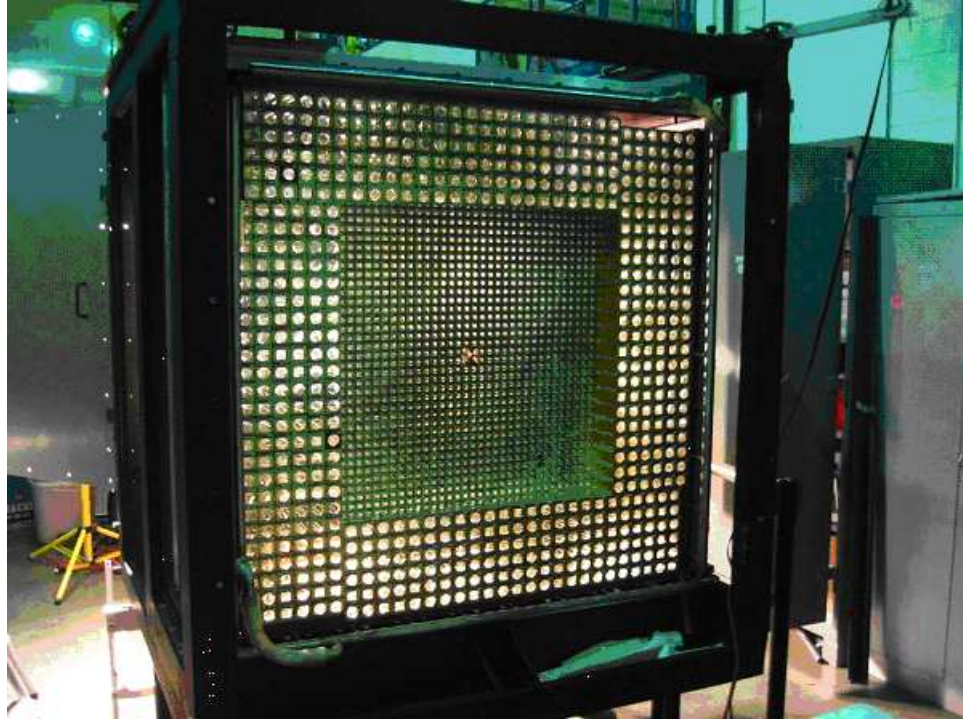


Figure 2.10: The lead tungstate ( $PbWO_4$ ) inset and the lead glass ( $PbO$ ) periphery of HyCal in a frame enclosure.

counters can be used to determine the position of the shower axis. The central region of crystals provides enhanced position and energy resolution for  $\pi^0$  mass and angle measurements. These high resolution detectors cover a region around the beam where at least one photon from the  $\pi^0 \rightarrow \gamma\gamma$  decay will hit the calorimeter. Ideally the entire detector would have been constructed from lead–tungstate modules. For the sake of cost effectiveness, the outer part of the calorimeter, where energy resolution and statistics are the primary concern, is made of lead–glass blocks. The dimensions of the lead glass are optimized to measure photon energies in the region from a few hundred MeV to a few GeV. Such an optimization results in reduced position resolution compared to that of the lead-tungstate crystals. The hybrid design of the

calorimeter offers a good compromise between the requirements for precision of position and energy measurements and the price of the calorimeter.

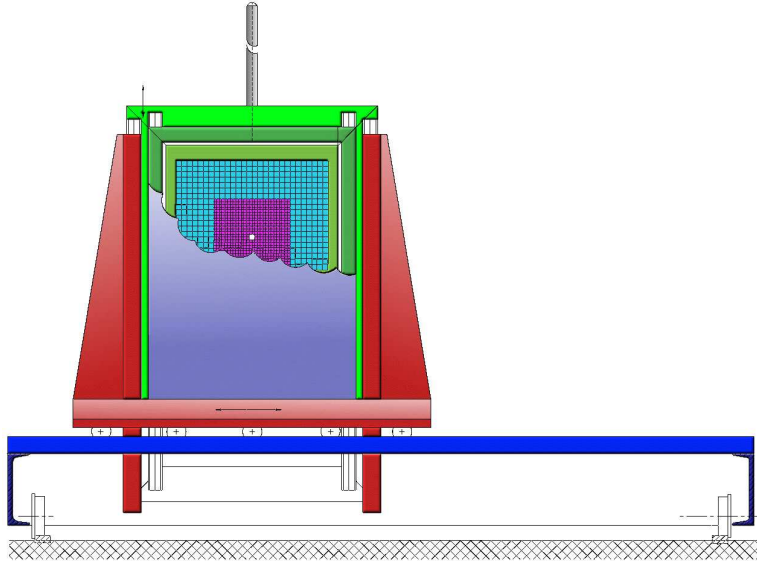


Figure 2.11: Schematic view of HyCal on the transporter. The shaded purple region depicts the lead tungstate modules and the light blue region depicts the lead glass modules.

The gains for individual counters were determined by sending a low intensity tagged photon beam directly into the detector. During the calibration the calorimeter was installed on a transporter in order to expose every module of the detector to the beam (see Figure 2.11). The energy dependent resolution can be described by the following expression [28]:

$$\sigma_E/E = a \oplus b/\sqrt{E} \oplus c/E \quad (2.3)$$

where  $E$  is the energy of incident photon in GeV. The constant  $a$  accounts for calibration errors, shower leakage and non-uniformity in light collection efficiency along the length of

the crystals. The parameter  $b$  arises from statistical fluctuations of electromagnetic shower and photon statistics in the PMT and the term with constant the  $c$  is due to noise in detection electronics. The data from “snake” calibration runs were used to obtain a resolution function for the crystal part of the calorimeter (see Figure 2.12).

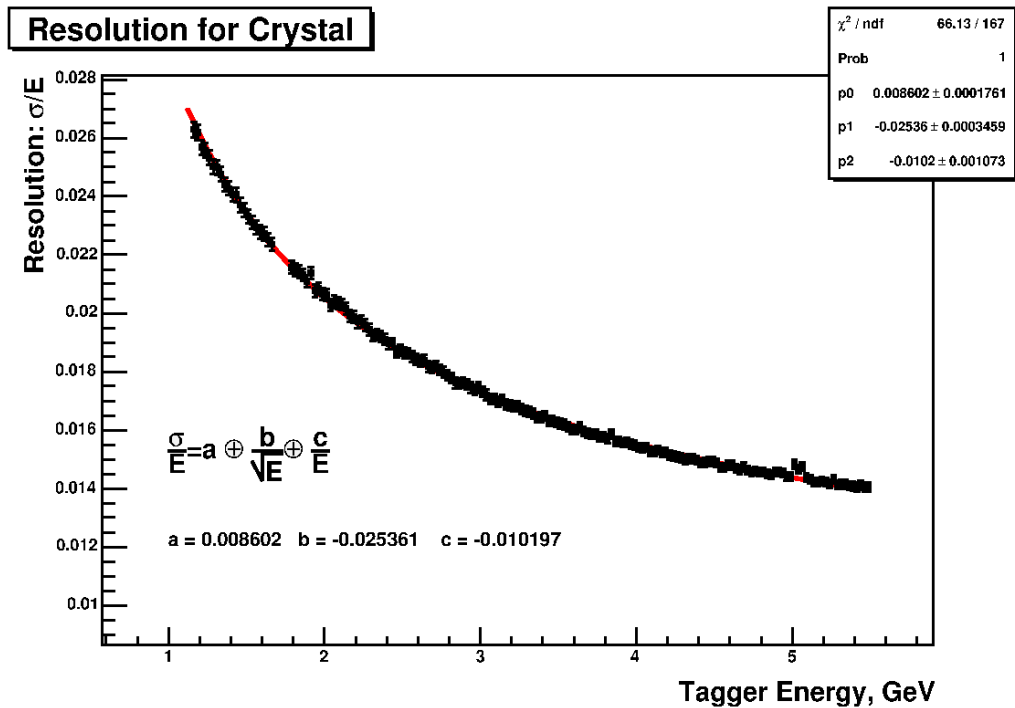


Figure 2.12: HyCal energy resolution function obtained from “snake” calibration data.

The yield of light, produced by scintillation, within the crystal is highly dependent upon temperature ( $\sim 2\%/\text{ }^\circ\text{C}$ ). Therefore, the calorimeter is thermally isolated and surrounded on all four sides by water cooled copper plates in order to stabilize the temperature with a precision of ( $\pm 0.1\text{ }^\circ\text{C}$ ).

## 2.6 Total Absorption Counter

The **Total Absorption Counter (TAC)** consists of a single  $20 \times 20 \times 20 \times 40$  cm<sup>3</sup> lead glass block (SF5,  $L = 17X_o$ ). It has a single 5" Hamamatsu PMT (R1250, rise time  $\sim 2.5$  ns) attached to it and is instrumented with both an ADC and TDC. The TAC was mounted on a support structure with vertical motion behind the HyCal. The vertical motion enabled the placement of the TAC out of the path of the primary beam during high intensity runs.

In the August 2002 test run, with a 100 pA electron beam and a  $2 \times 10^{-5} X_o$  bremsstrahlung radiator, the TAC fired at about 100 kHz with a 35 mV threshold.

The TAC is used to obtain an absolute normalization of the photon flux in the experiment (see 4.1). The normalization procedure is based upon the assumption that the TAC has 100% efficiency for detecting photons in the entire tagging energy range. Figure 2.13 shows the measured TAC-ADC – photon energy correlation.

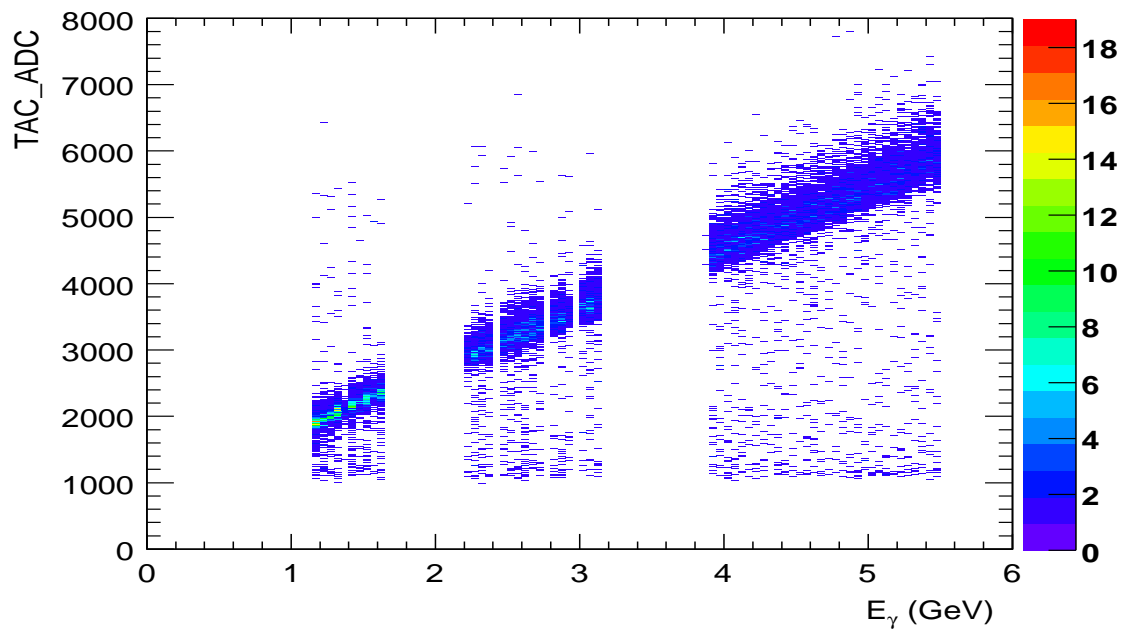


Figure 2.13: Correlation of the photon energy and the TAC ADC counts.

Copyright © Aram Teymurazyan 2008

## CHAPTER : 3 FLUX DETERMINATION IN PRIMEX

### 3.1 Principles of tagged yield normalization

The primary advantages of the PrimEx experiment over the previous Primakoff experiments arise from the use of the Jefferson Lab Hall-B photon tagging facility to carefully control systematic errors and reduce backgrounds. First, the tagging technique allows for a significantly more accurate knowledge of the photon flux. Second, due to the energy dependence of the Primakoff cross section, it is critical to have a good knowledge of the absolute photon beam energy.

In order to determine the energy of the decaying  $\pi^0$ , each event is recorded in coincidence with a signal from the tagger. The experimental cross section for neutral pion photo-production is given by the following expression:

$$\frac{d\sigma}{d\Omega} = \frac{dY_{\pi^0}^{tagged}}{N_{\gamma}^{tagged} \cdot \epsilon \cdot t \cdot d\Omega} \quad (3.1)$$

where  $d\Omega$  is the element of solid angle of the pion detector,  $dY_{\pi^0}^{tagged}$  is the yield of tagged  $\pi^0$ -s within solid angle  $d\Omega$ ,  $t$  is the target thickness,  $\epsilon$  is a factor accounting for geometrical acceptance and energy dependent detection efficiency and  $N_{\gamma}^{tagged}$  is the number of *tagged* photons on the target (the tagged photon flux<sup>1</sup>).

As can be seen from Equation 3.1, the normalization of the cross section directly depends on knowing the photon flux on the target. A naive assumption, that the number of tagged photons on target is equal to the number of hits recorded by the tagging counters, is not true because of a number of effects:

---

<sup>1</sup>Hereafter the tagged photon flux will be referred to simply as the photon flux unless otherwise specified.

- (1) events in which a bremsstrahlung photon is produced and then absorbed before reaching the target.
- (2) Møller scattering events in the bremsstrahlung radiator which produce an electron in the tagging counters without an accompanying photon.
- (3) extra hits registered in the tagging counters due to room background.

To minimize the absorption of photons before they reach the target, the bremsstrahlung beam travels in vacuum. The Møller scattering events are known to affect the tagging rate at the level of a few percent. The impact of the room background on the tagging rates of runs with various electron beam intensities is non-trivial and therefore continuous and attentive monitoring is necessary.

The combination of these effects can be measured in a calibration run by removing the physics target and placing a lead-glass total absorption counter (TAC) directly in the photon beam. Assuming that the total absorption counter is 100% efficient in detecting photons in the energy range relevant for the experiment, the ratio of Tagger-TAC coincidences to the number of tagger hits, the so called absolute tagging ratio, is then recorded:

$$R_{absolute} = \frac{N_{\gamma\cdot e}^{TAC}}{N_e} |_{calibration} \quad (3.2)$$

where  $N_{\gamma\cdot e}^{TAC}$  is the number of photons registered by the TAC in coincidence with a tagging signal and  $N_e$  is the number of electrons registered in tagging counters.

Knowing this ratio, one can determine the tagged photon flux in the data taking run by counting the number of post bremsstrahlung electrons in the tagging counters:

$$N_{\gamma}^{tagged}|_{experiment} = N_e|_{experiment} \times R_{absolute} \quad (3.3)$$

The use of the total absorption counter to calibrate the number of tagged photons per electron in the tagger provides an absolute normalization of the photon flux incident on the  $\pi^0$  production target. However, these measurements can be performed only at intervals between the data taking. Also in the calibration run, the rate of the total absorption counter is limited, and therefore, the tagging ratio<sup>2</sup> can only be measured at a rate which is reduced by a factor of about one thousand as compared to the data taking run. As such, any rate and time dependence in the tagging efficiency must be carefully considered. Consequently, a pair production luminosity monitor was constructed (see Section 2.4) which is able to measure the relative tagged photon flux over a range of all relevant intensities, and operate continuously throughout the data taking runs. The PS uses the physics target as a converter to measure the ratio of the number of  $\gamma + A \rightarrow A + e^+ + e^-$ <sup>3</sup> reactions in coincidence with a tagging signal to the number of hits in the tagging counters (see Equation 3.4),

$$R_{relative} = \frac{N_{e^+e^- \cdot e}^{PS}}{N_e} \quad (3.4)$$

While this is a relative number, its absolute normalization can be fixed with the TAC.

The advantages of the pair spectrometer are that it can operate over the entire range of intensities (of both the flux calibration and data taking runs) and has a smooth, relatively flat acceptance in  $E_{\gamma}$  covering the entire tagging range. The segmentation of the pair spectrometer

---

<sup>2</sup>The term tagging efficiency will be used interchangeably with “absolute tagging ratio” and is not to be confused with the efficiency of the tagging counters.

<sup>3</sup>The reaction  $\gamma + A \rightarrow A + e^+ + e^-$  is the primary source of  $e^+e^-$  pairs, but it is understandable that higher order processes also contribute to the rates registered by the PS.

detectors is driven by the fact that the pair production and Primakoff target are the same, and therefore the pair spectrometer detectors must accommodate the rates from a 5% radiation length target. Under the PrimEx run conditions, we had singles rates on a single telescope of about 140kHz, and a total of 90 kHz of PS-Tagger coincidences over the range of tagging energies. The efficiency of the pair spectrometer for tagging photons was about 0.45%.

The PrimEx experiment is intended to provide a measurement of the  $\pi^0$  lifetime with better than 1.4% precision. As quoted in the error budget of the experiment (see [20]), the main contribution to the error bar in the PrimEx measurement comes from the knowledge of the photon flux. To achieve the desired precision in the measurement of the  $\pi^0$  decay width it is necessary to know the photon flux to 1% or better. To emphasize the importance of the photon flux measurement for the PrimEx experiment it should be noted that such a high precision measurement of the photon flux has not been previously attempted at Jefferson Lab Hall-B. As indicated by Equation 3.3, the problem of cross section normalization is reduced to the determination of the number of electrons in tagging counters and measuring the absolute tagging ratio. The constant online monitoring of the relative photon flux is also very crucial for the precision tagged photon flux measurement.

Note that in Equation 3.1 the  $Y_{\pi^0}^{\text{tagged}}$  and  $N_{\gamma}^{\text{tagged}}$  need to be carefully defined. As it is defined above,  $Y_{\pi^0}^{\text{tagged}}$  is the total number of  $\pi^0$  events induced by **tagged** photons, and **not** the total number of  $\pi^0$  events observed by HyCal. To reduce the data acquisition rates the primary trigger is not induced by the tagged photons, but by the HyCal, which means there are possible  $\pi^0$  events in the data which are induced by untagged photons. These  $\pi^0$  events, which do not have “partner” electrons in the tagger have essentially no capability to pass the energy conservation requirement which is used to reduce the backgrounds. Thus these events

are excluded from consideration. In the yield one counts only  $\pi^0$  events which are tagged as true events. The  $N_\gamma^{tagged}$  in the denominator of Equation 3.1 has to be counted consistently with the way  $Y_{\pi^0}^{tagged}$  is estimated. This means that if for any reason events are discarded from yield calculation, they should not be considered when calculating the photon flux either and vice versa.

The fact that for the cross section measurement one is interested only in the tagged pion yield, *i.e.*, the number coincidences of  $\pi^0$  and tagging electron, and the tagged photon flux, which is proportional to the number of tagging electrons, results in the convenience of not having to worry about the detection efficiency of tagging counters and the deadtime effects of the data acquisition. Due to the tagged nature of both the yield and the photon flux, the efficiency of the tagger and the deadtime, appear in the numerator as well as in the denominator when calculating the cross section such that the effect cancels out. But keep in mind that this does not necessarily include inefficiencies which can be introduced through the reconstruction software. A more detailed discussion will follow in Chapter 6.

Copyright © Aram Teymurazyan 2008

## CHAPTER : 4 ABSOLUTE TAGGING RATIOS

### 4.1 Absolute calibration with total absorption counter

During PrimEx data taking in the Fall of 2004, specialized calibration runs were periodically performed to determine the absolute normalization of the photon flux. For a calibration run, the experimental target is retracted and a Total Absorption Counter (TAC) is placed in the path of the photon beam. To avoid radiation damage to the TAC, the electron beam intensity is lowered to  $\sim 70 - 80$  pA<sup>1</sup>. The low intensity of calibration runs enables the use of the Tagger Master OR (MOR) signal as the data acquisition trigger. The MOR signal is formed by OR-ing the timing information from all or any of the 61 T-counters. Using the MOR trigger enables one to directly count the number of electrons that hit the tagging counters. Due to the reduced intensity of the primary beam, even a slight variation in room background can have a significant negative effect on the tagging ratios. Thus periodic measurements are necessary to ensure a stable, reproducible result. As discussed in Section 2.2 the T-counters have overlapping geometrical acceptances and non-overlapping T-channels are defined via timing coincidences. Due to the small size of the overlaps, the rates in the even channels are low (see Figure 2.5 Parts (a) and (b)), so in order to obtain sub-percent statistical errors within a reasonable amount of time the even channels are grouped together with the previous odd channel to form “combined T-channels”<sup>2</sup> as shown on Figure 4.1.

Absolute tagging ratios are then defined for each of the T-counters as:

---

<sup>1</sup>The maximum beam intensity for the safe operation of the TAC is  $\sim 150 - 200$  pA

<sup>2</sup>In this and subsequent sections the term “T-counter” will refer to the “combined T-channels” and not to the physical T-counters unless otherwise noted.

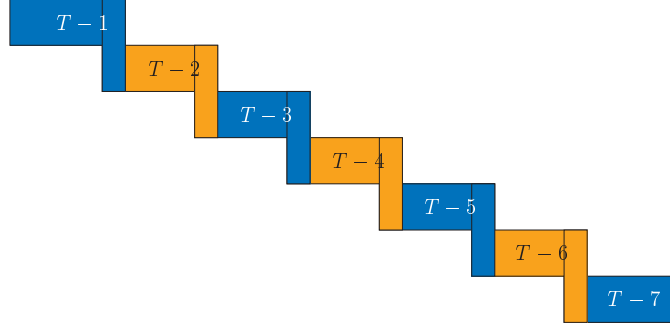


Figure 4.1: The numbering scheme of the combined T-channels, only the first 7 counters are shown.

$$R_{absolute}^i = \frac{N_{\gamma \cdot e^i}^{TAC}}{N_e^i} \quad (4.1)$$

where  $N_e^i$  is the number of electrons registered in the T-counter  $i$  and  $N_{\gamma \cdot e^i}^{TAC}$  is the number of photons registered by the TAC in coincidence with an electron in the T-counter  $i$ .

## 4.2 TAC - Tagger coincidence and background determination

The difference in times of hits, recorded for the tagger and for the TAC, forms a coincidence peak with a flat background. Parts (a) and (b), Figure 4.2, show typical coincidence spectra for TAC-Tagger. Note that the signal to background ratio is better than 10000 : 1, thus the determination of the number of coincidences is quite insensitive to the accuracy of the background estimation procedure.

From Figure 4.2 (b) we can see that the background is not uniform on the left and right sides of the coincidence peak. The dip, around  $\sim 5$  to 40 ns, to the right of the coincidence

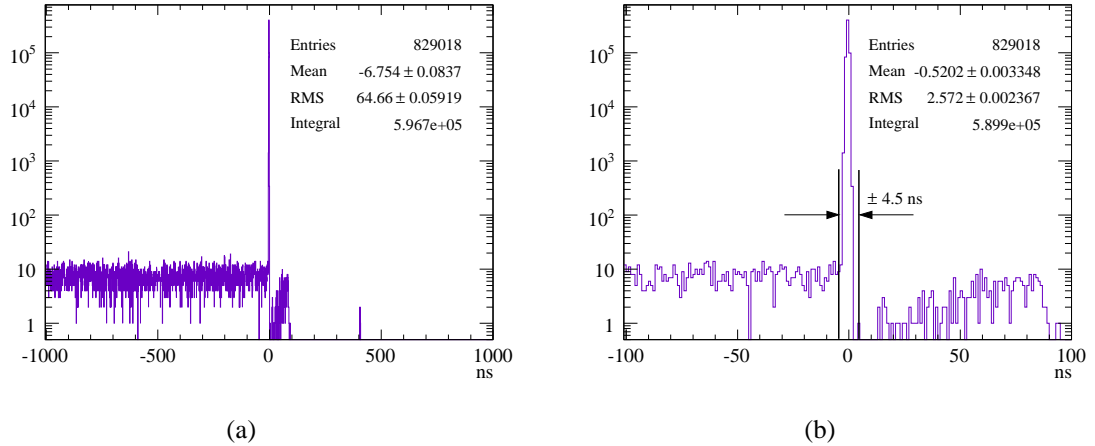


Figure 4.2: (a) Distribution of time differences for events reconstructed for Tagger and TAC. (b) a close up version of the first plot showing the  $\pm 4.5$  ns timing window for coincidence events.

peak is due to the TDC dead time. A  $\pm 4.5$  ns window was set up around 0 to determine the number of TAC-Tagger coincidences. Due to the nonuniformity of the background, a  $w \approx 4.5 \mu\text{s}$  window, from 7 to 4500 ns, was taken only on the left side of the coincidence peak to calculate the background level. Assuming a flat uniform background the number of background events per bin was calculated using the formula:

$$\text{Background events per bin} = \frac{\text{Integral of events}}{w} \quad (4.2)$$

Using the above described procedure, the background was evaluated for each T-counter, rescaled according to the size of the coincidence window and subtracted from the integral

number of events in the peak around zero to obtain the number of true TAC-Tagger coincidences.

### 4.3 Effects of incident electron beam intensity on absolute tagging ratios

As it was previously discussed, due to the technical limitations of the TAC the absolute tagging ratios can be measured only at beam intensities which are  $\sim 10^3$  times lower than the intensity of a regular production run. The goal of PrimEx is to be able to measure the photon flux for the production data with a precision of 1% or better. It is important to demonstrate that the tagging efficiencies obtained at beam intensities of  $\sim 80$  pA are valid when applied to the data collected at the high beam intensities of about 80 to 130 nA. To investigate this, during our running period in Fall of 2004 we had normalization runs with various beam intensities (40 – 120 pA).

Figure 4.3 (top) shows the absolute tagging ratios as a function of T-counter number measured at different beam intensities. An artificial shift was introduced on the horizontal axis in order to be able to distinguish the different measurements. As a result, one has 11 groups of 4 points (one group per T-counter). The weighted average was calculated for each of the 11 groups. Figure 4.3 (bottom) shows the percent deviation of each measurement from the mean value for the relevant group. No noticeable systematic dependence of tagging ratios on the incident beam intensity was detected when varying the beam intensity from 40 to 120 pA. The run summary of the data used for this study is presented in Table 4.1. Note that the Pair Spectrometer (PS) dipole was running at  $\sim -3000$  A and a 12.7 mm collimator was used during this measurements. A more complete answer to the question of intensity dependence of tagging efficiencies can be found by looking at relative tagging ratios where the beam intensity

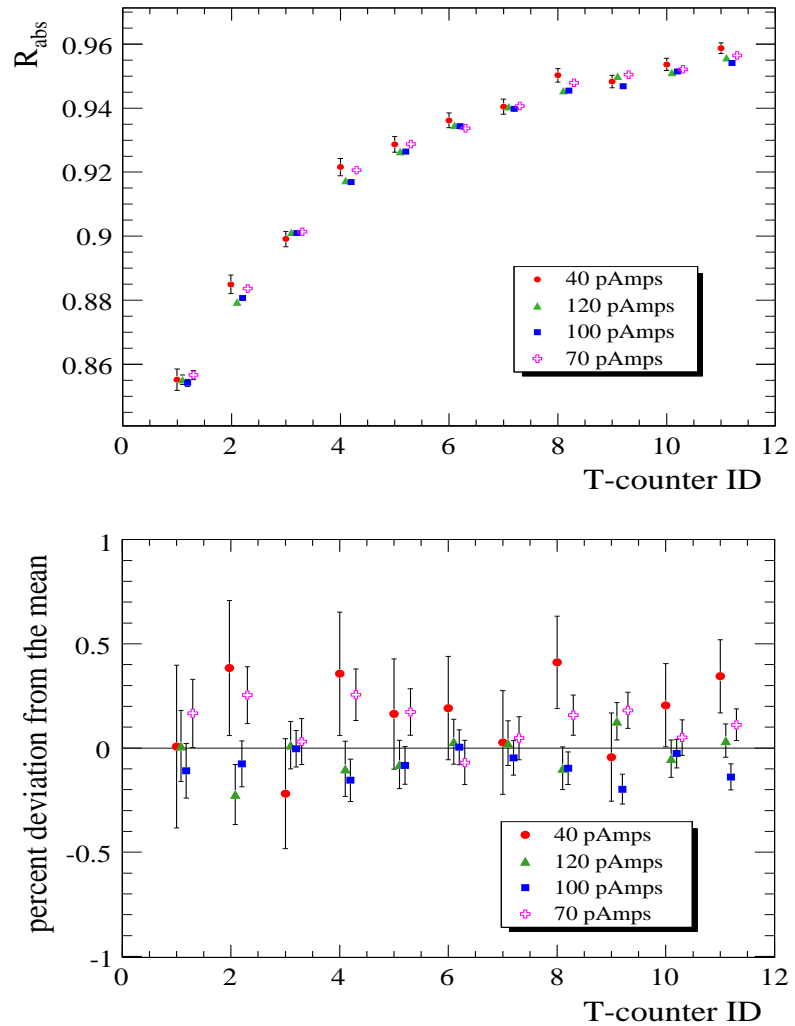


Figure 4.3: (top) Absolute tagging ratios plotted as a function of T-counter number for runs with different beam intensities, (bottom) The percent deviations from the mean for tagging ratio measurements made at different beam intensities for the first 11 T-counters.

can be changed anywhere from 0 to 100 – 150 nA (see Chapter 5).

Table 4.1: Run summary of data used for tagging efficiency beam intensity (*in*)dependence test.

Run#	PS dipole current	Radiator	Collim. type	Collim. pos.	Beam Current
4552	-3005.14 A	C	12.7 mm	7.02 in	40 pA
4553	-3005.14 A	C	12.7 mm	7.02 in	120 pA
4554	-3005.14 A	C	12.7 mm	7.02 in	100 pA
4774	-3105.43 A	C	12.7 mm	7.02 in	70 pA

#### 4.4 Effects of collimator size

A decision was made for PrimEx to run with very loose collimation of the bremsstrahlung photon beam to cut out the beam halo. Together with careful monitoring of the beam position, collimation should increase the stability of the luminosity by keeping the photon beam focused at one spot on the target and thus reducing the effects of possible nonuniformity of the target thickness.

Two different sizes of copper collimators were available for this purpose (see Section 2.1). In Figure 4.4 (top) the relative tagging ratios are plotted versus T-counter ID for data taken with two different collimators. For reference purposes a result with no collimation is also plotted. The running conditions requested for this data taking period are summarized in Table 4.2. Note that for these measurements the statistical error on each point is on the order of 0.15%. It is easy to see from Figure 4.4 (bottom) that the 12.7 mm collimator cuts out  $\sim 1\%$  of the photon beam and 8.6 mm collimator cuts out  $\sim 4\%$  of the photon beam.

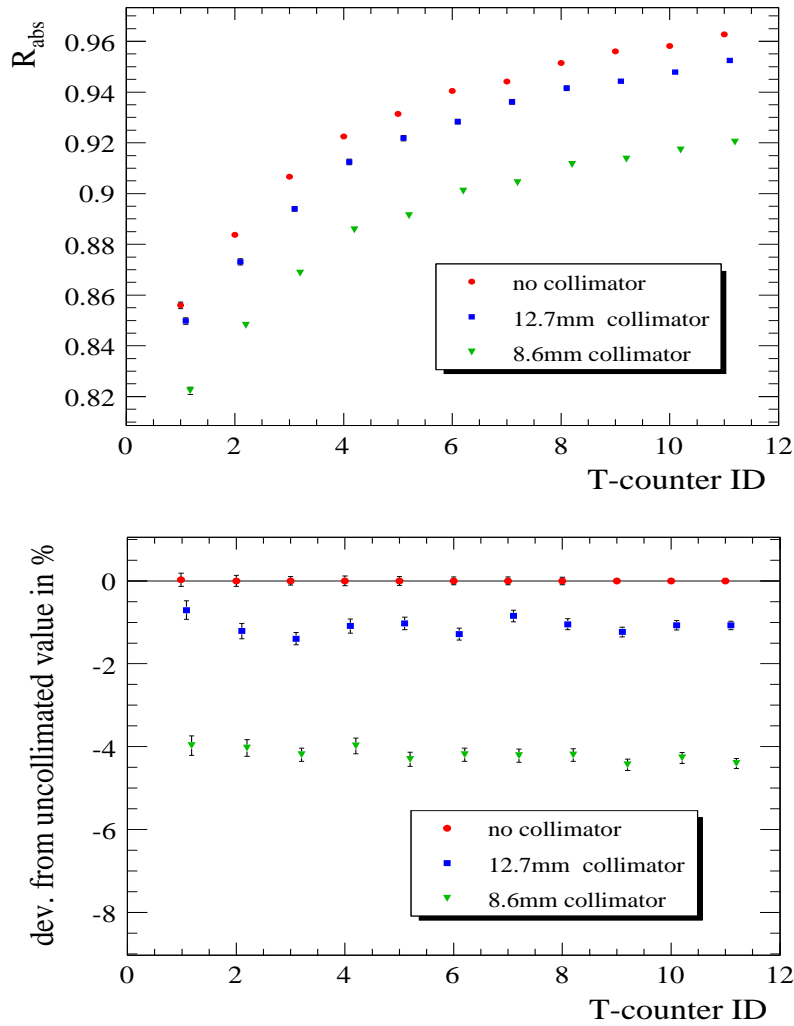


Figure 4.4: (top)  $R_{abs}$  measured for 3 different collimator sizes, (bottom) Percent deviation from the uncollimated value.

#### 4.5 Effects of collimator position misalignment

Figure 4.5 shows the position of the collimator on its ladder versus run number. One can easily see that the entire running period can be divided into two groups of runs. Group 1) with run numbers from 4100 to 4295 with collimator at 7.075" and group 2) with run numbers from 4502 to 5447 with collimator at 7.02". Keeping in mind the required precision of 1% on the

Table 4.2: Run summary of data used for tagging efficiency collimator size dependence test.

Run#	PS dipole current	Radiator	Collim. type	Collim. pos.	Beam Current
4549	-3005.14 A	C	12.7 mm	7.02 in	70 pA
4550	-3005.14 A	C	8.6 mm	2.98 in	70 pA
4551	-3005.14 A	C	NONE	0.0 in	70 pA

photon flux, it is important to investigate the extent to which the tagging ratios are affected by this shift.

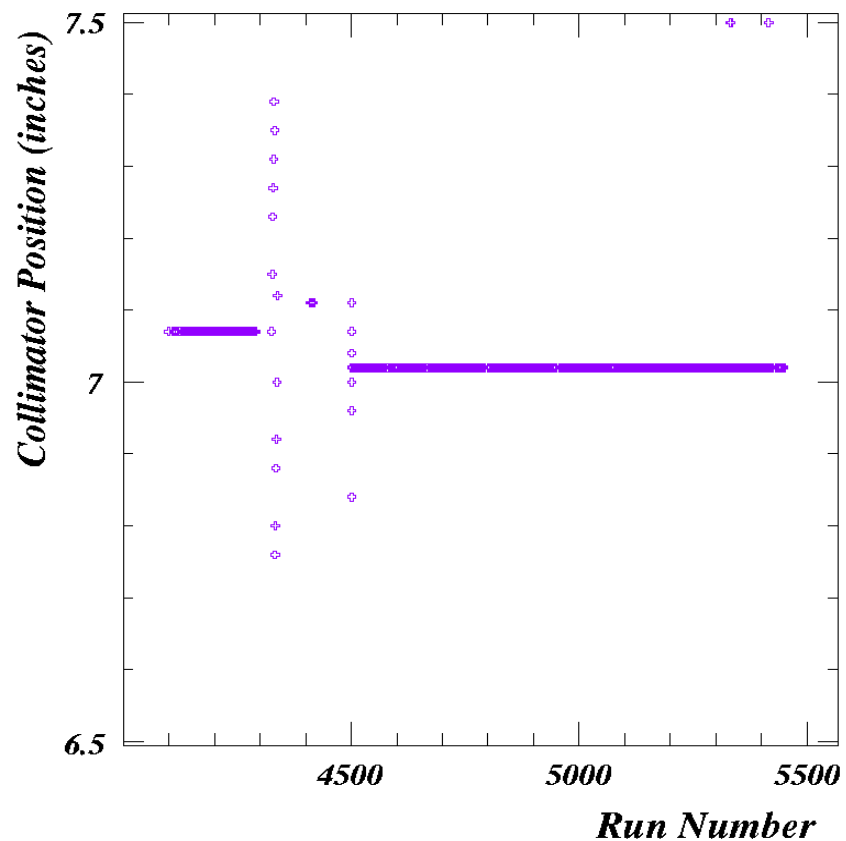


Figure 4.5: Collimator position vs. run number.

The tagging ratios measured for five different positions are shown in Figure 4.6 (top). Figure 4.6 (bottom) shows the percent deviation of tagging ratios, measured at different positions of the collimator, from the value which was measured with the collimator in its nominal position (*i.e.*, at 7.02"). From Figure 4.6 (bottom) one can easily see that the shift in collimator position from 7.02" to 7.15" ( $\sim 3.3$  mm) lowers absolute tagging ratios by about 0.34%, hence if needed runs 4549, 4326, 4327 can all be used when calculating the final tagging ratios to reduce the the statistical error. One can also notice that larger shifts in collimator position result in  $\sim 1.2\%$  and more reduction of  $R_{abs}$ .

The running conditions for the test of the (*in*)dependence of the tagging ratios on the collimator position are presented in Table 4.3.

Table 4.3: Run summary of data used for tagging efficiency collimator position dependence test.

Run#	PS dipole current	Radiator	Collim. type	Collim. pos.	Beam Current
4549	-3005.14 A	C	12.7 mm	7.02 in	70 pA
4326	900.7 A	C	12.7 mm	7.07 in	70 pA
4327	900.7 A	C	12.7 mm	7.15 in	70 pA
4328	900.7 A	C	12.7 mm	7.23 in	70 pA
4329	900.7 A	C	12.7 mm	7.27 in	70 pA

#### 4.6 Effects of HyCal scraping due to beam mis-steering (uncollimated beam)

As described in Section 2.1, the space between the Pair Spectrometer dipole vacuum window and the face of HyCal is taken up by a helium bag. The HyCal has a central opening to allow the uninteracted beam particles to pass through. A **Gamma Profiler** (GP) was installed directly

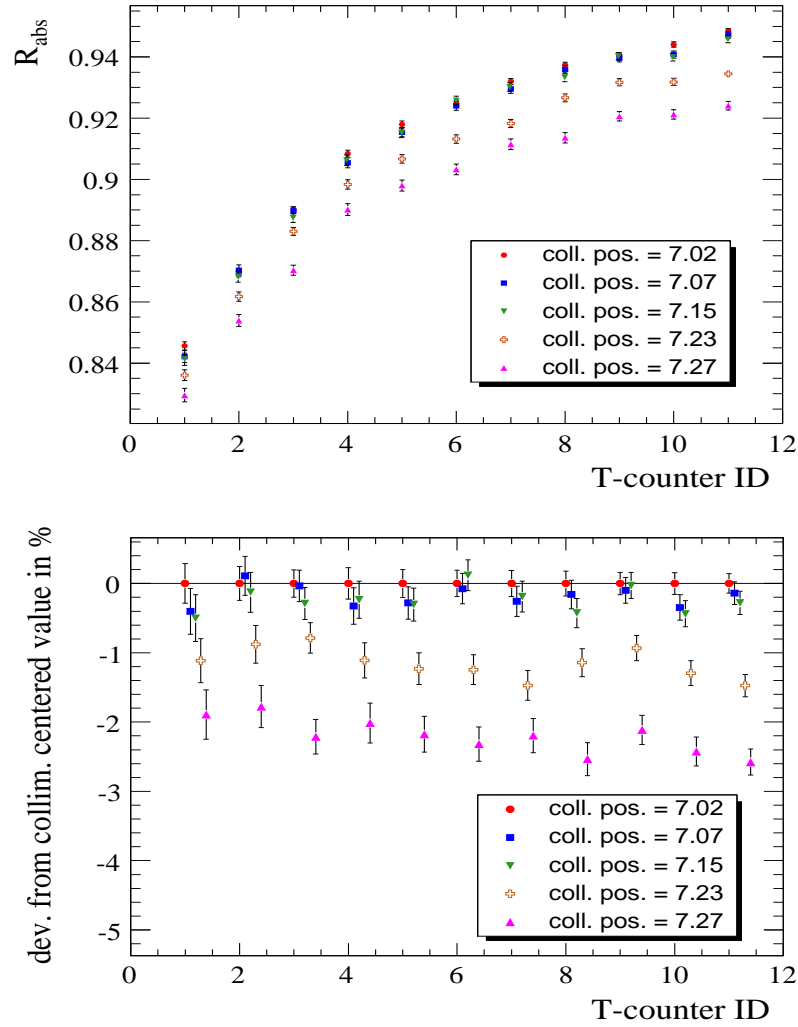


Figure 4.6: (top)  $R_{abs}$  measured for five different collimator positions measured in inches. (bottom) Percent deviation from the measurement taken with collimator in its nominal position (7.02'').

behind the calorimeter to monitor the shape and the position of the photon beam during the experiment. Ideally one would place the TAC right at the position of the target but given the technical constraints in case of PrimEx, the TAC was mounted on the same moving platform as the GP behind HyCal and was placed in the path of the photon beam interchangibly with

GP to perform a normalization run. In this configuration the photons must travel through a  $4.15 \times 4.15 \text{ cm}^2$  central opening in HyCal (see Section 2.5) before they can be registered in the TAC. Consequently it is necessary to evaluate to what extent the size of the HyCal central opening and the alignment of the photon beam with respect to the HyCal axis affect the results of normalization runs. For this purpose the direction of the photon beam was purposefully altered and the tagging ratios were measured. To allow for larger artificial shifts in beam position the collimator was retracted during this study. Due to the fact that this investigation was done with uncollimated beam, it places an upper limit on the amount of the photon beam that can be cut by HyCal due to scraping. Because the GP was mounted on the same moving platform as the TAC, photon beam position measurements were possible only before and after a normalization run. In light of this, the study described in this section should be considered only as a qualitative exercise.

It was determined that in the absolute coordinate system of the GP, the nominal photon beam position is  $X_{av} = -0.83 \text{ mm}$  and  $Y_{av} = -1.45 \text{ mm}$ . Figure 4.7 (top) shows several measurements of tagging ratios with different beam positions. Run # 4338 was taken with the beam at its nominal position. For run # 4340 the beam was steered a little over 5 mm in the positive  $Y$  direction to  $(-0.93, 4.09) \text{ mm}$ . For run # 4341 the beam was at  $(-6.54, -1.23) \text{ mm}$ . During run # 4342 beam was at  $(-9.45, -1.52) \text{ mm}$  – *i.e.*, about 8.5 mm off of its nominal position. For run # 4343 beam was at  $(5.12, -1.44) \text{ mm}$  – *i.e.*, about 6 mm off of its nominal position.

This qualitative study indicates that the HyCal and the beam were not positioned ideally with respect to each other. Runs # 4342 and 4343 indicate that a  $\sim 8.5 \text{ mm}$  shift in the beam position in the negative direction has the same effect on the tagging ratios as a  $\sim 6 \text{ mm}$  shift in

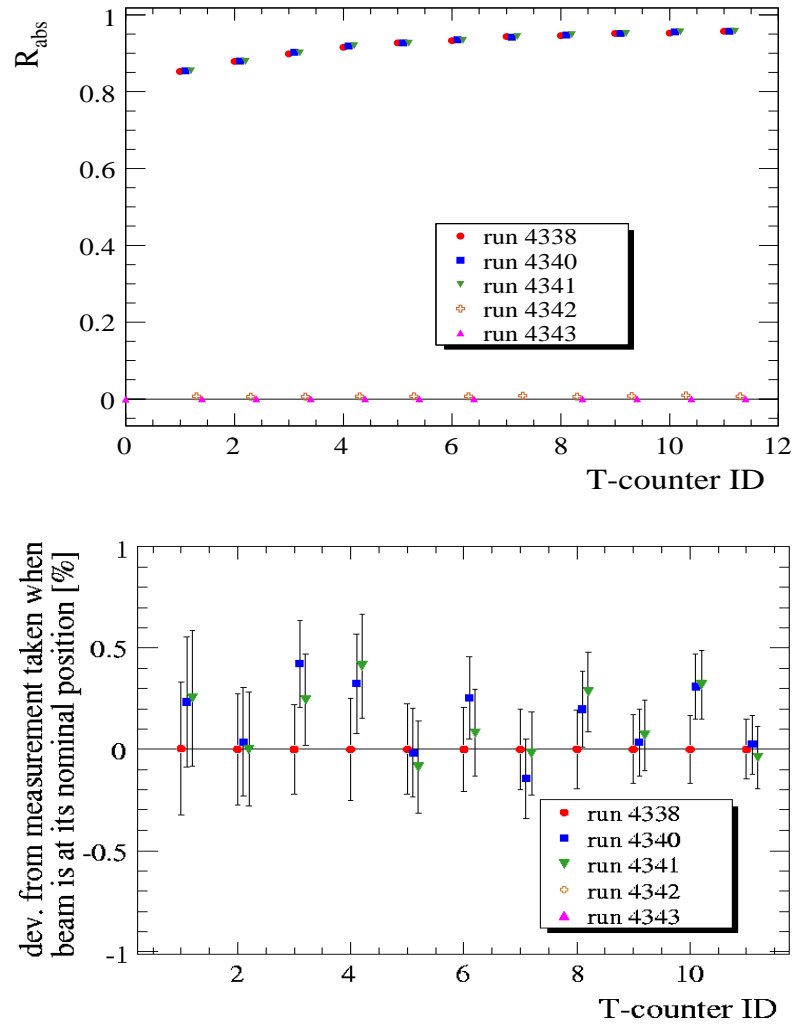


Figure 4.7: (top)  $R_{abs}$  measured for five different beam angles. (bottom) Percent deviation from the uncollimated value.

the positive direction along the  $X$  axis. Also runs # 4340 and 4341 indicate a slight increase ( $\sim 0.23\%$ ) in tagging ratios when the beam is steered 5 mm in the positive  $Y$  direction or 5 mm in the negative  $X$  direction.

The table below lists all other parameters of interest for the runs included in this study.

Table 4.4: Run summary of data used for the study of tagging efficiency dependence on the beam position.

Run#	PS dipole current	Radiator	Collim. type	Collim. pos.	Beam Current
4338	900.7 A	C	NONE	0 in	70 pA
4340	900.7 A	C	NONE	0 in	70 pA
4341	900.7 A	C	NONE	0 in	70 pA
4342	900.7 A	C	NONE	0 in	70 pA
4343	900.7 A	C	NONE	0 in	70 pA

#### 4.7 Long and short term reproducibility with uncollimated beam

To test our ability to perform a consistent measurement of the absolute tagging ratios,  $R_{absolute}$ , we had back-to-back normalization runs which were taken only 20 – 25 minutes apart. This study includes runs number 4322, 4323, 4324, 4325. The Pair Spectrometer magnet was operating at  $\sim 900$  A.

Table 4.5: Run summary of data used for tagging efficiency short term reproducibility test.

Run#	PS dipole current	Radiator	Collim. type	Collim. pos.	Beam Current
4322	900.7 A	C	NONE	0 in	70 pA
4323	900.7 A	C	NONE	0 in	70 pA
4324	900.7 A	C	NONE	0 in	70 pA
4325	900.7 A	C	NONE	0 in	70 pA

As can be seen from Figure 4.8, the study shows that all four runs agree within the limits of required precision and statistical errors.

The set of runs testing the reproducibility of absolute tagging ratios after long periods of

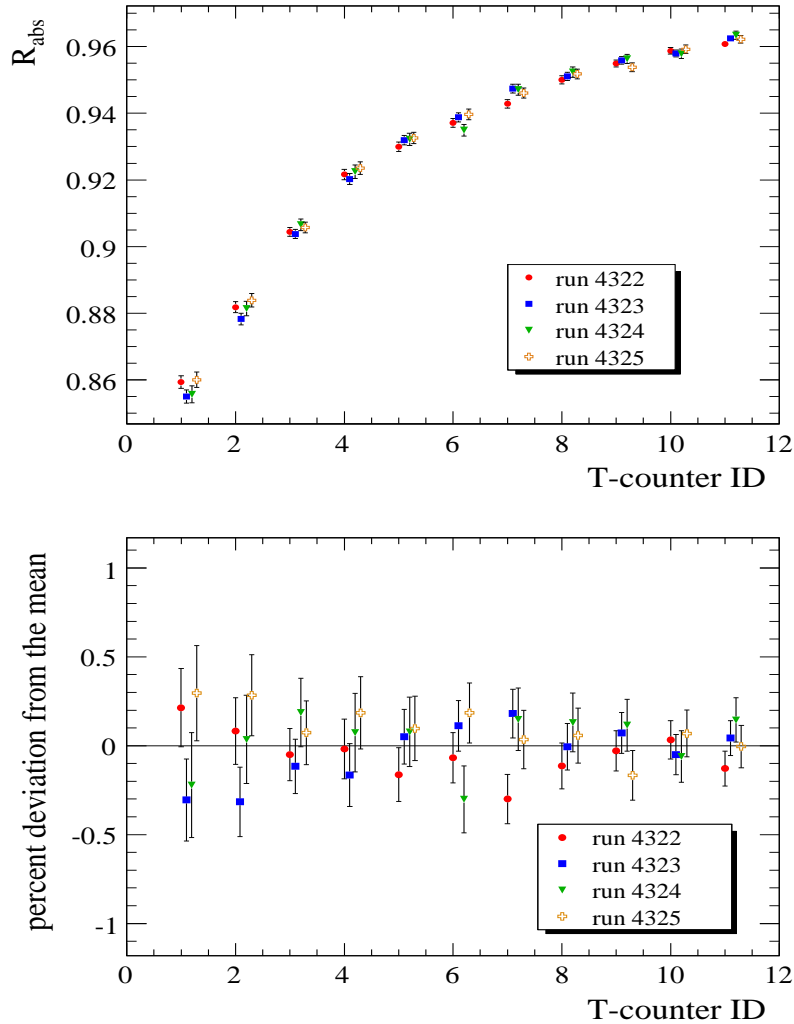


Figure 4.8: (top)  $R_{abs}$  measured for four consecutive runs. (bottom) Percent deviation from the mean.

time is 4551, 4324 and 4338. All of these runs were performed at different values of the field of Pair Spectrometer dipole ( $\sim 3000, 900$  and  $0A$ ).

Figure 4.9 (top) shows the absolute tagging ratios measured for the first 11 T-counters. These runs were taken  $\sim 4$  and half hours and 5 days apart from each other (counting from

run 4324). Figure 4.9 (bottom) shows the percent deviation of the tagging ratio for each T-counter from the relevant average value. The statistical error for each point is on the order of 0.2%. As seen from the plots, all three measurements are in very good agreement with each other (better than 0.3%). Note that since all three measurements were taken with different settings of Pair Spectrometer dipole, this study also shows that there is no detectable dependence of absolute tagging ratios on the magnetic field of the PS dipole when using an uncollimated photon beam.

Table 4.6: Run summary of data used for tagging efficiency long term reproducibility test.

<i>Run#</i>	<i>PS dipole current</i>	<i>Radiator</i>	<i>Collim. type</i>	<i>Collim. pos.</i>	<i>Beam Current</i>
4324	900.7 A	C	NONE	0 in	70 pA
4338	~0 A	C	NONE	0 in	70 pA
4551	-3005.19 A	C	NONE	0 in	70 pA

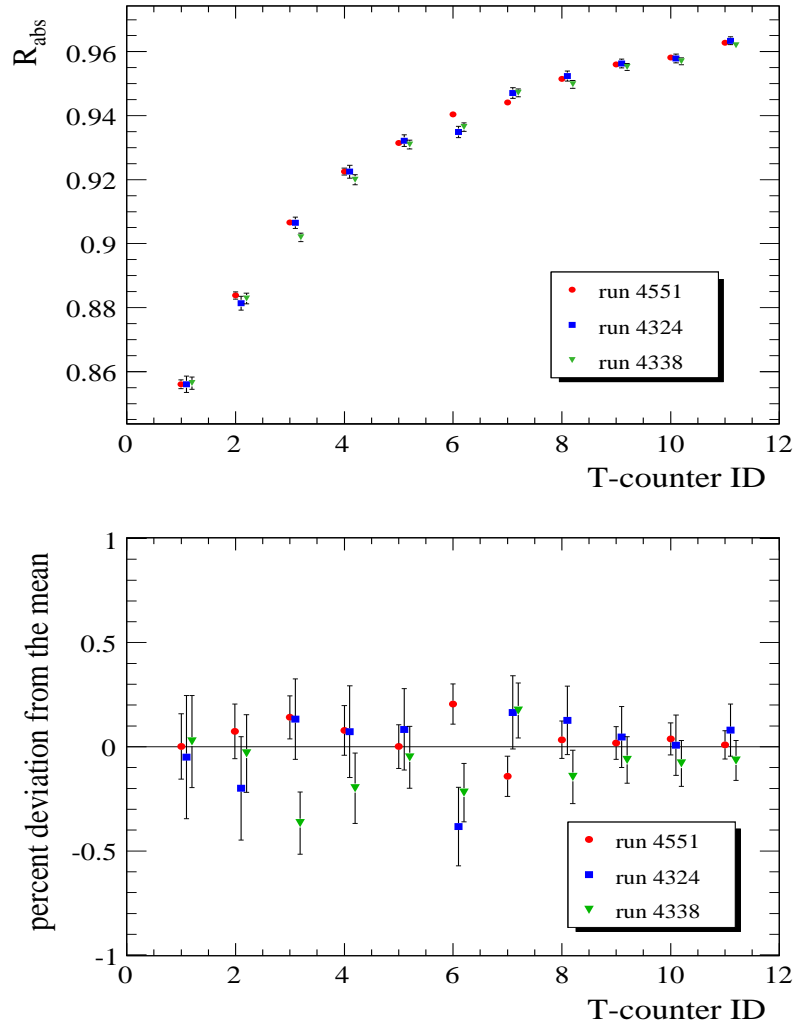


Figure 4.9: (top)  $R_{abs}$  measured for three runs which were spread in time during our data taking. (bottom) Percent deviation from the mean.

#### 4.8 Effects of the PS dipole field with collimated beam

As was already demonstrated in Section 4.7, the PS dipole field has no measurable effect on the tagging efficiencies in the case of an uncollimated photon beam. Since, due to technical

difficulties with the PS power supply, the normalization runs were performed at different values of the magnetic field of the PS dipole, and the production data for PrimEx were taken with a 12.7 mm collimator, it is important to investigate the effect of the magnetic field on the tagging ratios measured for a collimated beam. For this purpose I have selected runs # 4339 and 4326. The running conditions for these two data-sets are summarized in Table 4.7:

Table 4.7: Run summary of data used for tagging efficiency PS dipole field dependence test.

<i>Run#</i>	<i>PS dipole current</i>	<i>Radiator</i>	<i>Collim. type</i>	<i>Collim. pos.</i>	<i>Beam Current</i>
4339	0 A	C	12.7 mm	7.12 in	70 pA
4326	900.7 A	C	12.7 mm	7.07 in	70 pA

Note that the collimator position for these runs is different from the nominal 7.02" value. There is about 1.3 mm difference in collimator position for runs # 4326 and 4339, but as demonstrated in Section 4.5 the effect of this shift is not larger than  $\sim 0.2\%$ ; hence it can be safely concluded that the strength of the PS dipole field has no measurable effect on the tagging ratios.

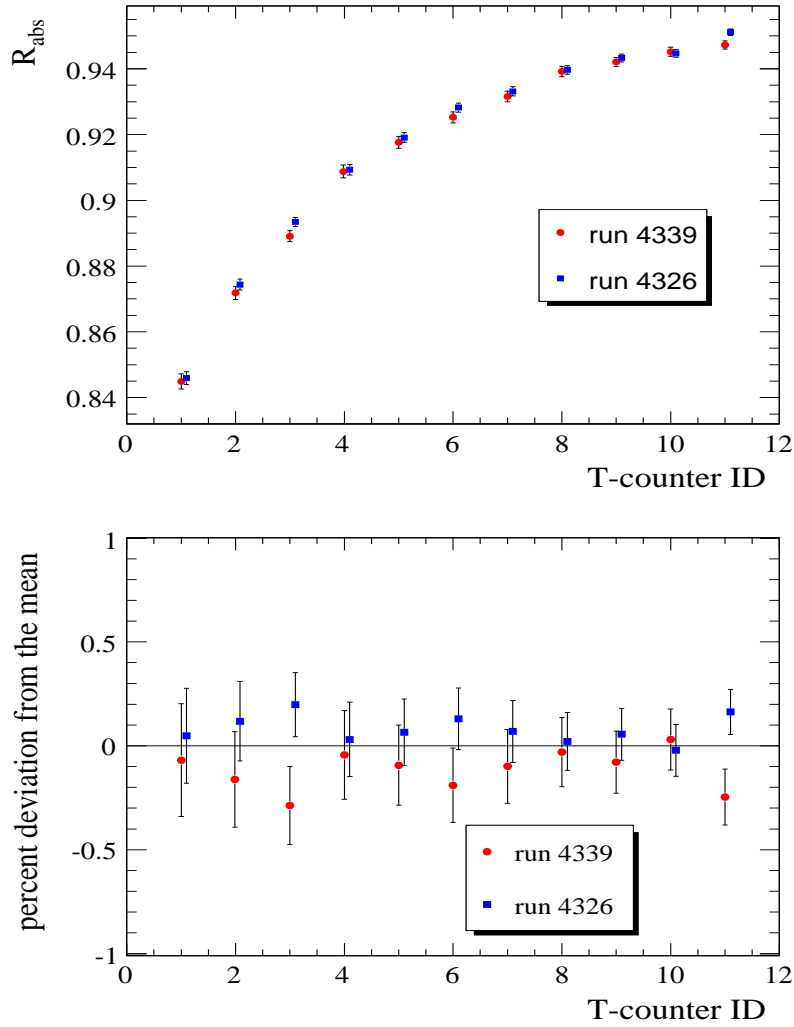


Figure 4.10: (top)  $R_{abs}$  measured for two runs which were taken with different settings of PS dipole magnet. (bottom) Percent deviation from the mean value.

#### 4.9 Absorption in the target

Some of the photons are absorbed in the target without producing a  $\pi^0$ . Special TAC runs with a carbon target placed in the beam were performed to study this effect. Figures 4.11 and 4.12 show a comparison of tagging efficiencies measured for target in runs to those measured for

target out runs for measurements performed without and with photon beam collimation. Both studies yield consistent results indicating that  $\sim 3\%$  of the photons are lost in the target.

Since PrimEx is aiming for a  $\sim 1.5\%$  level absolute cross-section measurement, one has to correct the yields for absorption of photons in the target. The main reaction of interest for PrimEx, ( $\pi^0 \rightarrow \gamma\gamma$ ) and the consistency check reactions (Compton effect and  $e^+e^-$  production) are affected by the photon absorption in the target on different levels. The pair production yields do not need to be adjusted for the 3% of the lost photon flux, since the attenuation of the photon beam in the target is included in the simulation (see Chapter 7). In the case of the Compton and Primakoff effects not only the primary photon but also the secondary photons can be absorbed in the target. Since the Compton scattering or the  $\pi^0$ -production can happen anywhere along the longitudinal direction of the target, the result of this study can be used to set an upper limit on the effect of photon absorption.

Table 4.8: Run summary of data used for the study of photon absorption in the target with no collimator.

Run#	PS dipole current	Radiator	Collim. type	Collim. pos.	Beam Current
4551	-3005.24 A	C	NONE	0.0 in	70 pA
4736	-3105.43 A	C	NONE	0.0 in	70 pA

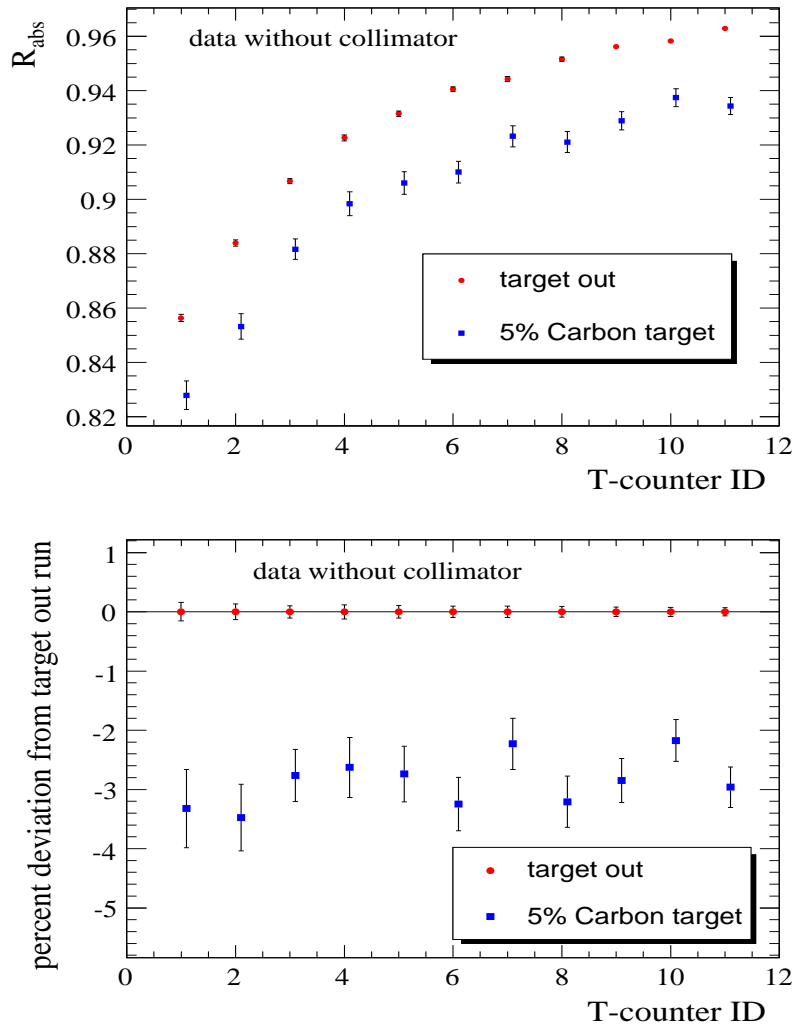


Figure 4.11: (top)  $R_{abs}$  measured for runs which were taken with target in and target out. (bottom) Percent deviation from the measurement obtained with physics target out; no photon collimation.

#### 4.10 Set of runs used to obtain the tagging ratios

I have selected runs # 4549, 4552, 4553, 4554, 4555, 4652, 4737, 4774, 4964, 5071 and 5277 as a set suitable for calculating the tagging efficiencies which have been used in the final

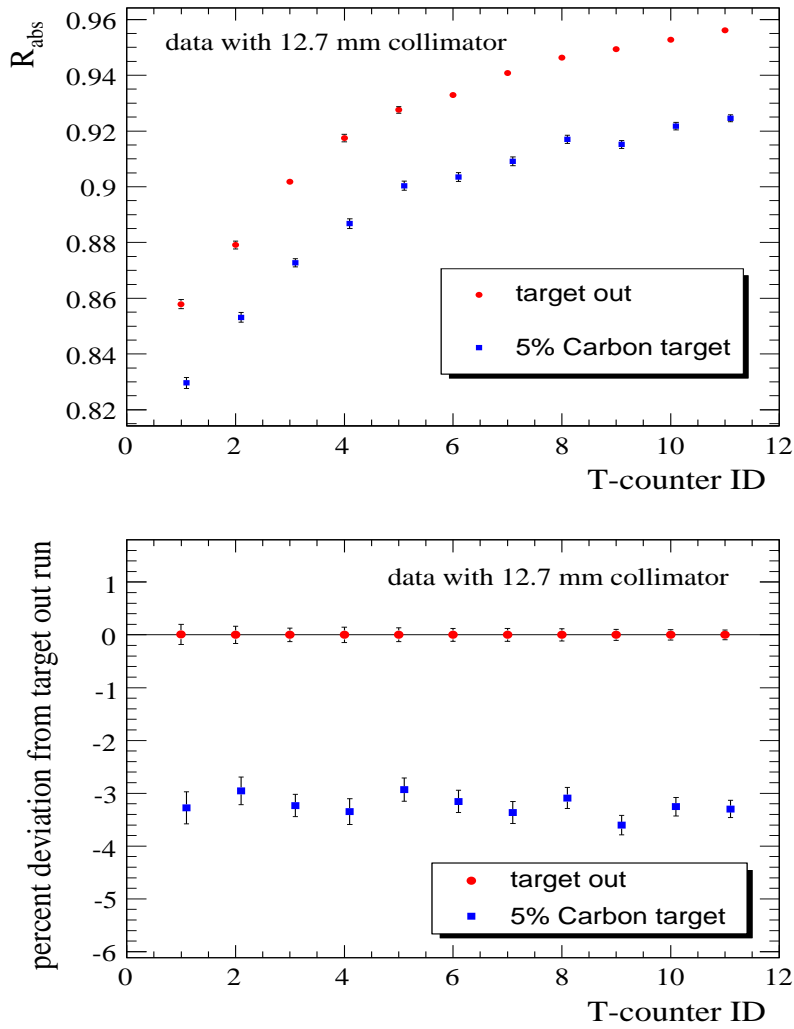


Figure 4.12: (top)  $R_{abs}$  measured for runs which were taken with taget in and target out. (bottom) Percent deviation from the measurement obtained with physics target out; with photon collimation.

photon flux calculation. All of these runs had the collimator in the same position of  $7.02''$  and about the same PS dipole current  $\sim 3000$  A. The only major difference in run conditions was the beam intensity which was varied from 40 to 120 pA. With the exception of the beam intensity, these are the same running conditions as those of the  $\pi^0$ -production data taking.

Table 4.9: Run summary of data used for study of photon absorption in the target with 12.7 mm collimator.

<i>Run#</i>	<i>PS dipole current</i>	<i>Radiator</i>	<i>Collim. type</i>	<i>Collim. pos.</i>	<i>Beam Current</i>
4737	-3105.43 A	C	12.7 mm	7.02 in	70 pA
4735	-3105.43 A	C	12.7 mm	7.02 in	70 pA

The tagging efficiencies for these runs have been calculated using the procedure described in Sections 4.1 and 4.2. The weighted means and the errors on the weighted mean, which was determined based on the results of these measurements are shown in Table 4.10.

Table 4.10: The tagging ratios used in the photon flux determination.

T-counter ID	$R_{absolute}$	Relative Stat. Error (%)
1	0.8544	0.06
2	0.8795	0.05
3	0.8999	0.04
4	0.9175	0.04
5	0.9262	0.04
6	0.9326	0.04
7	0.9394	0.04
8	0.9452	0.03
9	0.9482	0.03
10	0.9510	0.03
11	0.9551	0.03

## CHAPTER : 5 RELATIVE TAGGING RATIOS

### 5.1 Relative calibration with pair spectrometer

As described in Sections 2.4 and 3.1, the Pair Spectrometer is an essential part of PrimEx experimental apparatus designed for relative in-situ monitoring of the photon flux. The Pair Spectrometer uses the experimental target to convert a fraction of photons into  $e^+e^-$  pairs which are deflected in the field of a dipole magnet downstream of the target and are registered in plastic scintillator detectors on both sides of the beam-line. The relative tagging ratios per T-counter<sup>1</sup> are defined as:

$$R_{relative}^i = \frac{N_{e^+e^-.e^i}^{PS}}{N_e^i} \quad (5.1)$$

where  $N_{e_i}$  is the number of electrons registered in T-counter  $i$  and  $N_{e^+e^-.e^i}^{PS}$  is the number of  $e^+e^-$  pairs registered by the PS in coincidence with an electron in T-counter  $i$ .

During our production data taking in Fall of 2004, we had a random, *i.e.* not related to the particles in the beam, clock trigger set up to measure  $R_{relative}^i$ . The use of the random trigger enables one to directly count the number of electrons in the tagging counters and it gives the advantage of being insensitive to beam intensity variations.

### 5.2 PS-Tagger coincidence window and background determination

The event times reconstructed in both Tagger and Pair Spectrometer are randomly distributed in time due to the clock trigger. The difference of times of hits reconstructed for the Tagger

---

<sup>1</sup>The T-counter as defined in Section 4.1, Figure 4.1.

and the PS gives rise to a coincidence peak (correlation of events in Tagger and PS) and a non-flat, triangularly shaped background. A sample timing spectrum is shown on Figure 5.1.

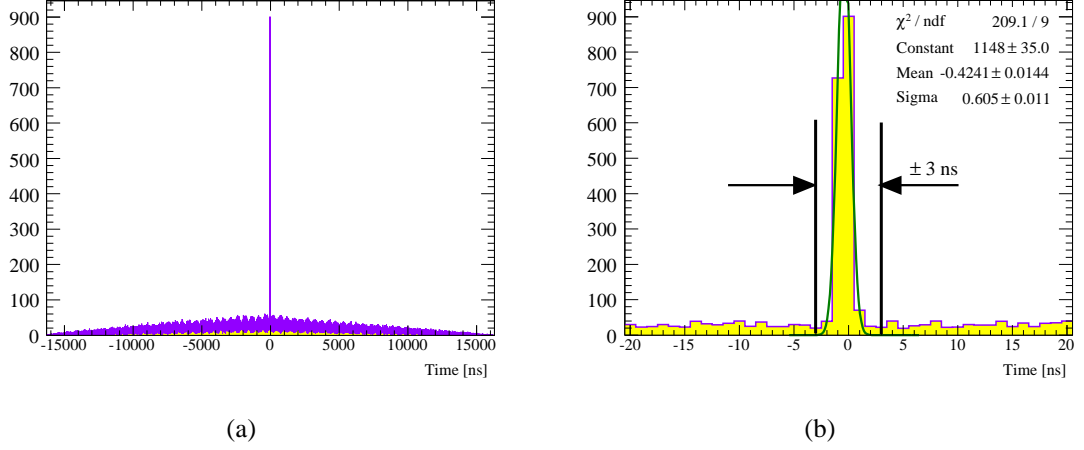


Figure 5.1: (a) Distribution of time differences for events reconstructed in Tagger and PS. (b) A close up of part (a) showing the  $\pm 3.0$  ns timing coincidence window.

By fitting a first order polynomial to the background on each side of the peak one can easily see that the background can be treated as flat if we limit ourselves to a relatively narrow region close to the peak (Figure 5.2).

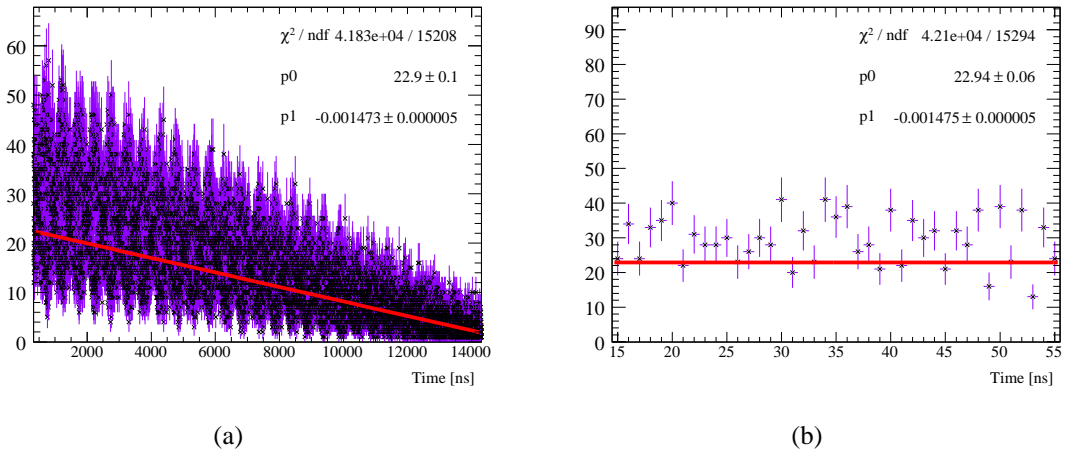


Figure 5.2: (a) Distribution of background events  $\text{Tagger} \cdot \text{PS}$  timing spectra. (b) A close up of part (a) showing the 40ns timing window taken for measuring the background.

A 6 ns window ( $w_{peak}$ ),  $\pm 3$  ns around 0, is set up within which the number of entries is counted ( $N_{peak}^i$ ). To calculate the contribution of the background to the events in the coincidence region two ( $w_B = 40$  ns) windows are taken, 15 ns to 55 ns to the right of the peak and  $-55$  ns to  $-15$  ns to the left of the peak. The distribution of events in those windows is assumed to be flat, and number of background events per bin ( $n_B^i$ ) is calculated using the formula:

$$n_B^i = \frac{\text{Integral}_{left} + \text{Integral}_{right}}{2w_B} \quad (5.2)$$

Finally the number of coincidence events ( $N_{e^+e^- \cdot e^i}^{PS}$ ) is determined by:

$$N_{e^+e^- \cdot e^i}^{PS} = N_{peak}^i - n_B^i w_{peak} = N_{peak}^i - N_B^i \quad (5.3)$$

where  $N_B^i = n_B^i w_{peak}$  – is the number of background events in the coincidence region.

In general, taking the difference of two random distributions, defined over the same interval, results in a triangular shape distribution. This provides us with an exact background model, which enables one to easily simulate the “background only” part of the spectra for study purposes. A result of such an exercise is shown on Figure 5.3 part (a) to demonstrate the validity of the background subtraction procedure described above.

For this study the range over which the random distributions are defined was chosen to be 0 to 16000, *i.e.*, equal to the  $16\mu\text{s}$  TDC window which was used in the experiment. The slope

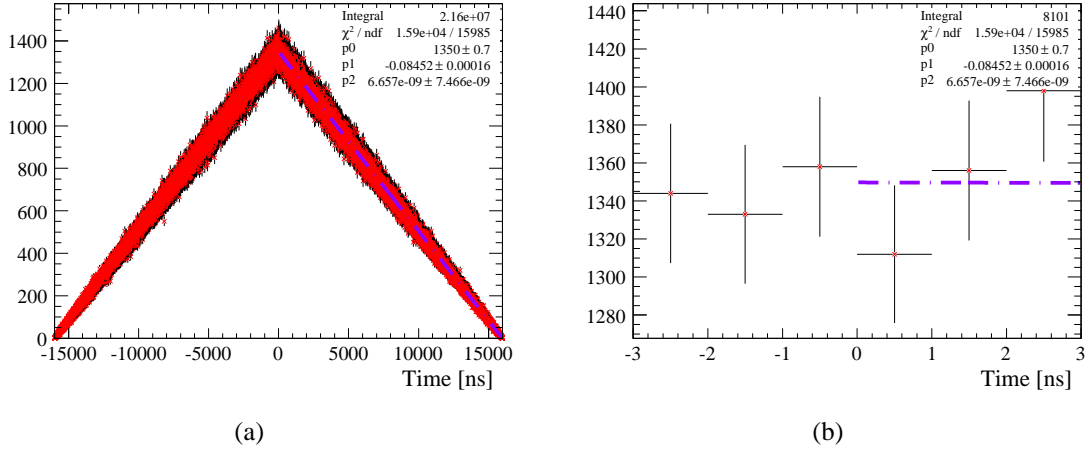


Figure 5.3: (a) Generated background timing spectra. (b) A close up of part (a) showing the  $\pm 3$  ns coincidence region.

of the sides of the triangle depends on the rates of the Tagger and the PS. For the purposes of this simulation the Tagger was allowed to have up to 15 hits per event and the PS was allowed to have up to 7 hits per event. Figure 5.3 part (a) shows a first order polynomial fit to the right side of the triangle. Note that the slope of the generated distribution is more than an order of magnitude larger than the slope obtained from fitting the real experimental background (see Figure 5.2). Such exaggerated slope should help to emphasize the weaknesses (if any) of the background determination procedure in question. Figure 5.3 part (b) shows the coincidence region with  $N_B^i = 8101.00 \pm 90.10$  generated background events. Figure 5.4 parts (a) and (b) show the left and right background windows with  $54010.00 \pm 232.40$  and  $54190.00 \pm 232.79$  events respectively.

Using Equation 5.2 and the values of the integral of events in the left and right background windows, one can calculate the number of background events in the coincidence region to be  $N_B^i = 8115.00 \pm 34.86$ , which is in perfect agreement with the generated number of

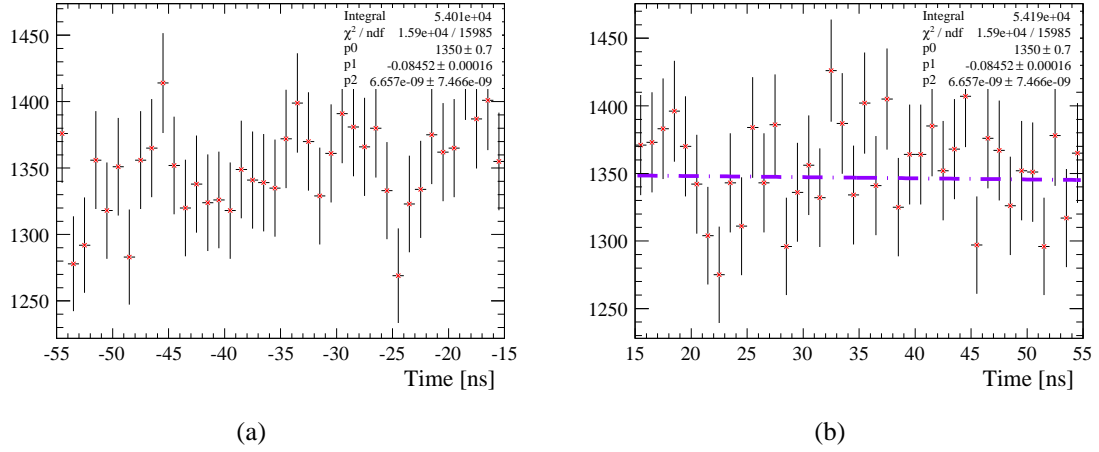


Figure 5.4: (a) Generated events, left background window. (b) Generated events, right background window.

background events  $N_B^i$ .

### 5.3 Effect of Incident Electron Beam Intensity on Relative Tagging Ratios

As discussed in Sections 3.1 and 4.3, the relative tagging ratios, defined by Equation 5.1, can be measured at low as well as at high electron beam intensities. In order to justify the use of the absolute normalization of the photon flux obtained at low electron beam intensities for the calculation of the number of tagged photons on target, it is important to demonstrate the independence of the  $R_{rel}^i$  on the electron beam intensity.

In August 2002, the  $R_{rel}^i$  was measured from 0.08 to 100 nA, the results for T-counter 3 are shown in Figure 5.5. The data points were fitted with a first order polynomial and as can be seen  $R_{rel}^i$  is quite independent of the beam intensity (note that the  $X$ -axis on top plot is presented in *log* scale). The fit parameters for all the T-counters used in the PrimEx experiment are listed in Table 5.1.

Table 5.1: Fit parameters for different T-counters, relative tagging ratio beam intensity (*in*)dependence test

<i>T</i> – counter #	<i>p</i> 0	<i>p</i> 1	$\chi^2/ndf$
1	$0.004598 \pm 1.550 \times 10^{-5}$	$4.542 \times 10^{-7} \pm 2.134 \times 10^{-7}$	5.218/6
2	$0.004585 \pm 1.432 \times 10^{-5}$	$5.768 \times 10^{-8} \pm 1.993 \times 10^{-7}$	7.992/6
3	$0.004528 \pm 1.333 \times 10^{-5}$	$3.046 \times 10^{-7} \pm 1.901 \times 10^{-7}$	2.770/6
4	$0.004425 \pm 1.597 \times 10^{-5}$	$2.100 \times 10^{-7} \pm 2.192 \times 10^{-7}$	12.790/6
5	$0.004372 \pm 1.437 \times 10^{-5}$	$4.183 \times 10^{-8} \pm 1.980 \times 10^{-7}$	3.189/6
6	$0.004249 \pm 1.431 \times 10^{-5}$	$1.947 \times 10^{-7} \pm 1.984 \times 10^{-7}$	16.43/6
7	$0.004104 \pm 1.495 \times 10^{-5}$	$5.934 \times 10^{-7} \pm 2.045 \times 10^{-7}$	3.927/6
8	$0.003974 \pm 1.403 \times 10^{-5}$	$4.382 \times 10^{-7} \pm 1.916 \times 10^{-7}$	12.79/6
9	$0.003859 \pm 1.283 \times 10^{-5}$	$9.129 \times 10^{-7} \pm 1.789 \times 10^{-7}$	4.469/6
10	$0.003685 \pm 1.390 \times 10^{-5}$	$6.149 \times 10^{-7} \pm 1.911 \times 10^{-7}$	11.55/6
11	$0.003519 \pm 1.190 \times 10^{-5}$	$8.079 \times 10^{-7} \pm 1.677 \times 10^{-7}$	10.56/6

In Figure 5.6 the relative tagging ratios are plotted versus T-counter ID, *i.e.*, photon energy, for the data taken in Fall of 2004, over the range of electron beam intensities used in the PrimEx experiment. The error on each point is not larger than 1.1%. The shape of the curve depends on the the setting of the Pair Spectrometer dipole magnet and the geometrical acceptance of Pair Spectrometer detectors. The pair production cross section is practically constant at the energies that are of interest to PrimEx. GEANT simulations show the same general behavior for the energy dependence of  $R_{rel}^i$ .

#### 5.4 Run-to-Run Stability of Relative Tagging Ratios

As previously discussed, the relative tagging ratios have to be not only intensity independent but also stable from run to run, *i.e.*, in time, to within 1%. The time stability of the relative tagging ratios measured by the PS justifies the use of a single set of absolute tagging ratios

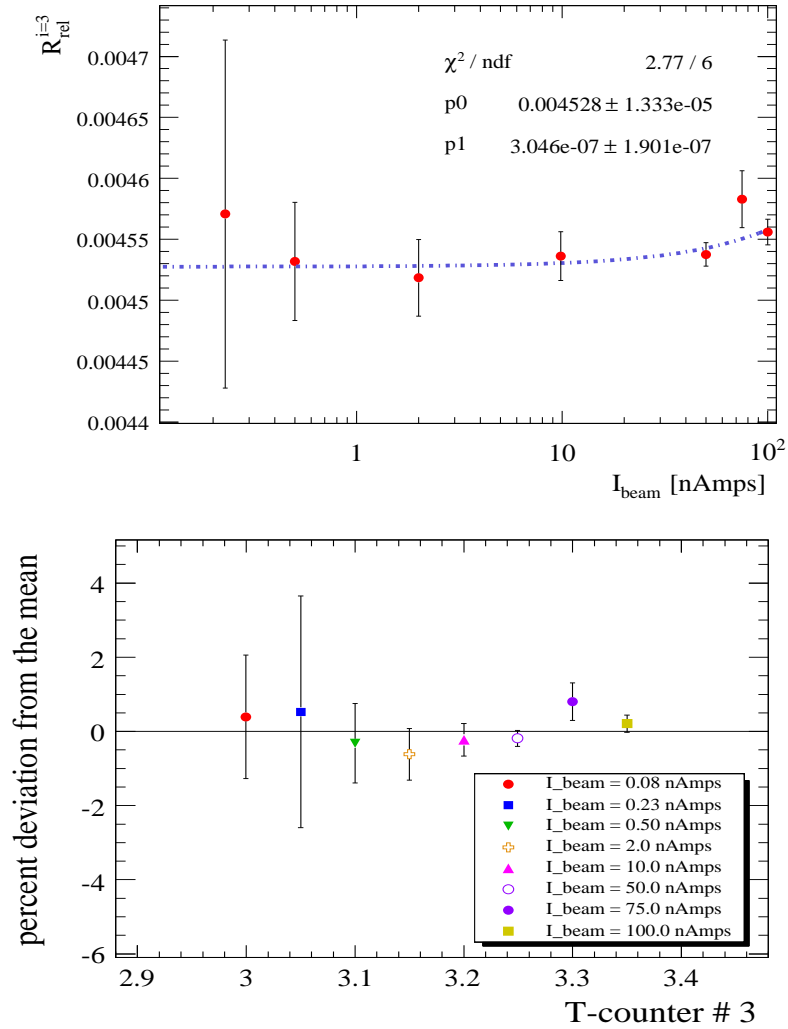


Figure 5.5: (top) Measured  $R_{rel}^i$  for T-counter #3 as a function of nominal electron beam current. (bottom) The percent deviations from the mean for tagging ratio measurements made at different beam intensities for the first eleven T-counters.

measured by the TAC for the tagged photon flux calculation. As such, to achieve a 1% level tagged photon flux measurement any deviation from the nominal value of the  $R_{rel}$  has to be carefully investigated and if possible corrected. In this and the next section the qualitative analysis of the run-to-run stability of the relative tagging ratios will be presented and possible

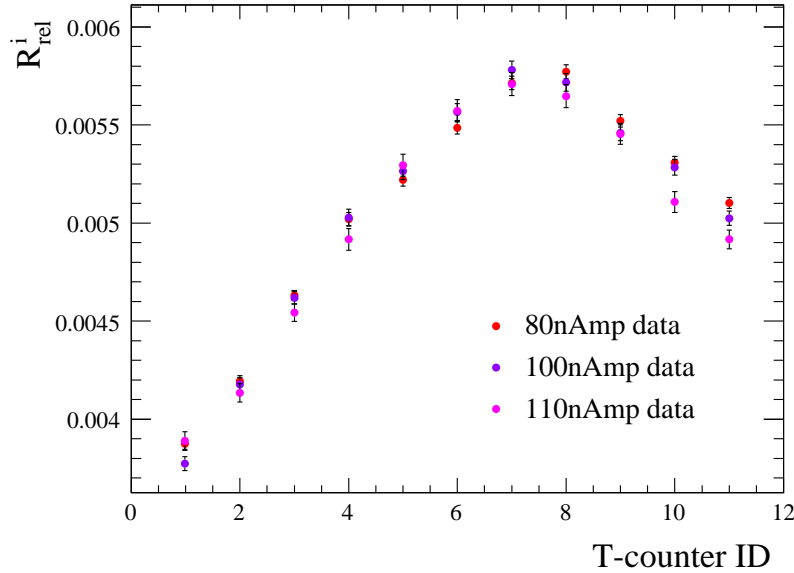


Figure 5.6:  $R_{rel}^i$  measured for three different beam currents across the focal plane of the Tagger. The radiator thickness during these measurements was  $2 \times 10^{-5} X_0$ .

sources for deviations will be discussed. For the purpose of this qualitative discussion the data from all eleven T-counters were combined together and the part of the focal plane of the Tagger that is of interest to the PrimEx experiment is treated as one single counter which enables a reduction in the statistical error.

Figure 5.7 shows the time evolution of the  $R_{rel}^{combined}$  - combined relative tagging ratio in time. The two black solid lines on the graph represent  $\pm 1\%$  deviation from weighted average. The weighted average for the runs with the carbon target is calculated based on runs with run numbers less than 4800 and for lead target runs the average was determined based on the group of runs with Run Numbers from 5050 to 5090 giving for lead runs an average of  $0.00543505 \pm 0.042491\%$  and for carbon runs an average of  $0.00505767 \pm 0.028842\%$ .

It is easy to see that for the last group of runs (run number  $> 5150$ ), the relative tagging

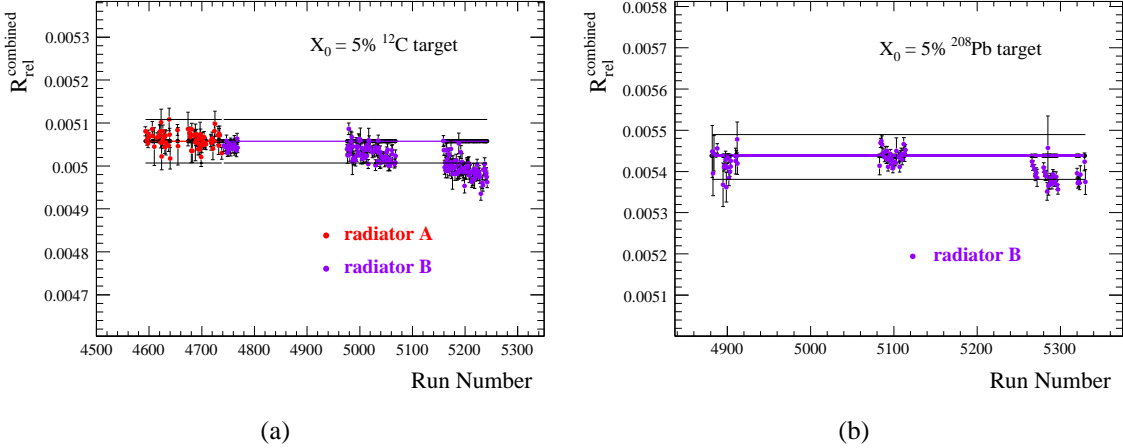


Figure 5.7: Run-to-Run stability of  $R_{rel}^{combined}$  - relative tagging ratio combined for eleven T-counters (a) carbon target. (b) lead target.

ratio starts to fall off. The deviation is larger than 1% and indicates that extra care is needed when calculating the photon flux for this group of runs. I will address this issue in the next two sections.

## 5.5 Inefficiency of Tagger

Before making any corrections one needs to investigate the reason for the drop in relative tagging ratios on Figure 5.7. The  $R_{rel}^{combined}$  can drop due to a number of reasons:

1. The Tagger registers extra electrons which do not have partner photons on our physics target.
2. A part of our photon beam is being lost before reaching the physics target (or TAC since the same effect has been seen in absolute tagging ratios).
3. A combination of first the two effects.

To investigate this drop in relative tagging ratios one can look at the ratio of the number tagged pairs ( $N_{e^+e^-}^{PS}$ ) to the number of all pairs ( $N_{e^+e^-}$ ) and at the ratio of the number of all pairs ( $N_{e^+e^-}^{PS}$ ) to the number of electrons in the tagger ( $N_e^i$ ).

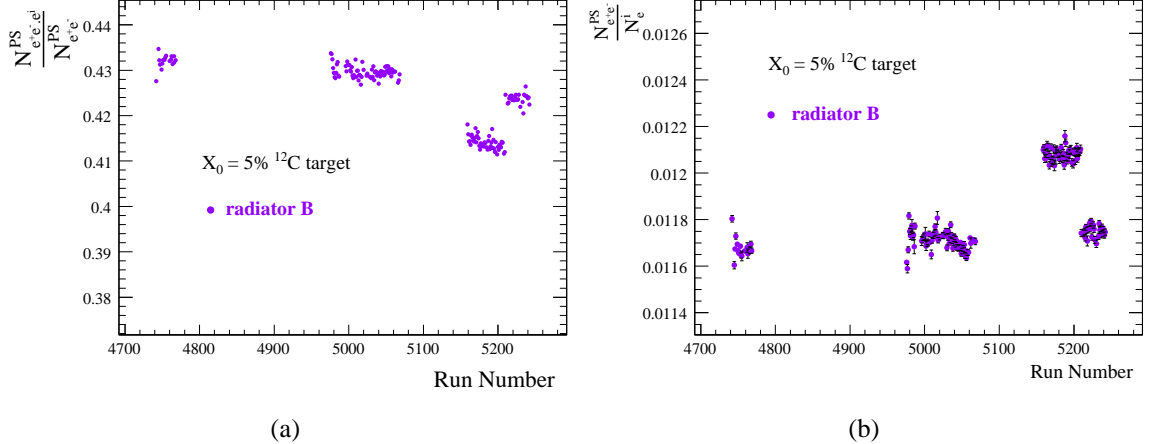


Figure 5.8: (a) Run dependence of  $\sim \frac{\text{tagged } \gamma's}{\text{total } \gamma's}$  combined for eleven T-counters. (b) Run dependence of  $\sim \frac{\text{total } \gamma's}{\text{total } e^-s}$  combined for eleven T-counters.

Keeping in mind Figure 5.7, let us call runs 4747 – 4768 that were taken at  $\sim 80$  nA *group 1*, runs 4978 – 5069 that were taken at  $\sim 100$  nA *group 2*, runs 5158 – 5210 that were taken at  $\sim 130$  nA *group 3* and runs 5211 – 5242 that were taken at  $\sim 110$  nA *group 4*.

In order to understand the beam intensity dependence of these ratios, the weighted averages were calculated for each group. The results are plotted as a function of the electron beam intensity in Figures 5.9, 5.10 and 5.11<sup>2</sup>. Note that the polarity of the PS dipole field was flipped between runs in groups 1 and 2, thus the average values of only groups 2, 3 and 4 should be compared to each other.

<sup>2</sup>On the next three plots groups 3 and 4 appear in reverse order.

In Figure 5.9 there is a drop of 0.46% in relative tagging ratio between groups 2 and 3 (point at 130 nA). Group 4, however, is  $\sim 1.00\%$  lower than group 1 which indicates either a drop in the number of tagged  $e^+e^-$  pairs or an increase in the number of electrons registered in the tagger, possibly both.

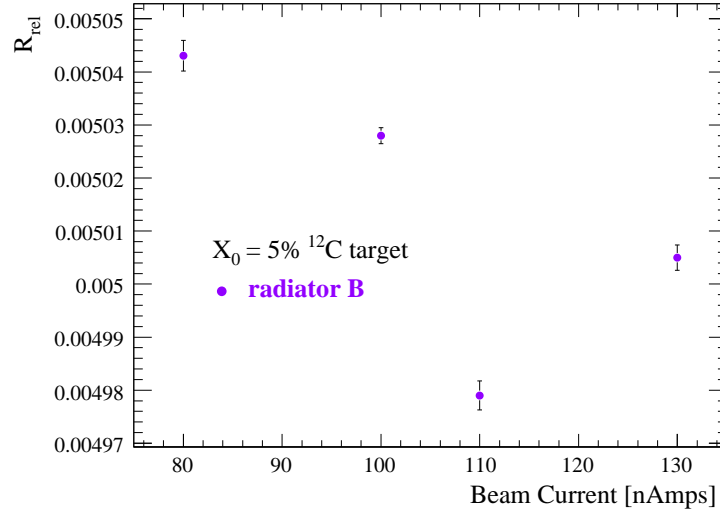


Figure 5.9:  $R_{\text{relative}}$  vs. beam current, combined for eleven T-counters and averaged for all runs with same current. The drop in relative tagging ratios reflects the change in number of electrons in the Tagger.

Figure 5.10 shows a  $\sim 3.52\%$  drop in  $\frac{N_{e^+e^- \cdot e^i}^{PS}}{N_{e^+e^-}^{PS}}$  when going from group 2 to group 3. Note that on this plot group 4 is  $\sim 2.24\%$  higher than group 3, which indicates that in Figure 5.9, the drop in relative tagging ratios for group 4 is due to extra electrons registered in the tagger which have nothing in common with tagged photons on our target. The overall drop in  $\frac{N_{e^+e^- \cdot e^i}^{PS}}{N_{e^+e^-}^{PS}}$  can be explained by a drop in the absolute efficiency (hardware and reconstruction) of the tagging counters with an increase of the beam intensity.

In Figure 5.11 I have plotted the ratio of the number of  $e^+e^-$  pairs registered in the Pair Spectrometer to the number of electrons registered in the tagger. The plot shows a  $\sim 3.16\%$  rise when going from group 2 to group 3, which again could be explained by inefficiency of the tagger at high beam intensities.

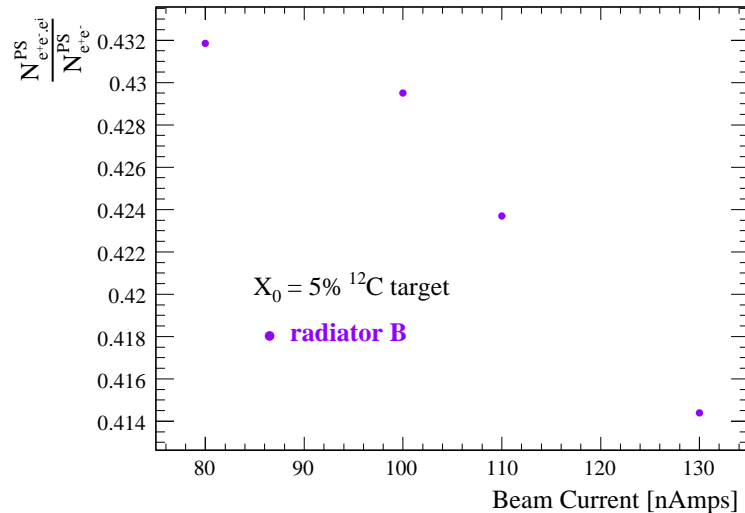


Figure 5.10:  $\frac{\text{tagged } \gamma's}{\text{total } \gamma's}$  vs. beam current, combined for eleven T-counters and averaged for all runs with the same current, reflecting the loss of absolute efficiency of the Tagger.

## 5.6 Correction of Photon Flux for Affected Runs

Figure 5.7 part (a) shows that groups 4 and 3 of runs with the  $^{12}C$  target were influenced by extra electrons (found to be correlated with presence of beam in other Halls) in the tagger. The qualitative study presented in Sections 5.4 and 5.5 indicates that those electrons do not create bremsstrahlung photons on our target. Hence, we need to correct the number of electrons in the tagger when calculating the photon flux for the affected runs.

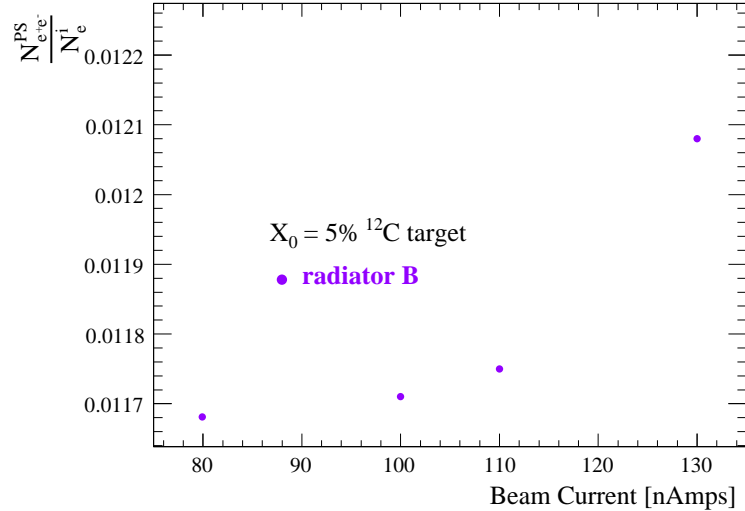


Figure 5.11:  $e^+e^-/e^-$  vs. beam current, combined for eleven T-counters and averaged for all runs with same current, reflecting the loss of absolute efficiency of the Tagger.

For carbon target runs, the nominal values of the relative tagging ratios were obtained by calculating the weighted average for each of eleven T-counters. Runs numbered 4978 through 5069 (group 2) were used for this purpose and the results are presented in Table 5.2.

Table 5.2: The nominal values of  $R_{rel}^i$  for runs with carbon target.

<i>T</i> - counter #	$R_{rel}^i$	error(%)
1	0.00387	$\pm 0.118$
2	0.00421	$\pm 0.107$
3	0.00446	$\pm 0.091$
4	0.00498	$\pm 0.109$
5	0.00525	$\pm 0.102$
6	0.00552	$\pm 0.098$
7	0.00571	$\pm 0.1$
8	0.00569	$\pm 0.1$
9	0.00550	$\pm 0.094$
10	0.00525	$\pm 0.097$
11	0.00501	$\pm 0.092$

Correction coefficients have been obtained by averaging the relative tagging ratios for the runs in the groups 3 and 4 (for each T-counter) and normalizing the weighted average relative tagging ratio for each group to the nominal value for the respective T-counter. The results are presented in Table 5.3.

Table 5.3: The correction factors for carbon target runs; groups 3 and 4.

<i>T – counter #</i>	Group 3		Group 4	
	$R_{rel}^i$	error(%)	$R_{rel}^i$	error(%)
1	1.00051	$\pm 0.213$	0.99631	$\pm 0.246$
2	0.99599	$\pm 0.195$	0.99049	$\pm 0.224$
3	0.99387	$\pm 0.168$	0.98692	$\pm 0.192$
4	0.98801	$\pm 0.198$	0.98601	$\pm 0.228$
5	0.994	$\pm 0.184$	0.99091	$\pm 0.212$
6	0.99339	$\pm 0.178$	0.98839	$\pm 0.204$
7	0.99617	$\pm 0.18$	0.988	$\pm 0.207$
8	0.99438	$\pm 0.181$	0.99104	$\pm 0.208$
9	0.99251	$\pm 0.171$	0.98675	$\pm 0.197$
10	0.99347	$\pm 0.177$	0.99386	$\pm 0.203$
11	0.99591	$\pm 0.168$	0.98115	$\pm 0.193$

From Figure 5.7 part (b) one can see that there are three distinct running periods for the lead target. Let us call runs numbered 4950 and less group 1, runs numbered from 5070 to 5155 group 2 and runs numbered 5250 and up group 3. Using the same method as described above for runs with the carbon target and information from group 2, one can obtain nominal values of relative tagging ratios for lead target runs (see Table 5.4). And based on these nominal values, one can calculate correction factors for group 1 and group 3 of the lead target runs (see Table 5.5).

Table 5.4: The nominal values of  $R_{rel}^i$  for runs with the lead target.

$T - counter \#$	$R_{rel}^i$	error(%)
1	0.00415	$\pm 0.167$
2	0.0045	$\pm 0.152$
3	0.00493	$\pm 0.131$
4	0.00531	$\pm 0.155$
5	0.00563	$\pm 0.143$
6	0.00591	$\pm 0.139$
7	0.00615	$\pm 0.14$
8	0.0062	$\pm 0.14$
9	0.00602	$\pm 0.132$
10	0.00575	$\pm 0.136$
11	0.00549	$\pm 0.13$

Table 5.5: The correction factors for the lead target runs; groups 1 and 3.

	Group 1		Group 3	
$T - \text{counter } \#$	$R_{\text{rel}}^i$	error(%)	$R_{\text{rel}}^i$	error(%)
1	0.9943	$\pm 0.3$	0.99213	$\pm 0.239$
2	0.99764	$\pm 0.272$	0.99616	$\pm 0.218$
3	0.99593	$\pm 0.233$	0.99234	$\pm 0.187$
4	1.00252	$\pm 0.277$	0.99312	$\pm 0.222$
5	0.99283	$\pm 0.258$	0.98806	$\pm 0.206$
6	0.99997	$\pm 0.249$	0.99365	$\pm 0.199$
7	0.99954	$\pm 0.251$	0.99083	$\pm 0.201$
8	0.9937	$\pm 0.252$	0.98926	$\pm 0.201$
9	0.99819	$\pm 0.237$	0.98833	$\pm 0.19$
10	0.9962	$\pm 0.245$	0.98888	$\pm 0.196$
11	0.99683	$\pm 0.233$	0.99103	$\pm 0.186$

Copyright © Aram Teymurazyan 2008

## CHAPTER : 6 NUMBER OF PHOTONS PER RUN PER T-CHANNEL

### 6.1 Detector Rates, Electron Counting

As discussed in Section 3.1, an important component in calculating the photon flux is counting the number of electrons that potentially would be detected by the tagger.

For most tagged photon experiments at JLab including PrimEx, photons are produced at a rate far greater than is practical for measuring directly via the data acquisition system (DAQ), with the exception of TAC calibration runs where the rates are lower by a factor of one thousand.

Traditionally, to measure normalization, hardware scalers are used to count the number of hits in a particular detector. Scalers have the advantage of being able to count virtually all the hits from a detector. Also using scalers to measure the detector rates can automatically account for beam-trips, *i.e.* uncontrolled beam intensity drops or spikes, providing that the scalers count signals from a beam related source, which in general is very beneficial. However the triggering scheme used for the PrimEx experiment and the tagged nature of the  $\pi^0$  yield that we are extracting makes the hardware scaler method unattractive exactly due to the fact that scalers would count all the hits in the tagging counters.

The primary trigger for the PrimEx experiment is formed by a coincidence of signals from the HyCal and the Tagger. If the total energy deposited in the calorimeter exceeds a threshold of 0.5 GeV and there is a signal available from the tagger, a trigger signal is formed which tells the DAQ to read out all the channels that have non-zero information (HyCal, Tagger, PS *etc.*). It is much more efficient to use the HyCal-Tagger coincidence as a primary physics trigger. Using the tagger signal alone would flood the data acquisition due to the high rate of tagging

counter signals, most of which represent photons which just passed through the target without producing a  $\pi^0$ . Figure 6.1 illustrates the basic ideology behind the primary trigger setup for PrimEx experiment.

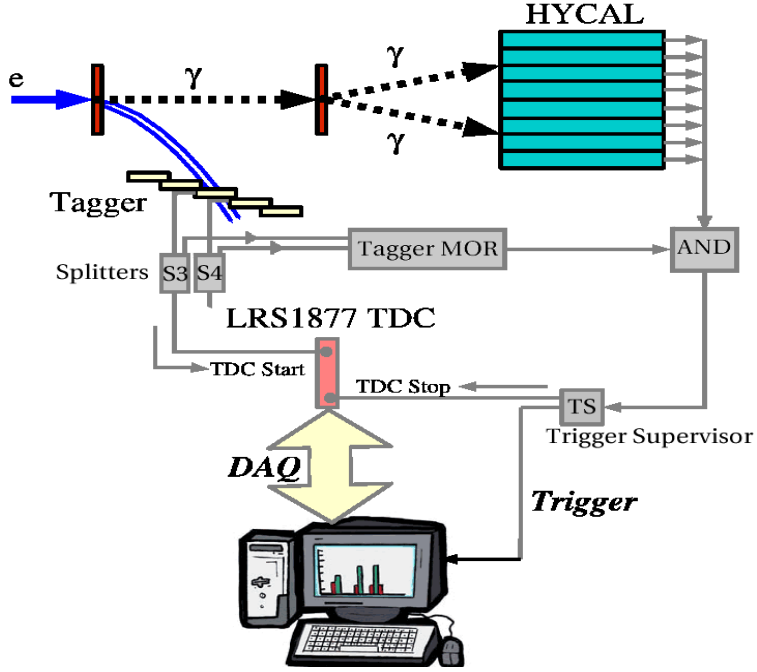


Figure 6.1: Trigger setup schematic

The PrimEx DAQ primarily utilized LeCroy 1877 TDCs. These TDCs have a maximum range of  $32 \mu\text{s}$  and double pulse resolution of  $\sim 20 \text{ ns}$ . The LRS1877's are multi-hit TDCs with the capability of storing up to 16 hits per trigger event per channel in a LIFO (Last In First Out) mode. The range of the TDC and the LIFO limit are programmable and for the PrimEx experiment were set to  $16 \mu\text{s}$  and 10 hits, respectively. For more information on the specifications of the LeCroy 1877 TDC module see Appendix C Section C.1. If the rate of a detector is too high, the older hits are overwritten by more recent ones due to the LIFO limit.

Since only a timing coincidence is required between HyCal and Tagger MOR (OR of

eleven T-counters) signals to form a trigger, there are three scenarios of losing tagged  $\pi^0$  yield due to the TDC dead-time (double pulse resolution) and LIFO limit:

1. An entire event is lost due to TDC dead-time, *i.e.*, there was no signal from tagging counters to form a coincidence with HyCal signal but data acquisition is ready to take data. From the stand point of photon flux calculation, this case is very similar to the situation where the DAQ is busy reading out data and is not accepting any triggers.
2. A photon is lost due to TDC dead-time but a coincidence of another photon from a different tagging counter with a HyCal signal forms a trigger and an event is read out. If a  $\pi^0$  is reconstructed in such an event, it will not satisfy the energy conservation condition and will not contribute to the tagged  $\pi^0$  yield.
3. A photon producing a  $\pi^0$  may be lost due to the LIFO limit but the triggering condition might be satisfied by a signal from another tagging counter. Just like in the previous case such events will not contribute to the tagged yield.

The three situations presented above lead to the conclusion that the photons that are untagged due to TDC dead-time or LIFO limit have no means to produce a tagged pion.

It is worth noting that the majority of the inelastic pions (pions not satisfying the energy conservation condition) are produced by low energy photons which are out of the tagging range of interest and are recorded in the data stream as a result of accidental timing coincidence with a photon in the high energy region of the tagger (first eleven T-counters), *i.e.*, the majority of inelastic events are not a result of TDC dead-time or LIFO limit.

As discussed in Section 3.1, to extract the neutral pion width one is interested only in the number of tagged photons on the target which have the potential to produce a tagged  $\pi^0$ . The

tagged  $\pi^0$  yield automatically includes in it the effects of TDC intrinsic dead-time, LIFO limit and the DAQ readout/dead-time, hence; it is not necessary to correct for the number of the tagged photons lost due to these effects.

The rate of tagged photons can be determined from the timing information, recorded by tagging counters, via sampling of the number of hits for a small fraction of the time. An assumption is then made that these samples are representative of the detectors' responses for the times when no data are recorded. This can be used to extrapolate to all times in order to determine the total number of tagged photons represented by a given data sample. Since one is interested in the number of tagged photons that have the potential to produce a tagged  $\pi^0$ , the timing information from only fully reconstructed hits in the Tagger need to be considered and not just the raw TDC response. A fully reconstructed hit requires a timing coincidence between the left and right PMTs of a T-counter that are simultaneously in time with a hit in an E-counter. The coincidences between “E-” and “T-” counters are also subject to a geometric matching where the two counters are required to be on an electron trajectory which is consistent with the magnetic optics of the Tagger.

The LeCroy 1877 TDCs that the T-counters were equipped with operated in common stop mode during the PrimEx experiment. A T-counter signal passes through a constant fraction discriminator and then is split into two signals. One signal tells the TDC to start a clock and the other signal passes through E-T coincidence/MOR module. Assuming a coincidence between the left and right T-counter PMTs and an E-counter has occurred, the MOR module sends a signal to the trigger supervisor when any E-T coincidence has been obtained. If a signal from HyCal is in coincidence with the MOR signal, the trigger supervisor sends a common stop

trigger signal to all electronics involved in the DAQ to stop counting<sup>1</sup>. Figure 6.2 shows an example of a timing spectrum of hits reconstructed for a single T-counter in the Tagger. Note that the  $X$ -axis in Figure 6.2 part (a) is presented on a log scale. The peak in the timing spectrum at around 100 ns corresponds to the time difference between the two split signals from a single T-counter, *i.e.*, is associated with the events when this particular T-counter was involved in the trigger. The flat accidental background comes from signals that were not involved in the trigger but were accidental hits recorded due to the common stop/multihit nature of T-counter TDCs.

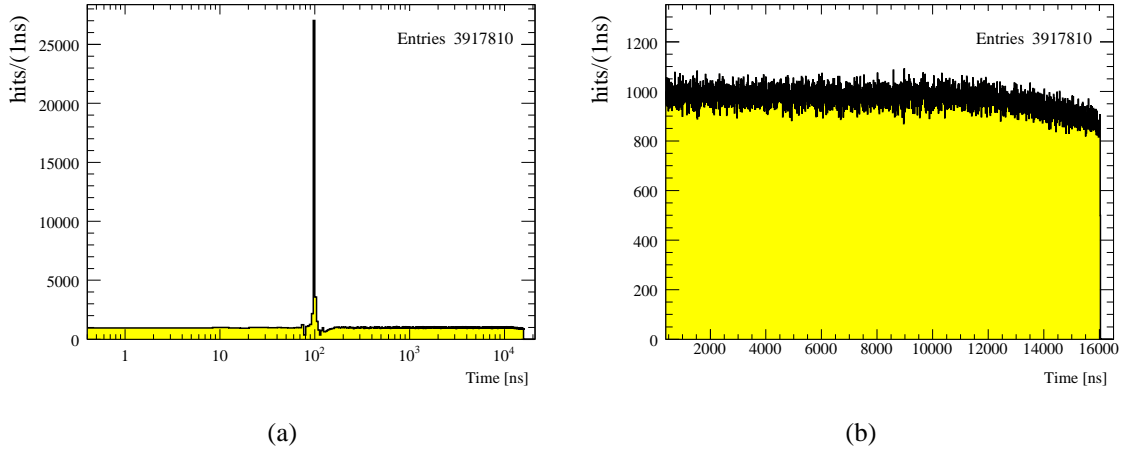


Figure 6.2: (a) Time spectrum of hits reconstructed for a single T-counter.  
 (b) A close up of part (a) illustrating the drop off of the number of hits due to LIFO limit.

One obvious effect seen in Figure 6.2 part (b) is that the number of hits trails off on the right side of the spectrum due to the LIFO limit. Since during the PrimEx experiment the LeCroy 1877's were used in a common stop mode, earlier times are to the right and later times are to the left in this plot. The LeCroy 1877 TDC will always report the latest hits. Thus when

---

<sup>1</sup>See DAQ setups schematic on Figure 6.1.

the LIFO fills up, the earlier hits are overwritten by later ones.

The photon flux at the target as a function of energy is determined by means of sampling the “Out-of-Time” (OOT) electron hits in the Tagger T-counters. The term “Out-of-Time” electron refers to any fully reconstructed electron which was not involved in the formation of the trigger signal. The idea is to simply count the number of hits in a particular T-counter within some user defined time window  $w$  and divide by the size of the time window. Since even high rate detectors on average tend to have only a few hits per event, it is necessary to integrate over many events to obtain an accurate value for the rate.

An important thing to keep in mind when counting hits is to discard hits that could be associated with the trigger. Hits which are correlated with the trigger are biased and will artificially increase the calculated rate. The OOT window- $w$  should be defined in such a manner that it does not include the trigger coincidence peak region but can include areas both before and after the trigger peak. The rate sampling technique with the described triggering scheme is potentially vulnerable to beam intensity variations since it will tend to sample more often when the beam intensity is higher.

To ensure that the calculated rates are not biased by beam intensity variations for the PrimEx experiment, in addition to the primary “physics” trigger the DAQ read-out was triggered by a  $195\text{kHz}$  clock which is completely uncorrelated with the electron beam intensity. The clock triggers are pre-scaled so that the data are dominated by events of physics type that are of interest. The pre-scale factor depends on the electron beam intensity and on the type of the data taking run, *i.e.*, pion photo-production, Compton effect or pair production. Figure 6.3 shows a sample timing distribution for hits reconstructed in a single T-counter recorded with

the clock trigger. As in case of Tagger MOR-HyCal coincidence trigger one can see a depletion of hits due to the LIFO limit starting at around  $10 \mu\text{s}$ , but the peak characteristic to a beam related trigger is missing due to the absence of trigger-beam correlation.

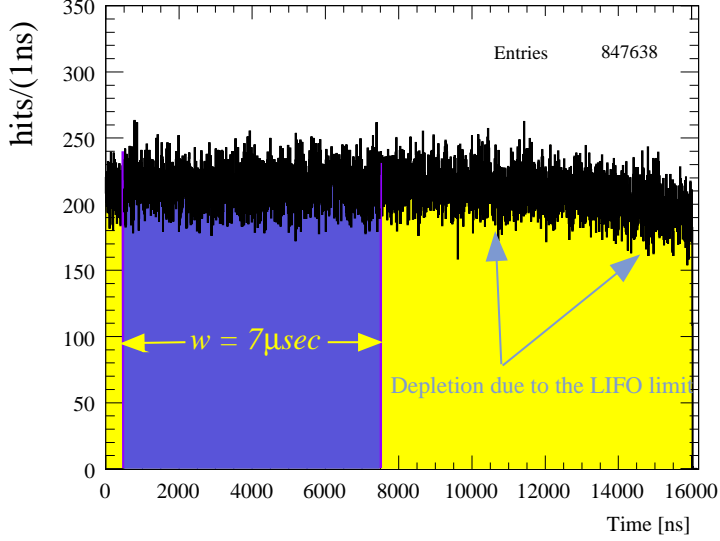


Figure 6.3: Timing spectrum of hits reconstructed for a single T-counter.  
These data were taken with clock triggers

The same OOT window— $w$ , shown on Figure 6.3, is used when calculating the rates with either clock or physics triggers. It was chosen to be  $7\mu\text{s}$  for all T-counters spanning from 500 to 7500 ns and thus avoiding the coincidence peak in case of MOR-HyCal coincidence trigger and the region affected by LIFO limit for both triggers. Extra effort has been put into checking that the distribution of hits inside the OOT window is flat. Any deviation from a flat distribution inside of this window is indicative of a potential problem.

Following the above described recipe for an electron rate calculation we have:

$$r^i = \frac{n_e^i}{w \cdot n_{trigger}} \quad (6.1)$$

where  $r^i$  is the rate of T-counter  $i$ ,  $n_e^i$  is the number of hits within the OOT window of width  $w$  and  $n_{trigger}$  number of times the T-counter  $i$  could have had a hit, *i.e.*, the number of triggers.

Equation 6.1 assumes Poisson statistics for “out of time” electrons and it means that we assume constant electron rate per T-counter.

The PrimEx experiment used a second generation of the JLab designed Trigger Supervisor (*TS*) module [29]. This module is designed specifically to optimize event rates for Fastbus and VME based DAQ systems like those commonly used in intermediate and high energy physics experiments. One new feature in the second generation model is the inclusion of two scalers dedicated to measure the live-time of the DAQ. Both scalers are driven by a  $195.3160 \pm 0.0045$  kHz internal clock. One of this scalers is live-time gated while the other is free-running. The ratio of the two gives the fractional live-time of the DAQ.

In reality one is really only interested in the final number of the hits a detector has seen during the live-time of the data sample. This can be obtained using only the live-time gated scaler to calculate the actual live-time as shown below, *i.e.*, the free running scaler is not really needed since both the  $\pi^0$  yield and the photon flux are affected by the DAQ dead time in the same way:

$$T_{live} = n_{gated} \cdot \beta \quad (6.2)$$

where  $n_{gated}$  is the number of scaler counts from the gated TS scaler and  $\beta = \frac{1}{clock\ frequency}$ , *i.e.*,  $\beta = 5119.9083 \pm 0.0002$  ns.

Given Equation 6.2, the total number of electrons that have passed through a T-counter  $i$

during the time the DAQ was live is expressed by:

$$N_e^i = r^i \cdot T_{live} = \frac{n_e^i}{w \cdot n_{trigger}} \cdot n_{gated} \cdot \beta \quad (6.3)$$

The number of tagged photons  $N_\gamma^i$  per T-channel  $i$  can be calculated as:

$$N_\gamma^i = N_e^i \cdot R_{absolute}^i \quad (6.4)$$

where  $N_e^i$  is the number of electrons per T-channel  $i$  and  $R_{absolute}^i$  is the tagging ratio, which is determined in the TAC analysis.

The rate calculation method described in this section is sometimes called the “Integral Method” for electron counting by sampling out of time hits. An alternative method as well as the advantage of the “Integral Method” for the PrimEx experiment are discussed in Section 6.4.

## 6.2 Beam Trip Accounting

As previously mentioned Equation 6.1 is valid only in the case of a constant rate. Also since

the live-time of this experiment is measured via two scalers which are driven by a clock rather than a beam related source, any uncontrolled variations of beam current, *i.e.* beam trips, must be properly identified and discarded during the data analysis. One of the scalers is free running and the other is DAQ live-time gated. The values of these scalers are read out with every event.

If we denote the reading of the free running scaler during event  $k$  by  $n_{free}^k$ , and the reading of the live-time gated scaler by  $n_{gated}^k$  then  $\Delta n_{free} - \Delta n_{gated} = n_{free}^k - n_{free}^{k-1} - (n_{gated}^k - n_{gated}^{k-1})$  gives us the absolute measure of DAQ dead-time per event in scaler counts. Figure 6.4 shows a histogram of this quantity and suggests that the DAQ for the PrimEx experiment to a very

good approximation has a fixed dead time per event of  $\sim 5.4$  scaler counts (or  $\sim 28\mu\text{s}$ ) if the rate of events is constant.

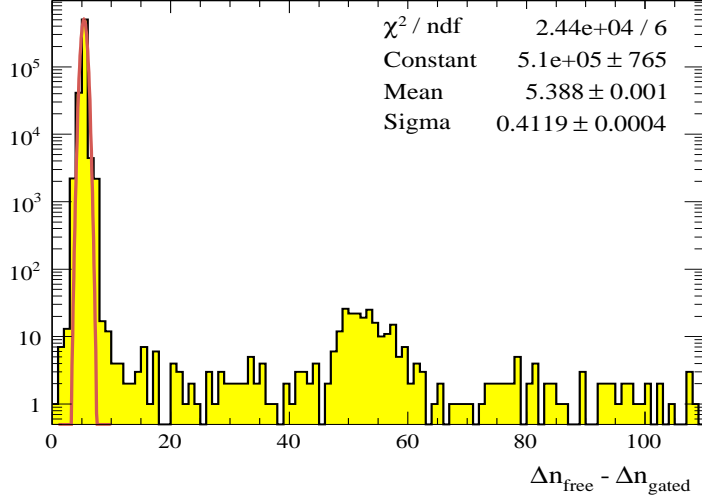


Figure 6.4: DAQ dead-time per event for run 5159

Figure 6.5 is a screen-shot, taken during Fall 2004 PrimEx running period, illustrating the scale of time over which the beam intensity and position are relatively stable.

To simulate a constant electron rate a run is divided into five second time intervals<sup>2</sup>. Having a fixed dead-time per event, one would expect a constant live-time for the DAQ if the rate of events is constant. Figure 6.6 shows the fractional live-time, *i.e.* the ratio  $\frac{\Delta n_{gated}}{\Delta n_{free}}$ , where corresponding increments of  $\Delta n_{gated}$  and  $\Delta n_{free}$  are calculated with respect to the start and end of each five second interval. As one can see there are two distinct peaks at  $\sim 0.96$  and at  $\sim 0.999$  corresponding to “normal” and “no-beam” running conditions respectively.

Figure 6.7 shows the correlation of the fractional live-time with the number of electrons

---

<sup>2</sup>Hereafter when talking about run intervals a five second long interval should be understood unless otherwise stated.

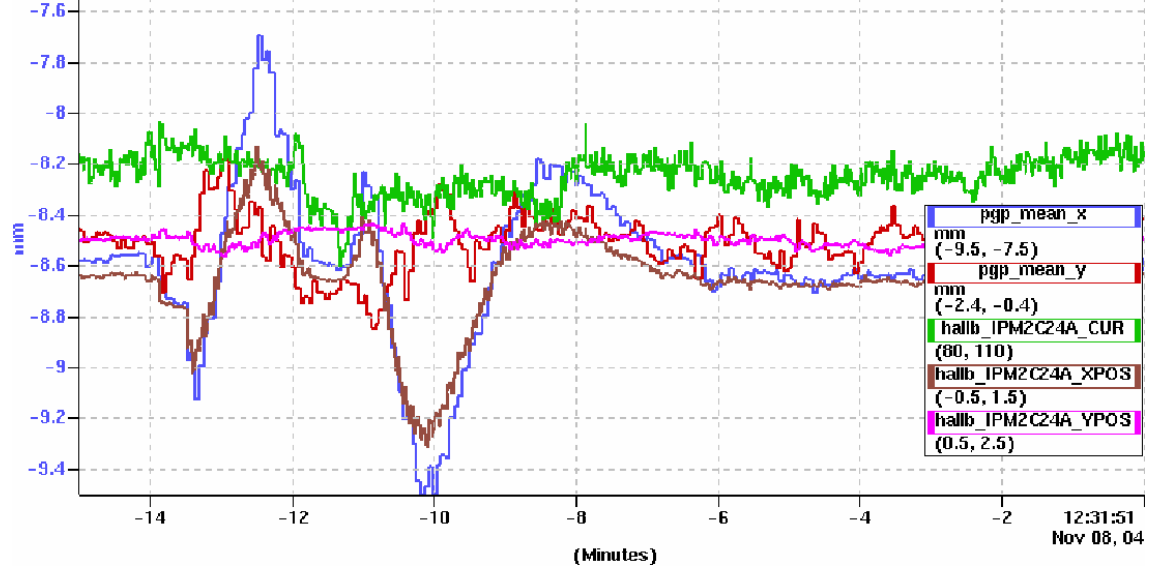


Figure 6.5: A snap-shot of a screen in the experimental control room during the PrimEx run showing: beam current (green),  $\gamma$  beam  $X$  position after HyCal (blue),  $\gamma$  beam  $Y$  position after HyCal (light brown),  $e^-$  beam  $X$  position before radiator (dark brown) and  $e^-$  beam  $Y$  position before radiator (pink)

in one of the T-counters, which is in turn proportional to the electron beam intensity. From this plot it is obvious that whenever the intensity of the beam drops the live-time rises and the increase in electron beam intensity corresponds to a drop of DAQ live-time. This observation enables the use of a very simple scheme for identifying the beam trips and eliminating them from the data sample. For each of the runs, a histogram of fractional live-time is fitted with a Gaussian to find the nominal value for the live-time. The half-width  $\sigma$  of the Gaussian is used to identify a region of width  $2m \cdot \sigma$ . Any five second long interval of the run with fractional live-time outside of the  $\pm m \cdot \sigma$  region centered on the nominal value is discarded, where  $m$  is a parameter and can be varied for optimization. Cutting out intervals where the beam intensity has dropped to zero has no effect on the statistics of the experiment and only discarding the

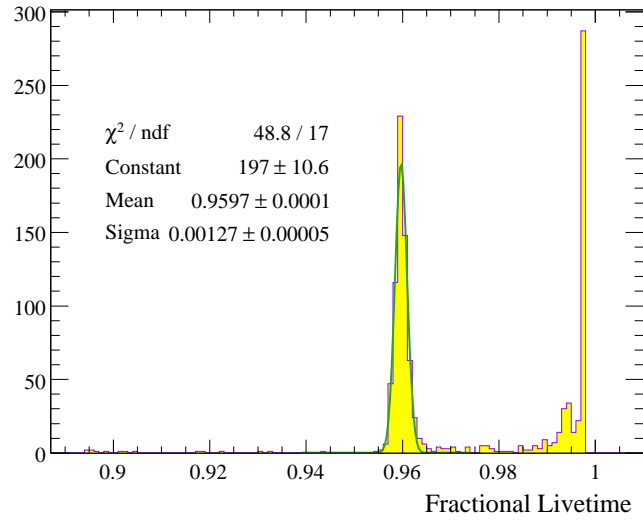


Figure 6.6: Fractional live-time for run 5159.

intervals where the beam intensity has spiked will reduce the statistics. This scheme, with  $m = 3$  has been used to mark the intervals good (green) or bad (red) in Figure 6.7.

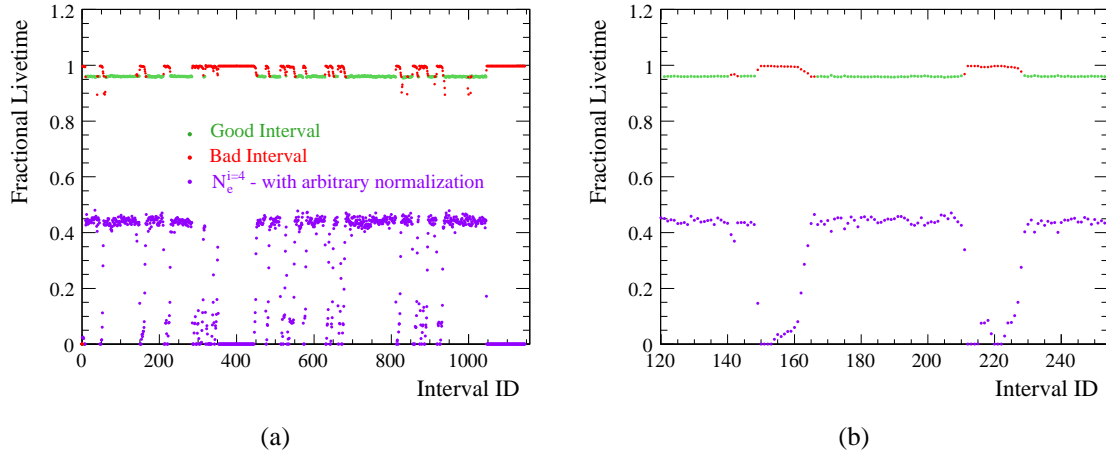


Figure 6.7: (a) Correlation of fractional live-time and number of electrons in T-counter #4. (b) A close up of part (a).

The rate of electrons for each five second interval can be calculated. Two histograms of rates of five second intervals of run number 5159 are shown on Figure 6.8. The green histogram, with mean value of 4.11 a.u. corresponds to intervals that passed the  $3\sigma$  cut on live-time histogram (see Figure 6.6) and red the histogram, with mean at 1.04 a.u. and most of its entries at 0 due to lack of beam, corresponds to intervals outside of the  $3\sigma$  cut.

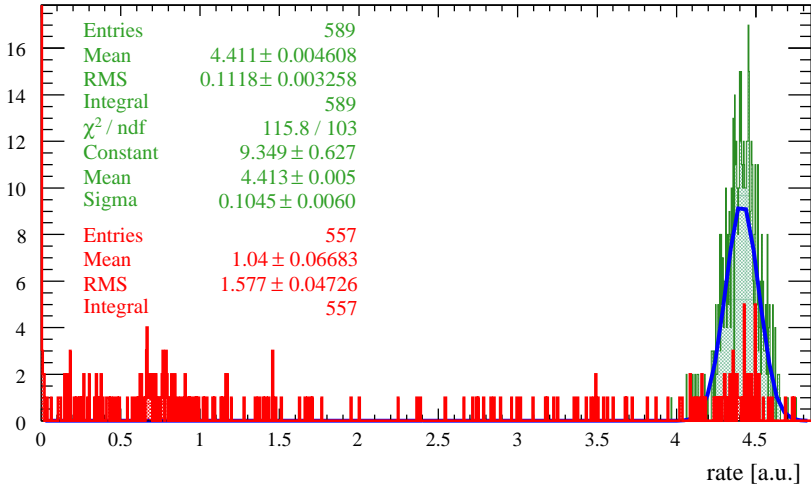


Figure 6.8: Number of counts in T-counter #5 per trigger recorded in a  $7 \mu\text{s}$  window for run 5159.

The number of tagged photons  $N_\gamma^i$  per T-counter is calculated for each five second interval and the total number of photons is obtained by summing over all intervals.

$$N_\gamma^i = \sum_{id} N_{\gamma, id}^i = R_{absolute}^i \cdot \sum_{id} N_{e, id}^i = R_{absolute}^i \cdot \sum_{id} (r \cdot T_{live})_{id} \quad (6.5)$$

### 6.3 Photon flux per E-channel, ET matrix

Equation 6.5 allows one to calculate the total number of tagged photons that have passed through T-counter  $i$  during the DAQ live time per running period. To obtain a total normalization for the run, one can sum over all T-counters. However, the binning of the photon flux according to T-counters is not useful for any kind of energy dependent study. Given the definition of T-counters<sup>3</sup>, they do not overlap, meaning that no photon shares two T-counters. And by the definition of E-channels no two channels can share the same photon. Two T-counters, though, share some of the corresponding E-channels due to the geometry of the Tagger and multiple scattering of the electrons, which creates overlapping energy acceptances of the T-counters. Figure 6.9 illustrates the correlation of the T-counters and E-channels.

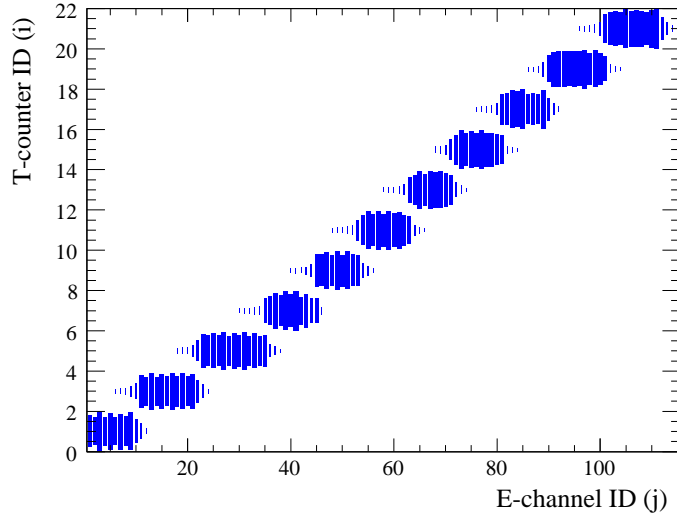


Figure 6.9: E - T matrix, showing the correlation of hits in T-counters to the hits in E-channels.

The 2-D histogram in Figure 6.9 is obtained from real data.

---

<sup>3</sup>For the definition of T-counters, *i.e.* combined T-channels, see Figure 4.1.

Introducing “E-T” coefficients:

$$C^{ji} = \frac{n^{ji}}{n^i} \quad (6.6)$$

where:  $n^i$  is the number of electrons that are registered by T-counter  $i$  and  $n^{ji}$  is the number of electrons registered by T-counter  $i$  that were also registered by E-channel  $j$ . Defined in this manner,  $C^{ji}$  is the probability of an electron that was registered by T-counter  $i$  to be registered by E-channel  $j$ . Note that by definition  $\sum_j C^{ij} = 1$ .

One can easily rebin the photon flux into E-channel bins:

$$N_\gamma^j = \sum_i C^{ji} \cdot N_\gamma^i \quad (6.7)$$

where  $N_\gamma^j$  is the number of photons in E-channel  $j$  and  $N_\gamma^i$  is the number of photons in T-counter  $i$ . Having the flux binned in E-channel bins one can obtain arbitrary non-overlapping energy binning by combining E-channel bins.

Note that the  $C^{ji}$  coefficients depend on the efficiency of the E-counters, but do not depend on the efficiencies of T-counters. To ensure a proper transition from T-counter binning of the photon flux to E-channel binning, frequent recalculation of  $C^{ji}$  coefficients is needed, since the efficiency of E-counters might change over time and/or depending on running conditions. For the PrimEx experiment the E-T coefficients are recalculated every run.

#### 6.4 Error Analysis

The photon flux calculation for the PrimEx experiment is done in two stages. First the absolute tagging ratio is extracted from TAC runs, and then the number of electrons in the run is

calculated. The number of the tagged photons is determined according to Equation 6.4. I will discuss the error evaluation in the same order.

Error in absolute tagging ratio ( $R_{absolute}$ ): Since the numerator and the denominator of the absolute tagging ratio (see Equation 3.2) are not independent, the ordinary formulas for error propagation cannot be used. The error in absolute tagging ratio for each run and each T-counter is calculated according to Equation A.4. As has already been discussed in Section 4.10, the results from eleven runs were combined by calculating the weighted averages following Equations B.1 and B.2 to obtain the absolute tagging ratios applied throughout the data-set (see Table 4.10). It is worth noting that the statistical error on absolute tagging ratios is not larger than 0.06%.

The effects that can change the tagging ratios are the beam tune and the room background (which in turn is dependent on beam tune). It is impossible to study one effect without changing the other. Keeping this in mind, let us take a closer look at the systematic effects that are reflected in the values of absolute tagging ratios discussed in Chapter 4: the scraping of the beam on collimator, the scraping on the HyCal and the reproducibility of the absolute tagging ratios.

The calibration runs with the TAC are performed at a reduced intensity and the position control at typical intensities of TAC runs of  $\sim 80$  pA is poor. The desired beam position is set prior to reducing the beam intensity but the possible fluctuations of the beam position cannot be controlled during the measurement.

The study of photon beam obstruction by HyCal described in Section 4.6 was performed

with an uncollimated photon beam. The relative values of the uncertainties obtained as standard deviations are shown in Table 6.1 for different T-counters.

Table 6.1: Relative uncertainty in tagging efficiency due to HyCal scraping in case of beam mis-steering.

Tcounter ID	1	2	3	4	5	6	7	8	9	10	11
Error (%)	0.18	0.04	0.37	0.35	0.01	0.23	0.12	0.18	0.04	0.27	0.12

The beam was steered 5 mm in the positive Y or 5 mm in the negative X directions off the nominal position at the profiler to observe this change in  $R_{absolute}$ . As seen on Figure 6.5 and from the analysis of beam position stability[30] the 5 mm, measured by the Gamma Profiler behind the HyCal, is an artificially large shift in photon beam position. This study places an upper limit of  $\sim 0.35\%$  on the uncertainty of absolute tagging ratio due to scraping of HyCal.

Short and long term reproducibility studies (see Section 4.7) of absolute tagging ratios with an uncollimated beam yield the following uncertainties in absolute tagging ratios for different T-counters:

Table 6.2: Relative uncertainty in tagging efficiency due to short and long term reproducibility.

Tcounter ID	1	2	3	4	5	6	7	8	9	10	11
Error (%) short term stability	0.30	0.25	0.13	0.15	0.12	0.22	0.22	0.10	0.13	0.06	0.11
Error (%) long term stability	0.04	0.14	0.29	0.16	0.07	0.30	0.18	0.14	0.06	0.06	0.07

Since the reproducibility studies were performed with an uncollimated beam, the only possible obstruction on the path of the photons is the HyCal. Hence the reproducibility studies address the effects of room background and HyCal scraping due to beam position fluctuations.

The uncertainty in absolute tagging ratios of  $\sim 0.30\%$  resulting from this study is consistent with the upper limit of uncertainty obtained from the HyCal scraping study.

During the PrimEx data taking, the photon beam was collimated. The nominal value of  $7.02''$  for the position of the  $12.7\text{mm}$  collimator was determined by moving the collimator in the horizontal direction while the beam position was fixed. As described in Section 4.5, changing the collimator position by  $\sim 1.3$  mm to  $7.07''$  has noticeable effects<sup>4</sup> on the absolute tagging ratios (see Table 6.3):

Table 6.3: Relative uncertainty in tagging efficiency due to collimator scraping in case of beam missteering

Tcounter ID	1	2	3	4	5	6	7	8	9	10	11
Error (%)	0.46	0.12	0.08	0.36	0.31	0.32	0.34	0.21	0.11	0.35	0.15

The results of this study indicate that if the position of the beam would change by  $\sim 1.3$  mm with respect to the collimator that would result in a  $\sim 0.45\%$  change in the absolute tagging ratios. Since the reproducibility studies were done with an uncollimated photon beam this needs to be included in the final error of  $R_{absolute}$ .

Error in number of electrons per run ( $N_e^i$ ): To calculate the number of electrons per run the number of electrons is first calculated per interval of a run according to Equation 6.3 which can be re-written in the following form:

$$N_{e, id}^i = r_{id}^i \cdot T_{live, id} = r_{id}^i \cdot n_{gated, id} \cdot \beta$$

Leading to an error:

---

<sup>4</sup>The deviations measured with collimator at  $7.15''$  (a shift of  $\sim 3.3$  mm) are very similar.

$$\frac{\delta N_{e, id}^i}{N_{e, id}^i} = \sqrt{\left(\frac{\delta r_{id}^i}{r_{id}^i}\right)^2 + \left(\frac{\delta T_{live, id}}{T_{live, id}}\right)^2} = \sqrt{\left(\frac{\delta r_{id}^i}{r_{id}^i}\right)^2 + \left(\frac{\delta n_{gated, id}}{n_{gated, id}}\right)^2} \quad (6.8)$$

The error in  $\beta$  was determined from the specifications of the JLab second generation Trigger Supervisor module and also via direct measurement. Both methods yield a value of  $\sim 4 \times 10^{-6}\%$  which is negligible.

The error in  $n_{gated}$  is purely statistical in nature. The PrimEx experiment ran with DAQ live-time greater than 94%, and given the frequency of the clock driving the gated and ungated scalers, the error in  $n_{gated}$  for a five second interval of a run is on the order of 0.03% or smaller. This error can be further reduced by combining data into intervals longer than 5 s.

In any given time interval  $w$ , the probability of observing any specific number of counts  $x_i$  is given by the Poisson probability function, with mean  $\mu_w = r \cdot w$ , where the subscript  $w$  indicates that these are average values for the time interval of length  $w$  and  $r$  is the average rate of counts. Thus, if one makes  $n$  measurements of the number of counts  $x_i$  recorded each time interval would follow the Poissonian distribution with a mean  $\mu_w$ . The mean value  $\mu_w$  can be obtained by fitting the histogram. Also it is known that the maximum likelihood value of  $\mu_w$  of the Poisson distribution of which the  $x_i$  are representative is given by:

$$\hat{\mu}_w = \bar{x}_w = \frac{1}{n} \sum_{i=1}^n x_i \quad (6.9)$$

Using the fact that the variance  $\sigma^2$  for a Poisson distribution is equal to the mean  $\sigma_w^2 = \mu_w$  the uncertainty in the mean  $\sigma_{w\mu}$  can be obtained using Equation B.2:

$$\sigma_{w_\mu}^2 = \frac{1}{\sum_{i=1}^n 1/\sigma_w^2} = \frac{\sigma_w^2}{n} \simeq \frac{\hat{\mu}_w}{n} \quad (6.10)$$

Usually, as in case of the PrimEx experiment, one is interested in the average number of counts per unit time:

$$r = \frac{\mu_w}{w} \quad (6.11)$$

with uncertainty:

$$dr = \frac{\sigma_{w_\mu}}{w} = \frac{1}{w} \sqrt{\frac{\mu_w}{n}} \quad (6.12)$$

The above described procedure for obtaining the rate at which counts are detected is sometimes called the Poisson method for rate calculation.

Using the terminology introduced in Section 6.1  $n = n_{trigger}$  and  $\sum_{i=1}^{n_{trigger}} x_i = n_e$  one can see that Equation 6.11 is identical to Equation 6.1 with  $dr = \frac{\sqrt{n_e}}{w \cdot n_{trigger}}$ , i.e. the Integral method for rate calculation is a limiting case of the Poisson method. The fact that the Integral method does not require any fitting and is much faster makes it very attractive.

Combining Equations 6.11 and 6.12 one has  $\frac{dr}{r} = \frac{1}{\sqrt{n_e}}$  for the relative error in rate calculation which can be used in Equation 6.8.

Figure 6.10 shows the distribution of number of counts within a  $7 \mu\text{s}$  window recorded per trigger event in T-counter #5. This is a typical distribution accumulated over a 5 second interval of a  $\sim 100 \text{ nA}$  run. One also can see that the results of a Poisson fit are in perfect agreement with the mean value and the integral of the histogram obtained as arithmetic average, which is equivalent to agreement between Integral and Poisson methods for rate calculation.

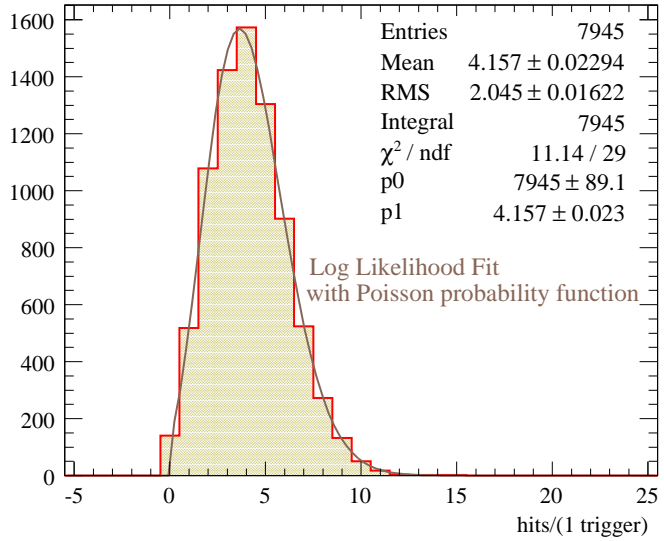


Figure 6.10: Distribution of number of hits per trigger event in T-counter #5 for run 5159.

As discussed in Section 6.1, the electron counting for the PrimEx experiment is done with two independent triggering schemes. The sampling technique for rate calculation can be biased if the beam intensity is changing with time and the sampling rate is intensity dependent as is the case with using the physics trigger and out-of-time hits. The level of beam intensity variation is controlled by dividing a run into five second intervals. Figure 6.8 shows that after discarding the beam trips the rate in the T-counters, which is proportional to beam intensity, is not changing more than 5 – 7% for the entire duration of the run. Assuming that the T-counter rates, within five second intervals, are at least as stable one can use Equations F.5 and F.7 to evaluate the error arising from oscillating and/or drifting beam intensity to be on the order of  $\sim 0.74\%$ . Comparing the results for electron counting from biased physics and unbiased clock triggers one has a difference on the order of  $\sim 0.77\%$  which is easily explained within the limits of the qualitative exercise of Appendix F. In the absence of a precise model/picture

of beam intensity time dependence, it will be fair to attribute a 0.80% systematic error to the electron counting technique.

Putting it all together Having calculated the error in number of electrons per 5 second interval of a run, the error propagation is straightforward.

$$N_\gamma^i = R_{absolute}^i \cdot \sum_{id} N_{e, id}^i \Rightarrow \frac{\delta N_\gamma^i}{N_\gamma^i} = \sqrt{\left(\frac{\delta R_{absolute}^i}{R_{absolute}^i}\right)^2 + \left(\frac{\delta N_e^i}{N_e^i}\right)^2} \quad (6.13)$$

where:

$$N_e^i = \sum_{id} N_{e, id}^i \Rightarrow \delta N_e^i = \sqrt{\sum_{id} (\delta N_{e, id}^i)^2} \quad (6.14)$$

and:

$$N_{e, id}^i = r_{id}^i \cdot n_{gated, id} \cdot \beta \Rightarrow \frac{\delta N_{e, id}^i}{N_{e, id}^i} = \sqrt{\frac{1}{n_{e, id}^i} + \left(\frac{\delta n_{gated, id}}{n_{gated, id}}\right)^2} \quad (6.15)$$

Equation 6.13 gives the number of photons and its error per T-counter. Redistributing the photon flux into non-overlapping energy bins according to Equation 6.7 introduces additional error which can be accounted for by adding it in quadrature due to the multiplicative nature of “E-T” coefficients:

$$N_\gamma^j = \sum_i C^{ji} \cdot N_\gamma^i \quad \Rightarrow \quad \delta N_\gamma^j = \sqrt{\sum_i \left\{ (N_\gamma^i \cdot dC^{ji})^2 + (C^{ji} \cdot dN_\gamma^i)^2 \right\}} \quad (6.16)$$

where  $N_\gamma^j$  is the number of photons per E-channel  $j$  and “E-T” coefficients  $C^{ji}$  are defined according to Equation 6.6. Due to the correlated nature of the numerator and the denominator of Equation 6.6 the error  $dC^{ji}$  of “E-T” coefficients has to be calculated according to formulas derived in Appendix A.

## 6.5 Summary

Given the above considerations the flux error budget is as follows:

	Effect	Error (%)
Statistical	Leakage current correction	< 0.3
	$R_{absolute}$ (TAC)	< 0.06
	Electron counting statistics	run dependent, ( <i>small</i> )
Systematic	Electron counting systematics	0.80 (conservative)
	$R_{absolute}$ reproducibility	0.30
	Beam position/collimation effect on $R_{absolute}$	0.45
	Absorption in TAC runs	negligible
Total		$\sim 1.0$

## CHAPTER : 7 A PRECISION MEASUREMENT OF PAIR-PRODUCTION CROSS-SECTION

### 7.1 Motivation

The goal of the PrimEx experiment, to measure the cross-section for the photo-production of neutral pions in the Coulomb field of a nucleus with a precision of  $\sim 1.4\%$ , sets unprecedented requirements on the photon tagging technique in regards to the determination of the absolute tagged photon flux.

The PrimEx experimental setup, with its new state of the art hybrid calorimeter (HyCal), provides a unique opportunity to verify the flux normalization procedure, described in previous chapters, by measuring the absolute cross-section for a well known electromagnetic process, such as  $(e^+ e^-)$  pair-production, without any additional hardware development.

### 7.2 Theoretical considerations

Cross-section calculations for the photo-production of  $e^+ e^-$  pairs on  $^{12}_6C$  at photon energies of a few  $GeV$  and small momentum transfer  $|\vec{Q}| \sim 10 \text{ keV}$  relevant for the PrimEx experiment were provided by A. Korchin<sup>1</sup>[31]. The detailed discussion of the calculations is outside of the scope of this dissertation, however for completeness a summary of different contributions included in the cross-section calculation is given below in decreasing order of significance:

- Bethe-Heitler mechanism for pair production on the nucleus [26]. Two models, Thomas-Fermi-Moliere [32, 33] and Hartree-Fock [34], for the atomic form factor describing the charge distribution of electrons were considered to account for screening effects due to

---

<sup>1</sup>A. Korchin, Kharkov Institute of Physics and Technology, Kharkov 61108, Ukraine.

atomic electrons. The Coulomb distortion effects have been included according to the work of Bethe and Maximon [35] (contribution to the  $e^+e^-$  cross-section of  $\sim 80\%$ ).

- Pair production on atomic electrons taking into account the excitation of all atomic states and correlation effects due to presence of other electrons and the nucleus (contribution of  $\sim 20\%$ ).
- QED radiative corrections (of order  $\alpha/\pi$  with respect to the dominant contributions): (i) virtual-photon loops and (ii) real-photon process  $\gamma + A \rightarrow e^+ + e^- + A + \gamma'$ , (contribution of  $\sim 1 - 2\%$ ).
- Nuclear incoherent contribution – quasi-elastic, or quasi-free process on the proton  $\gamma + p \rightarrow e^+ + e^- + A + p$  (contribution of  $< 0.05\%$ ).
- Nuclear coherent contribution, *i.e.* virtual Compton Scattering, a two-step process  $\gamma + A \rightarrow \gamma^* + A \rightarrow e^+ + e^- + A$  (contribution of  $\sim 10^{-5}\%$ ).

As an example, Figure 7.1 shows the calculated energy distribution of electrons produced by 5.46 GeV photons on a  $^{12}_6C$  target [31]. The calculations based on three different models of atomic form factors are shown: Hartree-Fock (HF), Thomas-Fermi-Moliere (TFM) and a simpler monopole approximation introduced by Tsai [33]. As one can see in the figure, the cross-section slightly decreases compared to TFM if the HF form factor is used. The difference between the cross-section based on the Hartree-Fock atomic form factor and the one based on the Thomas-Fermi-Moliere model is of the order of  $< 1\%$  which demonstrates consistancy of the calculations.

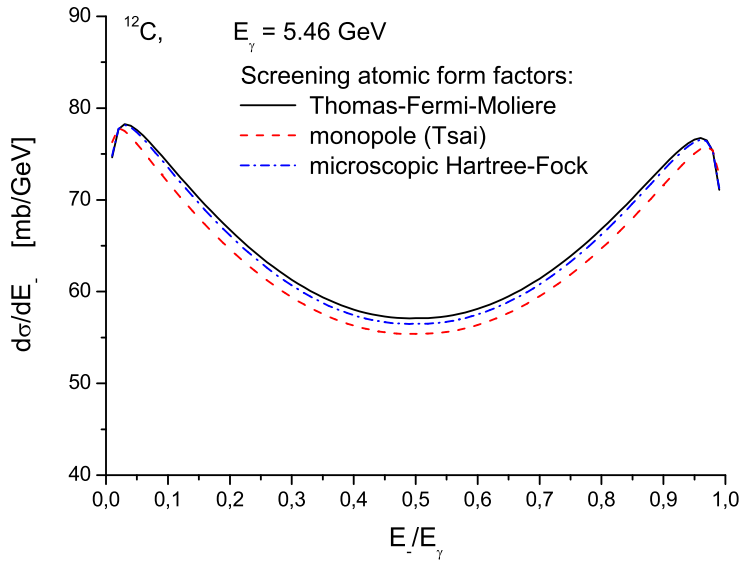


Figure 7.1: Calculated energy spectrum of electrons in pair-production on  $^{12}_{\text{C}}$  for 5.46 GeV photons.

Note that as shown in Figure 7.2 part (a), the total cross-section for  $e^+e^-$  production changes by less than 0.2% for incident photon energies of 4.91 – 5.46 GeV. The fact that the cross-section is nearly constant at photon energies of  $\sim 5$  GeV is also demonstrated in Figure 7.2 part (b) showing the absolute differential cross-section for pair-production as a function of fraction of photon energy carried by the electron. This allows one to combine the data from different photon energies (see Table 7.1) when presenting the data as is done in Figure 7.2 part (b).

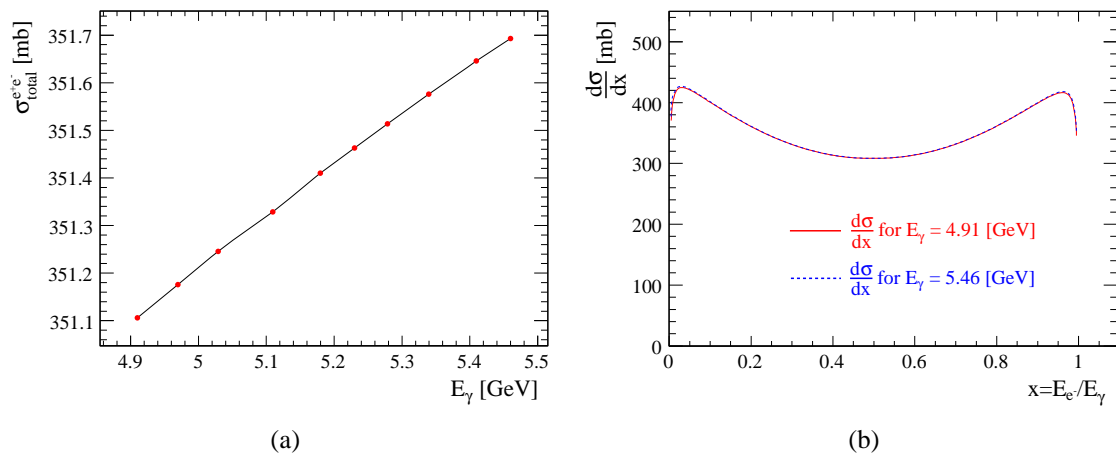


Figure 7.2: (a) Total cross-section for pair-production on  $^{12}\text{C}$  for photons in energy region  $4.91 - 5.46 \text{ GeV}$ . (b) Absolute cross-section for pair-production differential in fraction of energy of photon carried by the electron for  $E_\gamma = 4.91 \text{ GeV}$  and  $E_\gamma = 5.46 \text{ GeV}$ .

### 7.3 Measured quantities and data structure

A schematic of a pair-production event as seen by the PrimEx experimental setup (downstream of the tagger) is shown in Figure 7.3:

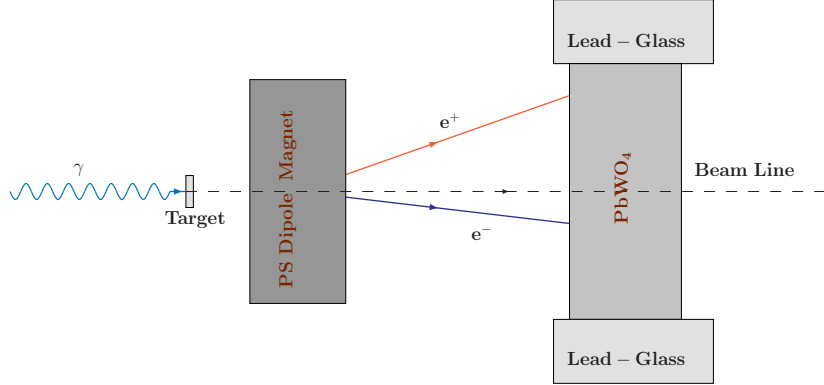


Figure 7.3: Schematic of a pair-production event as seen by the PrimEx experimental setup (top view).

For the pair-production cross-section measurement, both the incident photon energy and timing information were determined by the tagger. The strength of the magnetic field of the PS dipole was lowered (to  $\sim 0.220$  and  $0.293$  T $\times$ m) and the electron-positron pairs were swept into the calorimeter where the energy and position of the each particle was measured. The trigger signal, a coincidence between Tagger MOR and HyCal, recorded in a TDC provides timing information for the  $e^+ e^-$  - pair (see Figure 6.1).

Data accumulated during the PrimEx run are recorded in CODA (CEBAF Online Data Acquisition [29]) format. The data are structured into banks. Each bank has a “header” and a “body”. All banks have identical header structure, containing the name of the bank and the number of rows in the body of the bank. The banks that are used in pair-production

cross-section analysis fall into two separate categories; reference/service banks: TRIGGER, EVENTID and TRIGGER\_PHASE and physics banks: TRIGPHOTON and HYCALCLUSTER. The detailed list of the PrimEx data banks can be found by examining the latest version of “bankdef.xml” file in PrimEx software CVS (Concurrent Versions System) [36], and a description of the information stored in the banks is given in [37]. The reference banks provide the event number, run number and trigger ID that caused the readout of the DAQ electronics<sup>2</sup> and contain one entry per event/trigger. The TRIGPHOTON bank provides the time recorded by T-counter, T-channel ID, E-channel ID and photon energy. The HYCALCLUSTER bank stores the  $x$ ,  $y$ ,  $z$  coordinates and the energy of clusters reconstructed in the calorimeter. And finally the TRIGPHOTON bank also provides the time differences between the hits reconstructed in the Tagger and the trigger signals. The information in the TRIGPHOTON bank is used to identify the photon that was involved in the trigger for current event readout. The multiplicity, *i.e.* the number of rows/entries per event, of physics banks is rate dependent.

#### 7.4 Event selection

The first step in event selection is identifying and removing the beam trip regions from the data, which is done according to the procedure described in Section 6.2 requiring a  $3\sigma$  cut on fractional livetime. Note that the efficiency of this cut has no impact on the cross section of the studied process, since discarded data regions are excluded both from the yield extraction as well as from the flux calculation.

Figure 7.4, part (a) shows the different triggers enabled for the PrimEx  $e^+e^-$ - production

---

<sup>2</sup>Up to twelve triggers, such as clock triggers or physics triggers, can be set up with various prescale factors to control the data acquisition.

data taking. The trigger IDs 1, 5 and 10 correspond to MOR, Clock and physics (HyCal - MOR) triggers, respectively. The events triggered by MOR and Clock are mixed into the data for diagnostics and photon flux calculation purposes. For cross-section extraction one is interested only in events triggered by the HyCal-Tagger coincidence, *i.e.*, events with more than 0.5 GeV deposited in the HyCal and a photon registered in the Tagger. These events can be selected by requiring bit 10 to be set in the trigger latch word of the TRIGGER bank (see Figure 7.4, part (b)).

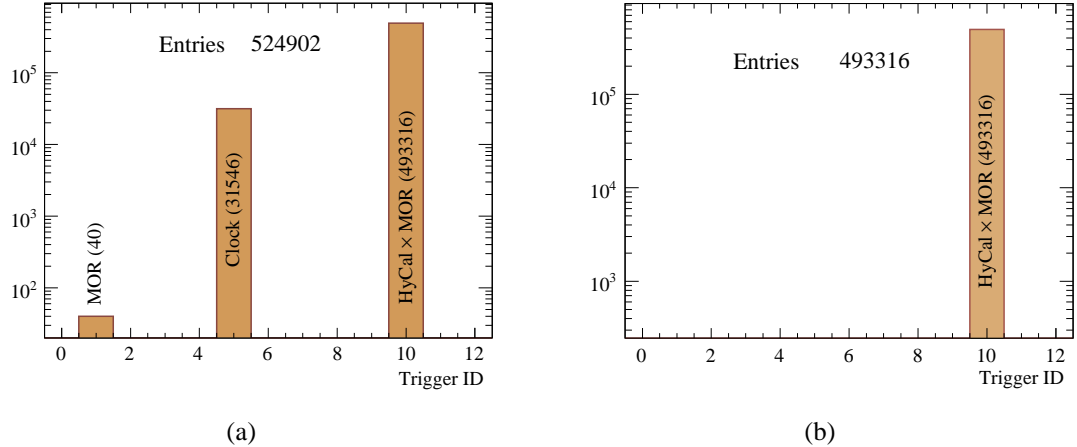


Figure 7.4: (a) The various triggers and their absolute amount in a  $e^+ e^-$  production run #5142 are shown. (b) Only events triggered by HyCal-Tagger coincidence are selected.

Even at electron beam intensities of pair-production runs of  $\sim 1$  nA, which with a  $10^{-4}$  rad. length radiator translates into  $\sim 0.6 \times 10^5$  equivalent photons per second, it is possible to have up to ten photons per event in the tagger (see Figure 7.7, part (a)).

Figure 7.5 shows the TDC spectra for various trigger signals in run #5142. Only three triggers were actually enabled for pair-production runs, but signals from ten possible triggers

were recorded in a TDC.

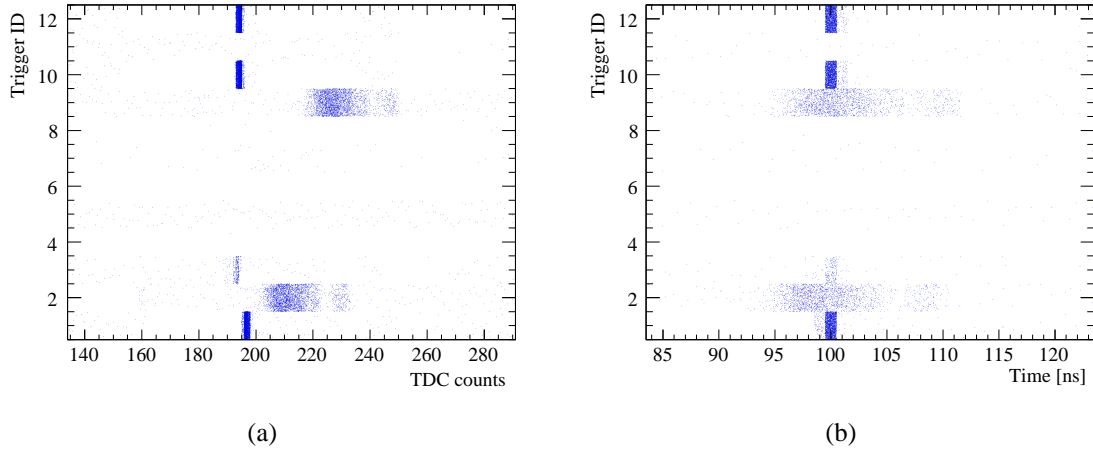


Figure 7.5: (a) TDC spectra for various triggers in pair-production run #5142. (b) Reconstructed and calibrated (with respect to the HyCal-Tagger coincidence) times of various trigger signals.

The TDC windows for the PrimEx electronics were set to  $16 \mu\text{s}$ , while the gate signal for HyCal ADCs was only 250 ns wide. The HyCal-MOR coincidence (trigger ID = 10) happens at  $\sim 200$  TDC counts, opening the ADC gate. Hence only those HyCal hits which happen within a 250 ns window (at/after the trigger) correspond to the values recorded in the HyCal ADCs. By cutting between 180 and 700 TDC counts on the trigger ID = 2, corresponding to HyCal total energy sum signal without tagger coincidence, the HyCal hit times in the proper range are selected. Comparing the times of the photons reconstructed in the tagger with HyCal hit times, that are in time with trigger, the photons which have the potential to be responsible for the energy deposited in HyCal are selected and stored in TRIGPHOTON bank. A rather wide timing cut ( $\pm 15$  ns), on tagger-trigger time differences, is used at this stage of event selection (see Figure 7.6).

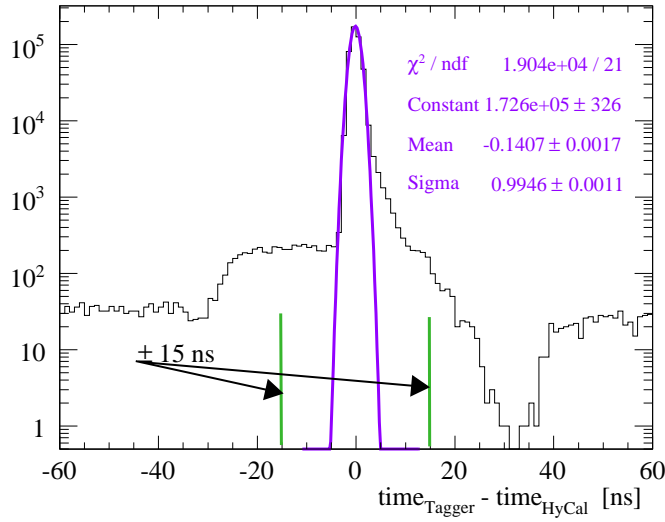


Figure 7.6: The time difference between HyCal total sum signal and events reconstructed in the tagger. The  $\pm 15\text{ns}$  coincidence window is also shown.

The above described procedure greatly reduces the tagger photon multiplicity. As seen in Figure 7.7, part (b) only  $\sim 0.9\%$  of the events have ambiguity in photon selection, *i.e.*, the possibility of misidentification of the incident photon energy.

Examining the multi-photon events, one can see that the majority of these events (87% out of 4064) are accidentals within the same T-channel, *i.e.*, have exactly the same time. The energy difference for photons in such multi-photon events is on the order of  $22 - 30$  MeV (see Figure 7.8 part (a)), which is well within the resolution of HyCal. For the 13% of the multi-photon events these are accidentals between different T-channels, *i.e.*, have different times, and the “true” photon can be selected by picking the one that is closest to the trigger time. However, as seen in Figure 7.8 part (b), in this case the true and accidental photons can have energy difference of up to 0.5 GeV, which will “misplace” the yield when calculating differential cross-section  $d\sigma/dx$  (where  $x = E_{e^\pm}/E_\gamma$ ) if one picks the “wrong” photon. To

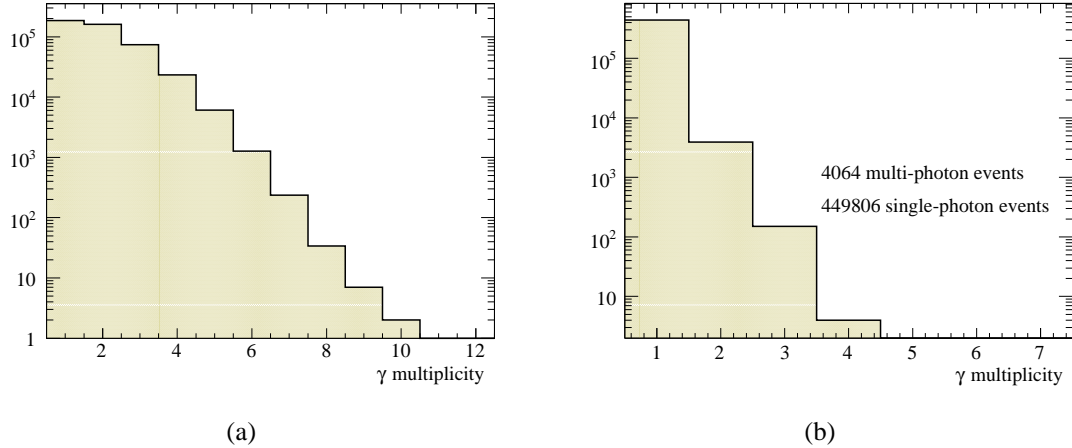


Figure 7.7: (a) The number of photons reconstructed in the Tagger per event. (b) The number of photons reconstructed in the Tagger per event that have the potential to be involved in the trigger.

quantify the effect of 0.9% of multi-photon events the cross-section extraction is performed with and without multi-photon events<sup>3</sup>.

All the particles reaching the HyCal are assigned a charge based on their  $X$  coordinate. The Pair Spectrometer dipole for  $e^+e^-$  runs operated at positive currents. Positive current corresponds to positive polarity of the magnet which gives a magnetic field pointing upward along the vertical  $Y$  axis. The upward magnetic field will deflect positively charged particles beam right ( $X < 0$ ) and the negatively charged particles will be deflected to the beam left ( $X > 0$ ).

The selected events are stored in a *ROOT* tree, recording the cluster energy (“*cl\_e*”), the cluster position at the HyCal (“*cl\_x*”, “*cl\_y*” and “*cl\_z*”), the cluster charge (“*cl\_charge*”), the T-channel ID (“*T\_id*”), the E-channel ID (“*E\_id*”), the incident photon energy (“*e0*”), the

---

<sup>3</sup>Note that the photon flux needs to be recalculated when evaluating cross-section with single-photon events only.

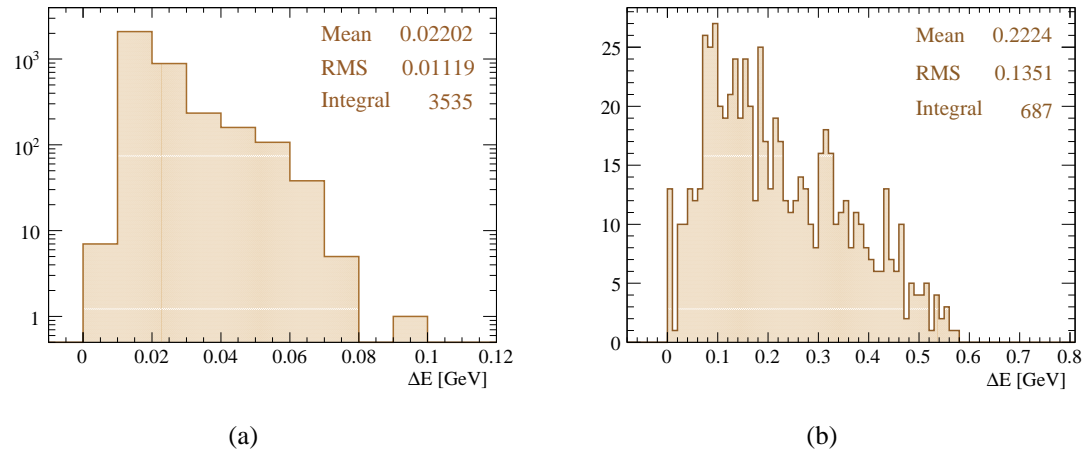


Figure 7.8: (a) The energy difference for photons reconstructed in the Tagger with an accidental in the same T-channel. (b) The energy difference for photons reconstructed in the Tagger with accidental in different T-channel.

incident photon time (“ $T\_time$ ”), the time difference between the incident photon and the HyCal total sum signal (“ $tdiff$ ”) and the event number (“ $event\_number$ ”).

## 7.5 Simulation

A fast, two-step *GEANT4* simulation was developed to aid in the study of the effects of Compton background, fiducial cuts and the target. It should be noted that the simulation is not intended to reproduce the response of the calorimeter or any other physical detector. The *GEANT4* pair-production and Compton scattering cross-sections provide accuracy of  $\sim 5\text{--}6\%$  [38]. Since at  $5\text{--}6$  GeV the total absolute cross-section for Compton scattering is  $\sim 0.5\%$  of the  $e^+e^-$ -production total cross-section, the simulation is a valuable tool for quantitative study of the main source of physics background – Compton scattering. Also the simulation is used to study the energy losses of  $e^+e^-$ -pairs passing through a  $\sim 1$  cm thick carbon target and the few meters long helium-filled gap between the dipole exit window and the face of the calorimeter.

Figure 7.9 shows the setup used in the simulation and a few simulated  $e^+e^-$  tracks. It consists of a  $13.212 \times 13.212 \times 13.212$  m $^3$  cube–”World” volume made of vacuum (*i.e.*, air with density of  $10^{-25}$  g/cm $^3$ , and pressure  $3 \cdot 10^{-18}$  Pa). The World volume contains a  $2.898 \times 2.898 \times 0.966$  cm $^3$  carbon target (with density 2.198 g/cm $^3$ ), an inner chamber of size  $11 \times 11 \times 11$  m $^3$  made of helium (at pressure of 1.013 Pa and density of 0.1787 mg/cm $^3$ ) to reproduce the effect of the helium bag in the experiment. The inner chamber contains a  $1.126 \times 1.126 \times 1.126$  m $^3$  cube made of vacuum and containing a homogeneous magnetic field directed vertically upwards. The inner chamber also contains a  $1.19 \times 1.19 \times 1.19$  m $^3$  cube made of vacuum and serves as a position holder for the calorimeter. The target is placed right at the edge of the inner chamber so their surfaces touch. The center of the magnet is positioned 0.963 m from the edge of the target downstream along the beamline and the center of “HyCal” is located

7.92 m from the edge of the target downstream along the beamline.

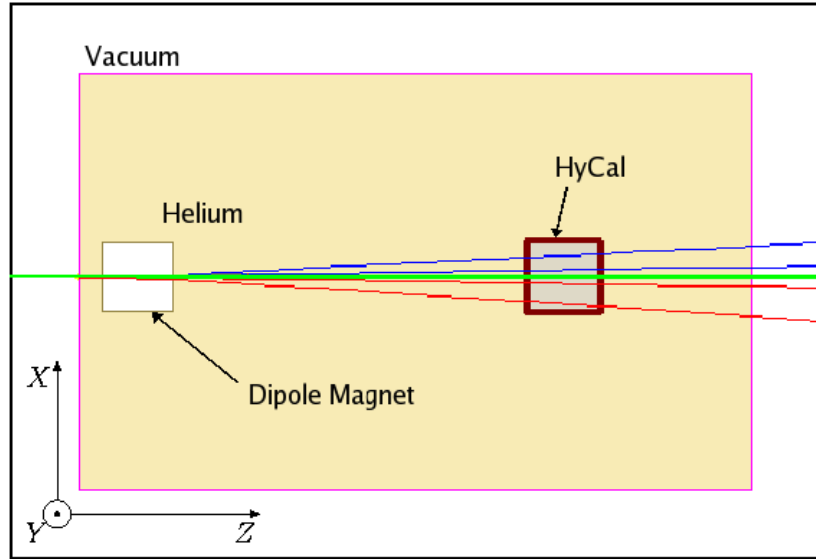


Figure 7.9: A visualisation of *GEANT4* model of PrimEx experimental setup. Pair-production events are also shown (top view).

The primary particle in the first stage of the simulation is a photon. The direction of the primary photons coincides with that of the  $Z$ -axis. The energy of the incident photons in the simulation is picked from the spectrum of the true photons (see Figure 7.20) selected in the data according to the procedure described in Section 7.4. A standard *GEANT4* physics list for electromagnetic processes was used [39]. For the primary photons it allows for photoeffect, Compton scattering and  $e^+e^-$ -production. In total  $2 \times 10^6$  photons were “thrown”. The coordinates and the energies of particles originating in reactions of pair production and Compton scattering were recorded at the surface of the “calorimeter” as well as in the target where the conversion or the Compton event occurred. The distribution of  $X$  and  $Y$  coordinates and energy - coordinate correlation for the generated events are shown in Figure 7.10 parts (a) and

(b) respectively. A  $4.15 \times 4.15 \text{ cm}^2$  central region at the face of the “calorimeter” was excluded from consideration to mimic the central opening of HyCal.

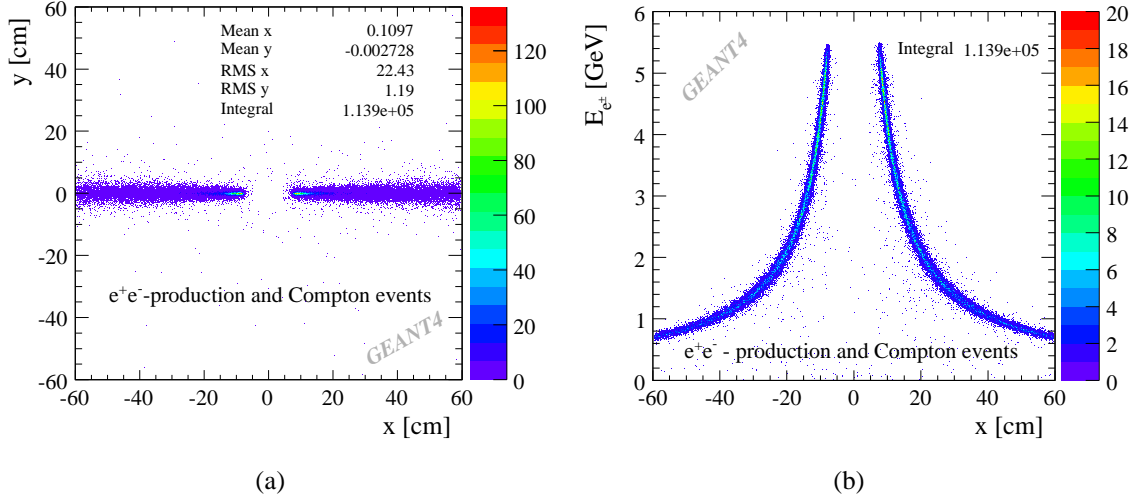


Figure 7.10: (a) The distribution of  $X$  and  $Y$  coordinates and (b) the energy- $X$  position correlation for generated pair-production and Compton scattering events.

To demonstrate the ability of the simulation to describe the data, particles with energies between 4.9 GeV and 5.1 GeV on both electron ( $X > 0$ ) and positron ( $X < 0$ ) arms of the generated events were selected and their deflection in the magnetic field was compared to that of the data (see Figures 7.11 and 7.12).

Figures 7.11 and 7.12 show overall reasonable agreement between simulation and data. The observed differences in the widths can be attributed to the fact that the simulation uses a point like beam where in reality the beam has dimensions. Also the data at this stage of the analysis are contaminated by background from the beam halo which will be discussed in more detail in Section 7.6.

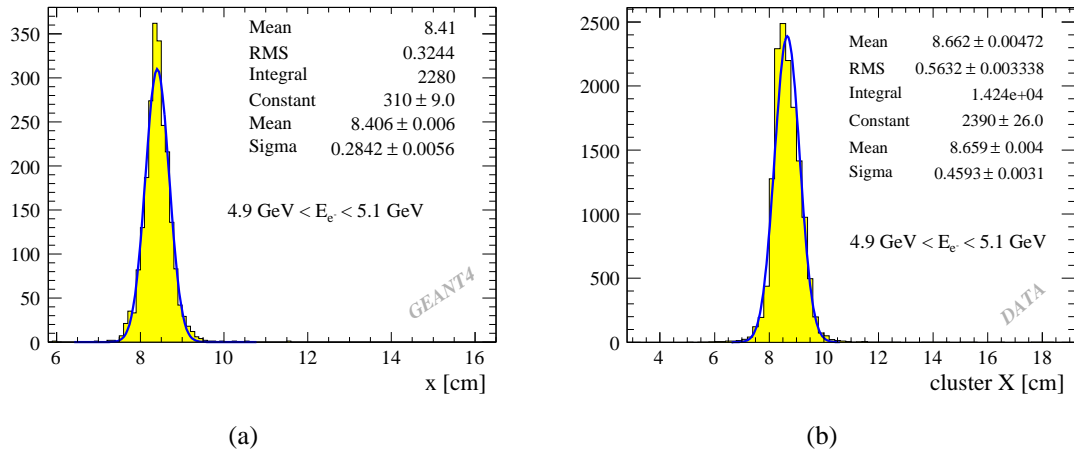


Figure 7.11: The distribution of  $X$  coordinates for electrons with energies between 4.9 and 5.1 GeV (a) generated events and (b) data.

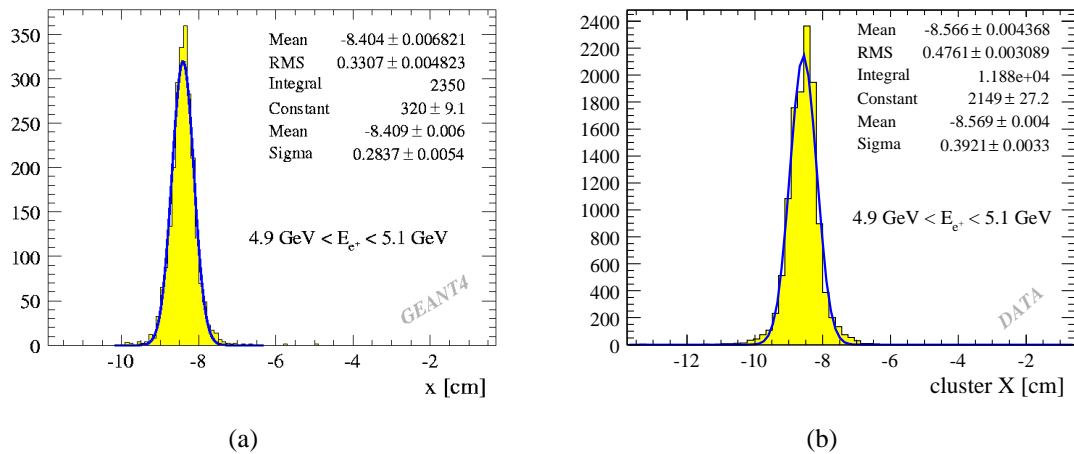


Figure 7.12: The distribution of  $X$  coordinates for positrons with energies between 4.9 and 5.1 GeV (a) generated events and (b) data.

### 7.5.1 Compton Background

Figure 7.13, part (a) shows nearly identical distributions of  $X$  and  $Y$  coordinates for electrons and positrons in the generated events when viewed independent of the position and the energy

of the other particle in the pair<sup>4</sup>. The 2D-distribution of  $X$  and  $Y$  coordinates for particles in the generated Compton events, in the single arm mode, is shown in Figure 7.13, part (b).

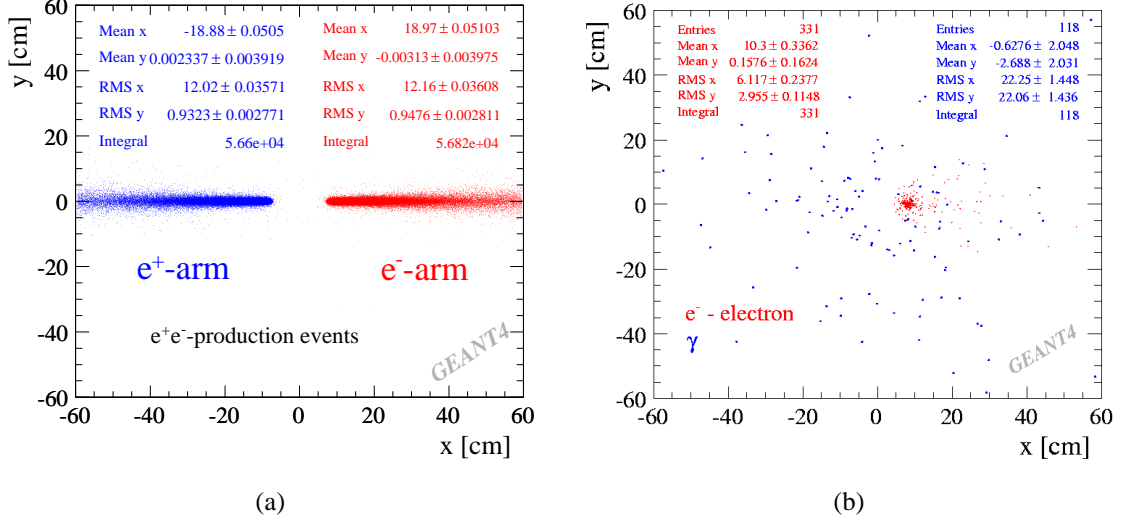


Figure 7.13: The distribution of  $X$  and  $Y$  coordinates for generated events in single arm regime: (a)  $e^+e^-$ -production and (b) Compton events.

It is known that, at energies of incident photon of  $\sim 5$  GeV, the electron in a Compton scattering event most of the time is more energetic than the scattered photon. Given the narrow band of the photon energies used by the PrimEx experiment ( $\sim 4.9 - 5.5$  GeV) we have a narrow band of energies of Compton electrons (see Figure 7.14, part (a)). This means that Compton electrons are distributed in a tight cone around the direction of primary photon and are deflected to a very localized region on the surface of the calorimeter. This can create significant ( $\sim 3 - 4\%$ ) background at the high energy region of the electron spectrum (see

<sup>4</sup>The regime where the energy and position of a particle are considered independent of the parameters of the other particle in the pair will be referred to as single arm, *i.e.*, single arm pair-production or single arm Compton scattering.

Figure 7.15, part (a)) even though the cross-section for the Compton scattering is two orders of magnitude smaller than that of the pair production. The effect is much smaller ( $\sim 0.5 - 0.6\%$ ) if one considers the distribution of electron coordinates on the surface of the calorimeter (see Figure 7.15, part (b)).

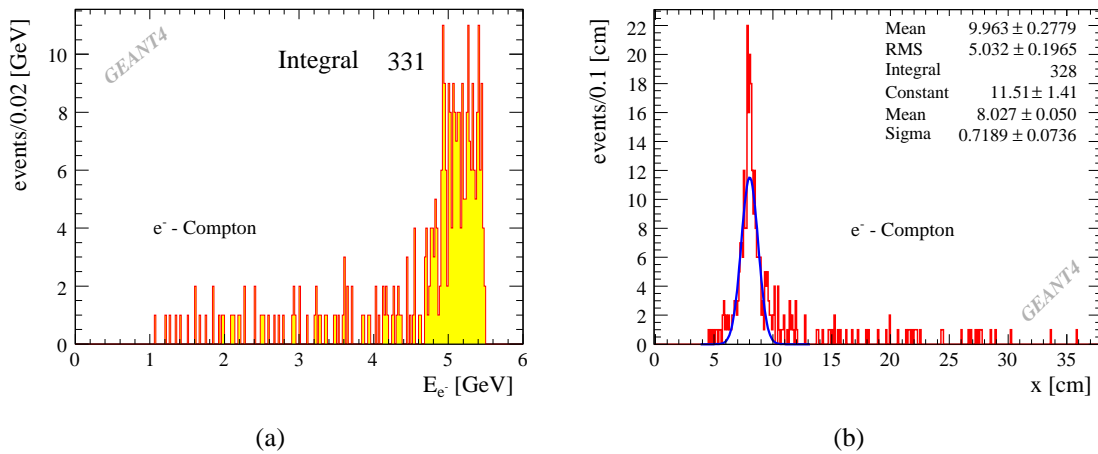


Figure 7.14: (a) Energy spectrum of the Compton electrons at PrimEx kinematics. (b) Distribution of  $X$ -coordinates of Compton electrons at PrimEx kinematics and PS dipole field of  $0.22 \text{ T} \times \text{m}$ .

Figure 7.16 shows the distribution of the  $Z$  position of photon conversion vertices with respect to the center of the target. As one would expect the photon has an equal probability to convert at any point in the target.

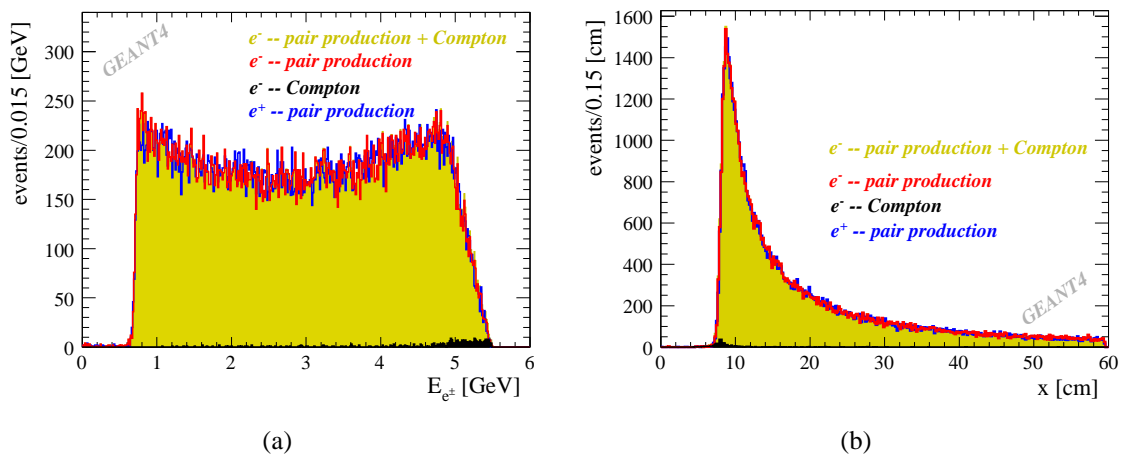


Figure 7.15: (a) Energy spectrum and (b) distribution of  $X$ -coordinates of generated Compton electrons and  $e^+e^-$  pairs.

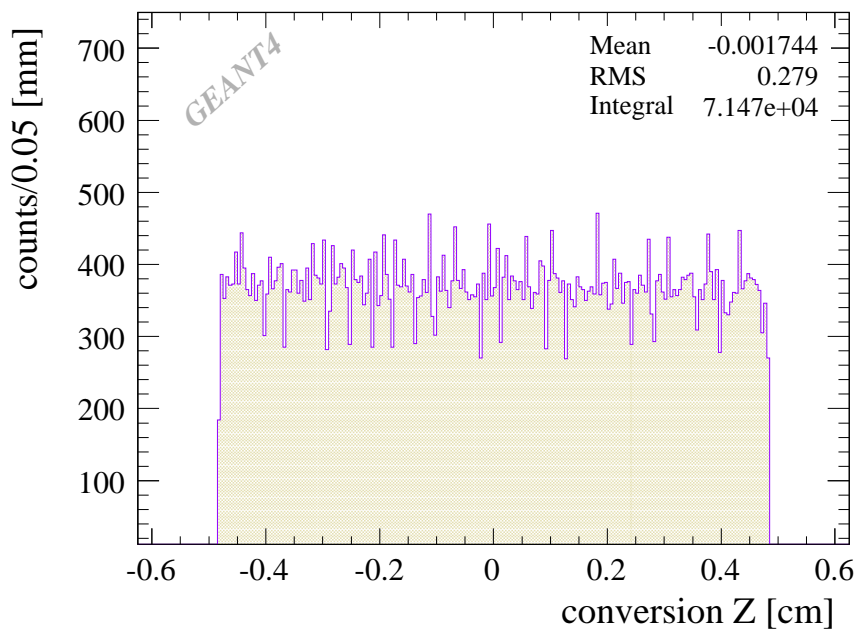


Figure 7.16: A sample distribution of  $Z$ -coordinates of simulated pair-production vertices with respect to the center of the target.

### 7.5.2 Fiducial cuts

Figure 7.17 shows the distribution of  $Y$  coordinates for electrons and positrons in simulated  $e^+e^-$ -events (see parts (a) and (b) respectively). As indicated on the plots a  $|Y| < 5$  cm cut would cost one  $0.25 - 0.29\%$  of the total yield.

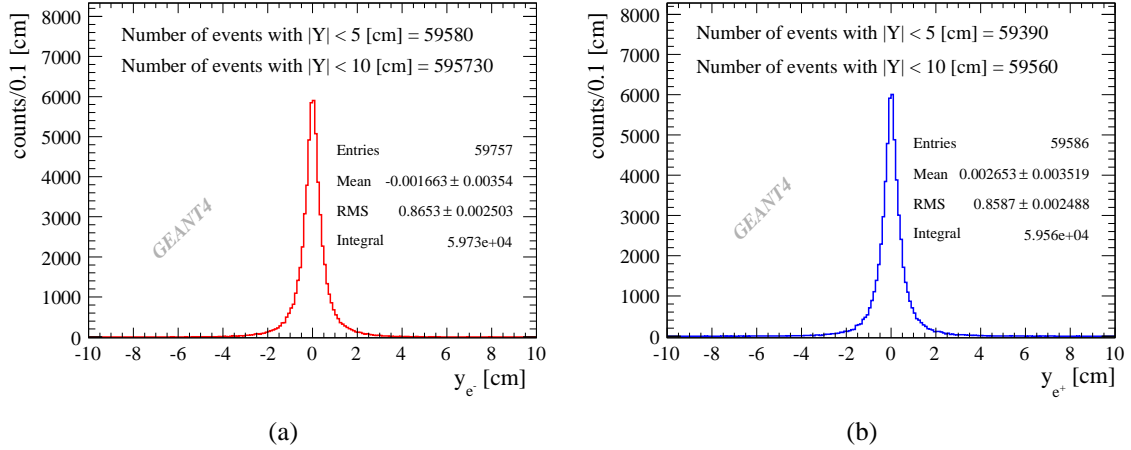


Figure 7.17: Distribution of  $Y$  coordinates of (a) electrons and (b) positrons from generated  $e^+e^-$ -pairs.

Figure 7.18 (parts (a) and (b)) shows that a  $|Y| < 5$  cm cut affects only the electrons and positrons with energies less than  $\sim 1.6 - 1.7$  GeV.

The *GEANT4* simulation demonstrates that the Compton scattering events are confined to a finite momentum region and as the main source of the physical background can be effectively eliminated by restricting the study to an energy band  $E_{min} < E_{e^\pm} < E_{max}$  (the numerical values of  $E_{min}$  and  $E_{max}$  will be discussed in Section 7.6). This enables the study of the pair production in a single arm regime having the opportunity to measure the same cross-section simultaneously in an independent manner via both the electron and positron arms.

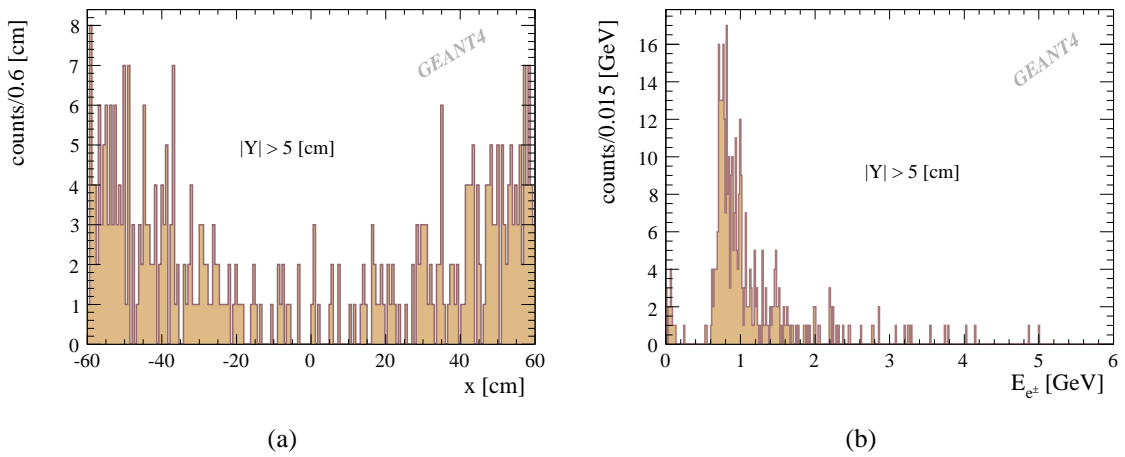


Figure 7.18: (a) Distribution of  $X$  coordinates for electrons and positrons with  $|Y| > 5 \text{ cm}$ . (b) Energy spectrum of electrons and positrons from generated  $e^+e^-$ -events where of  $|Y| > 5 \text{ cm}$ .

### 7.5.3 Energy losses in target and helium

According to the *GEANT4* implementation of the energy losses [38], in the simulation the electrons and positrons, with energies of a few GeV, have nearly identical energy losses in the target and helium due to the ionization, multiple scattering and bremsstrahlung which is shown on Figure 7.19 part (a). The difference of energy losses in a material for positrons and electrons arises from differences in cross-sections for Möller and Bhabha scattering and is more pronounced for electrons/positrons in a few MeV energy range. Figure 7.19 part (b) shows the correlation between the  $Z$  position of the vertex, with respect to the center of the target, and the energy losses of the electrons. Simulation shows that energy losses due to ionization and secondary interactions are significant and need to be taken into account when comparing the experimental cross-sections with theoretical calculations.

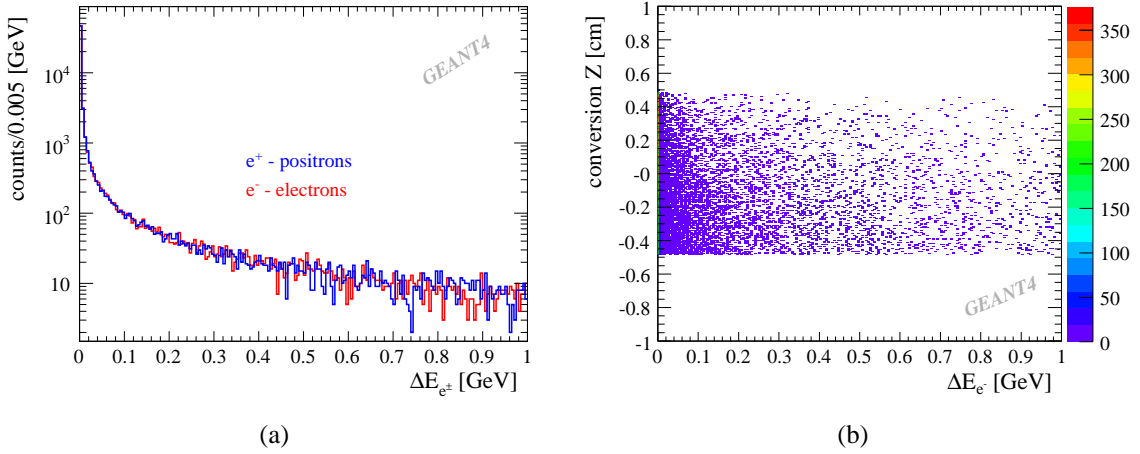


Figure 7.19: (a) Energy losses of generated electron and positron pairs in the target and helium bag. (b) The correlation of energy losses and the  $Z$  position of the conversion point in the target.

## 7.6 Yield Extraction

Following the event selection recipe introduced in Section 7.4 one can obtain the spectrum of selected photons which is shown in Figure 7.20.

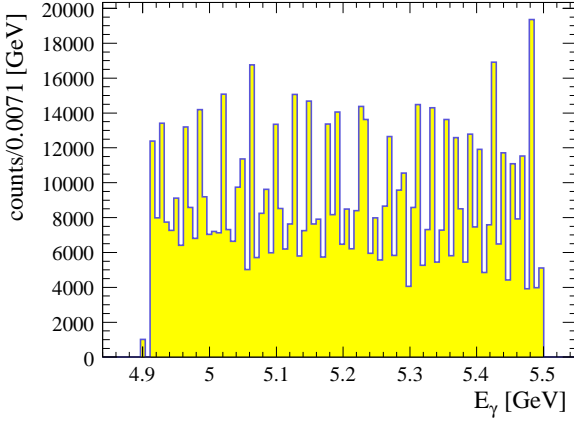


Figure 7.20: Energy spectrum of incident photons showing almost uniform distribution of  $\gamma$ 's over the tagged energy range (4.874 – 5.494 GeV).

The even E-channels are the product of the overlapping nature of the physical E-counters and have smaller width compared to odd E-channels which results in an uneven population of various E-channels. The level of occupancy of an E-channel also depends on its geometrical correspondence to odd or even T-channel.

The energy range represented in Figure 7.20 corresponds to 114 E-channels. The E-channels are combined in groups of 11 or 12 channels to comprise 10 energy sub-ranges providing finer photon energy binning. The boundaries of these 10 energy ranges are determined by the average energy of the first and last E-channel in the respective sub-range. The details of the fine photon energy bins are listed in Table 7.1:

Table 7.1: Table of photon energy bins.

Bin ID	min. E-ID	max. E-ID	$E_\gamma$ min. (GeV)	$E_\gamma$ max. (GeV)	$E_\gamma$ avg. (GeV)
1	104	114	4.898	4.956	4.927
2	93	103	4.962	5.018	4.990
3	82	92	5.023	5.074	5.049
4	71	81	5.085	5.141	5.113
5	60	70	5.145	5.201	5.173
6	49	59	5.207	5.260	5.234
7	37	48	5.267	5.326	5.296
8	25	36	5.332	5.388	5.360
9	13	24	5.393	5.443	5.418
10	1	12	5.450	5.494	5.472

The  $\pm 15$  ns timing cut introduced in Section 7.4 for event selection can be further refined by examining the Tagger-HyCal time differences, *i.e.*, “tdiff” spectra, for individual T-channels (see Figure 7.21).

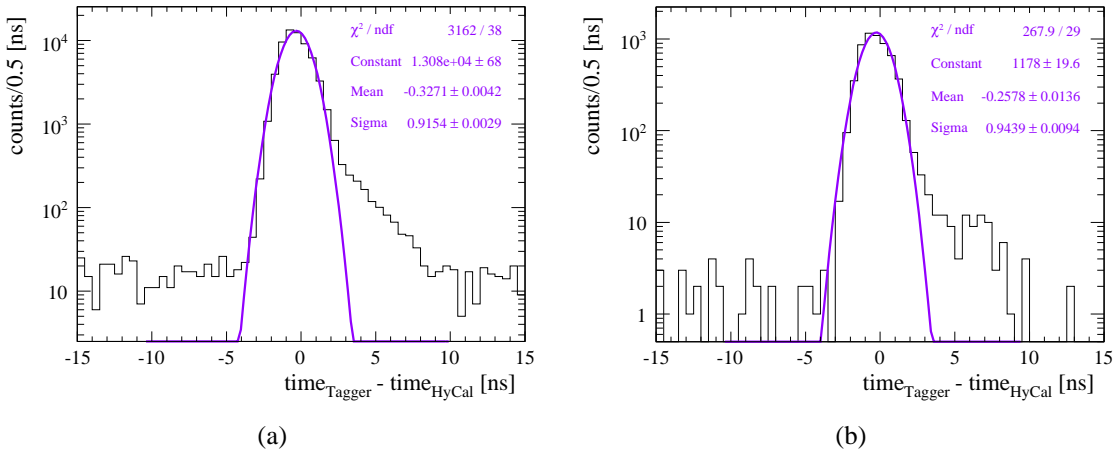


Figure 7.21: Tagger-HyCal time difference spectra for: (a) T-channel #3 and (b) for T-channel #12.

In parts (a) and (b) of Figure 7.21 showing the “tdiff” spectra for T-channels #3 and

#12 respectively, one can see that the mean values are different for the spectra of different T-channels. Figure 7.21 also shows a tail trailing on the positive side of the spectrum. A conservative, asymmetric cut  $(-5\sigma, +8\sigma)$  about the mean value has been applied to the “tdiff” distribution of each T-channel to account for these effects. The mean values and the standard deviations for various T-channels are listed in Table 7.2:

Table 7.2: List of mean values and standard deviations of “tdiff” distributions for various T-channels.

T-channel ID	mean (ns)	$\sigma$ (ns)
1	-0.3	0.9
2	-0.4	0.9
3	-0.3	0.9
4	-0.7	0.9
5	-0.5	0.9
6	-0.6	0.9
7	-0.1	0.9
8	-0.2	0.9
9	-0.2	0.9
10	-0.4	0.9
11	0.0	0.9
12	-0.3	0.9
13	-0.1	0.9
14	-0.6	0.9
15	-0.3	0.9
16	-0.3	0.9
17	0.0	0.9
18	-0.1	0.9
19	0.0	0.9
20	-0.1	0.9
21	0.0	1.0

As an example, Figure 7.22 shows the distribution of  $X$  and  $Y$  coordinates and the energy position correlation for events with incident photon energy in the range  $5.145 - 5.201$  GeV, *i.e.*, energy bin 5 after the timing cut of  $(-5\sigma, +8\sigma)$ . The negative  $X$  coordinates correspond to positrons and the positive  $X$  coordinates represent electrons<sup>5</sup>.

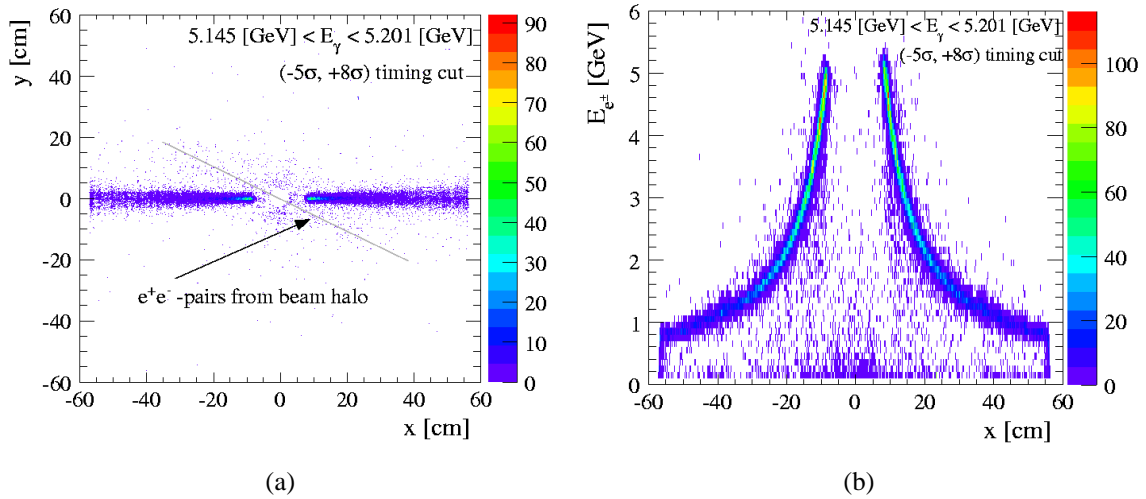


Figure 7.22: (a) Distribution of  $X$  and  $Y$  coordinates of clusters reconstructed in HyCal. (b) Correlation of energy and deflection in the magnetic field for clusters reconstructed in HyCal.

In part (a) of Figure 7.22, one can see a ring of “Compton” photons around the central opening of the HyCal and a faint line with negative slope due to pair-production generated by the halo of the beam hitting the photon beam collimator upstream of the experimental target. The electrons and positrons created by the halo on the collimator are first deflected in the field of the permanent magnet in the vertical direction and then by the Pair Spectrometer dipole

---

<sup>5</sup>All the plots pertaining to the analysis of pair production data, simulated or experimental, assume single arm analysis mode, *i.e.*, no energy conservation condition is being used.

magnet in the horizontal direction creating the sloped line.

To eliminate the  $e^+e^-$ -pairs created by the beam halo and most of the Compton photons, a cut on the  $Y$  coordinate of the particles is used. The distributions of  $Y$  coordinates for positrons and/or electrons, shown in Figure 7.23, created by incident photons of energy  $E_{\gamma \text{ bin}1} = 4.90 - 4.96 \text{ GeV}$  and  $E_{\gamma \text{ bin}10} = 5.45 - 5.49 \text{ GeV}$  have nearly identical widths which allows for a single cut range ( $|Y| < 5 \text{ cm}$ ) for all the energies of the photons. As shown by the simulation (see Figure 7.18) such a cut would affect electrons/positrons created on the target if their energy is less than  $\sim 1.6 - 1.7 \text{ GeV}$ .

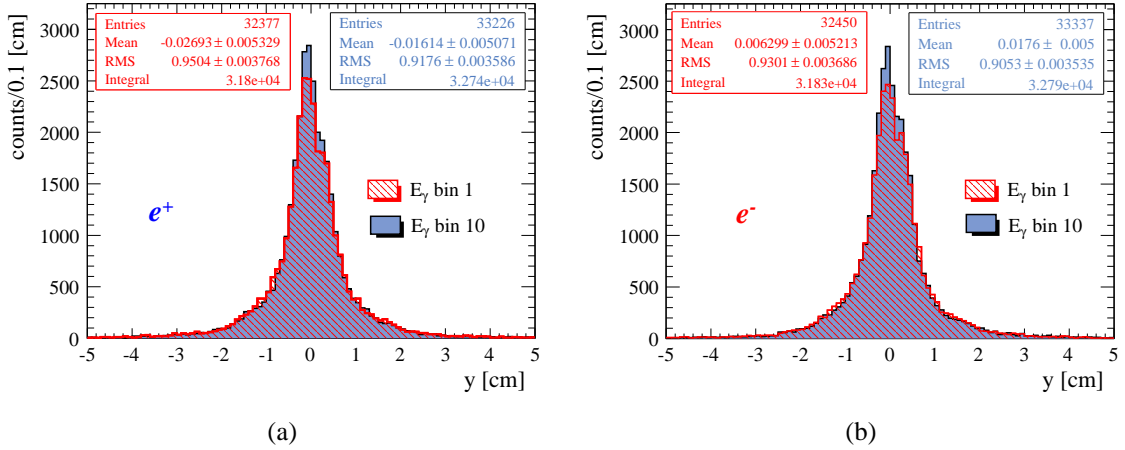


Figure 7.23: Distribution of  $Y$  coordinates of clusters reconstructed in HyCal due to incident photons of various energy: (a) positrons and (b) electrons.

As mentioned previously, pair-production data were taken with various settings of the Pair Spectrometer dipole (see Section 7.3). For the highest field setting of  $\sim 0.293 \text{ T} \times \text{m}$ , momenta of 1.6 GeV and less correspond to deflections of particles in the field of the dipole of  $\sim 37.17 \text{ cm}$  or more, *i.e.*, deflections into the outer Lead-Glass layer of the calorimeter. A cut of  $E_{e^{\pm}} >$

1.695 GeV on the energy of leptons limits the analysis to the inner, high resolution, lead-tungstate layer of the HyCal which extends out to  $\pm 35.275$  cm and enables the comparison of the data from runs with different field settings. Table G.1 lists the pair-production data runs with the setting of the Pair Spectrometer dipole for each run, the minimum lepton energy cut, and the corresponding minimum deflection in the horizontal direction.

As shown in part (a) of Figure 7.14, Compton electrons take most of the energy in the kinematic regime of the PrimEx experiment. Thus a cut  $E_{e^\pm} > 1.2$  GeV would also eliminate a large amount ( $\sim 59.9\%$ ) of Compton photons, some of which would otherwise be reconstructed in the lead-tungstate part of the calorimeter (see Figure 7.24). It is worth noting that the distributions of  $X$  and  $Y$  coordinates for Compton photons are identical due to the azimuthal symmetry of Compton scattering.

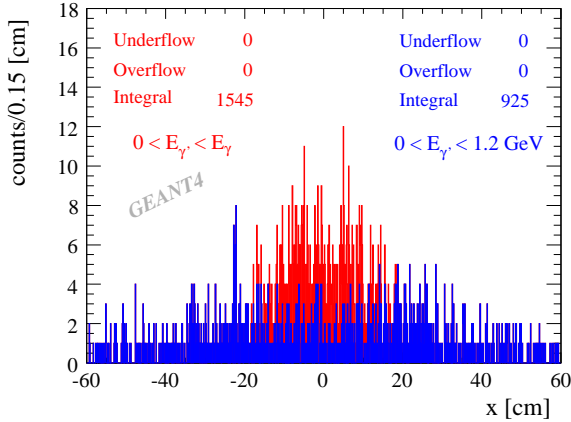


Figure 7.24: Distribution of  $X$  coordinates of scattered photons in simulated Compton events.

The final step toward the yield extraction is the subtraction of the background due to Compton scattering under the electron arm. For this purpose the energy distribution of Compton

electrons was generated for each photon energy bin as described in Section 7.5 (see Figure 7.14) and smeared with the detector resolution function (see Figure 2.12). The resulting distribution, shown in Figure 7.25, is subtracted from data with an appropriate scaling factor. The scaling factors, listed in Table 7.3, were determined according to the photon flux in each run keeping in mind that in total  $2.5 \times 10^7$  photons were thrown to generate the Compton electron background. The photon flux for the pair-production runs is listed in Appendix G.

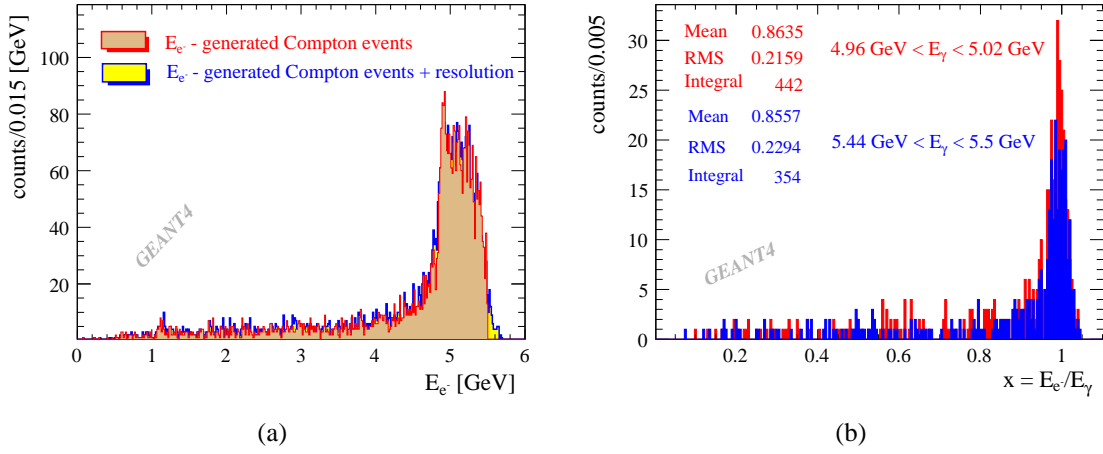


Figure 7.25: (a) Energy spectra of the Compton electrons generated in a **GEANT4** simulation by incident photons in the energy range (4.874 – 5.494 GeV). The effect of detector resolution is shown by the blue histogram. (b) Energy distribution of Compton electrons for incident photon energy bins 2 and 10.

An example of the high energy part of the electron spectrum, which is most affected by the background, is shown in Figure 7.26 before and after subtraction of Compton background.

Table 7.3: Compton electron background scaling factor based on total photon flux in the run.

Run Number	scaling factor	error (%)
5142	0.47919	0.34
5314	0.34516	0.40
5141	0.34381	0.40

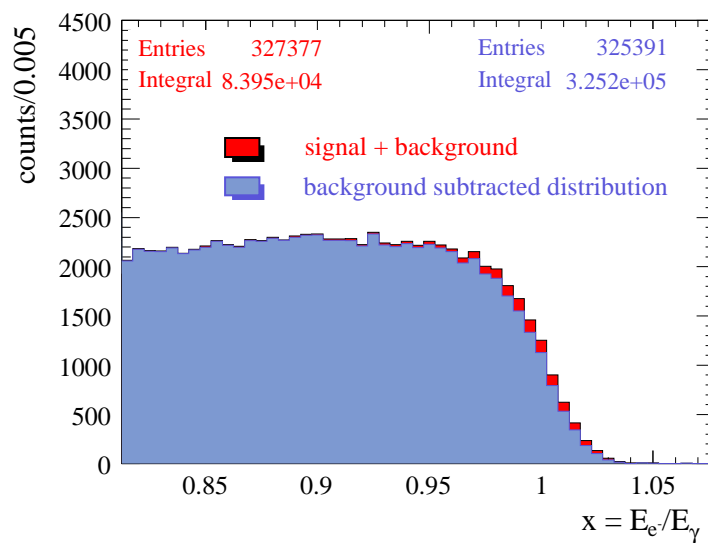


Figure 7.26: Energy spectrum of electrons before and after subtraction of Compton background.

## 7.7 Cross-Section

As mentioned in Section 2.3, the number of atoms per unit area in the carbon target is:  $0.1066 \times 10^{24} \left[ \frac{1}{cm^2} \right]$  ( $\pm 0.053\%$ ). Knowing the photon flux, one can easily convert yields, obtained as described in Section 7.6, into cross-sections. But before the cross-section obtained in the experiment can be compared to the one calculated by theory, one needs to take into account the effects of HyCal resolution and the energy losses of electrons and positrons due to secondary interactions in the target and the helium before they reach the calorimeter (see Figure 7.27)<sup>6</sup>. To do so *GEANT4* has been utilized.

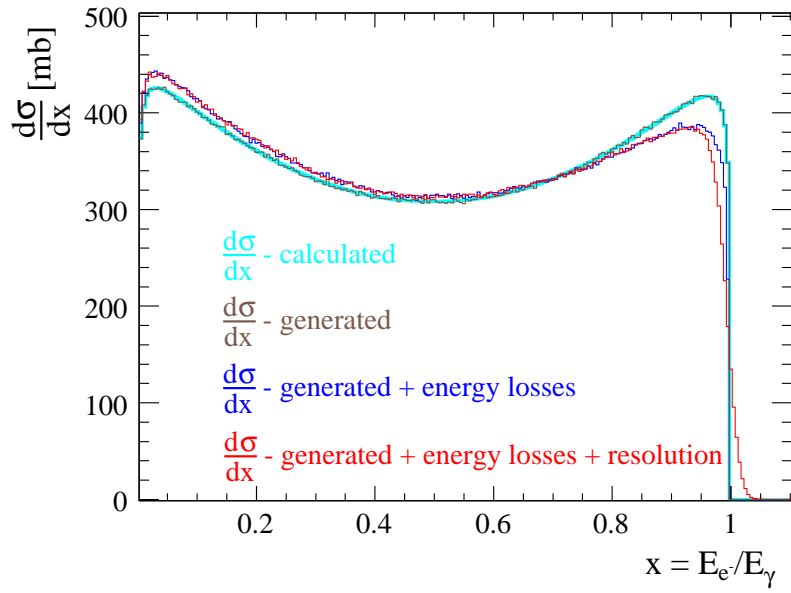


Figure 7.27: Absolute cross-section for pair-production differential in fraction of energy of photon carried by the electron for  $E_\gamma = 4.91 - 5.46$  GeV. The effect of energy losses in target and the helium bag is also shown as a blue histogram.

---

<sup>6</sup>The electron arm was used to generate the plot. Using the positron arm results in an identical distribution since the theoretical cross-sections for electrons and positrons are the same [31].

First a photon energy is picked according to the spectrum of photons present in the data (see Figure 7.20). Then an electron/positron is generated with a fraction of photon energy according to the spectrum shown in Figure 7.2 part (b) and at position  $(0., 0., Z)$  where the  $Z$ -coordinate is picked based on the distribution of  $Z$ -positions of vertices of  $e^+e^-$  events generated in the first stage of the simulation (see Figure 7.16). In total 10-million such events were generated and the electrons/positrons were tracked through the *GEANT4* setup introduced in Section 7.5. The energies of the particles at the surface of the calorimeter were then recorded. The energies of the electrons/positrons, recorded in the simulation at the surface of the calorimeter, were smeared according to the resolution function of the calorimeter shown in Figure 2.12. The generated yields were normalized to obtain a differential cross-section according to the calculated total cross-section for  $E_\gamma = 5.18$  GeV (see Table 7.4).

Table 7.4: Total cross-section for pair-production calculated for the central values of the 10 energy bins.

Energy bin ID	$E_\gamma$ avg. (GeV)	$\sigma_{total}^{e^+e^-}$ (mb)
1	4.91	351.106
2	4.97	351.176
3	5.03	351.244
4	5.11	351.328
5	5.18	351.408
6	5.23	351.461
7	5.28	351.513
8	5.34	351.574
9	5.41	351.644
10	5.46	351.692

For electrons *GEANT4* allows for multiple scattering, ionization and bremsstrahlung providing cross-section accuracy for these processes of  $\sim 5 - 10\%$  [38]. Let us define  $\sigma_0 = \frac{d\sigma_0}{dx}$

to be the calculated cross-section for pair production and  $\sigma_1 = \frac{d\sigma_1}{dx}$  to be the differential cross-section convoluted with the energy losses and the detector resolution. Then  $r = 100 \frac{\sigma_0 - \sigma_1}{\sigma_0}$  will be the percent deviation of the differential cross-section convoluted with the energy losses and detector resolution from the calculated value. In Figure 7.28  $r$  is plotted as a function of the fraction of energy of the incident photon carried by the electrons/positrons.

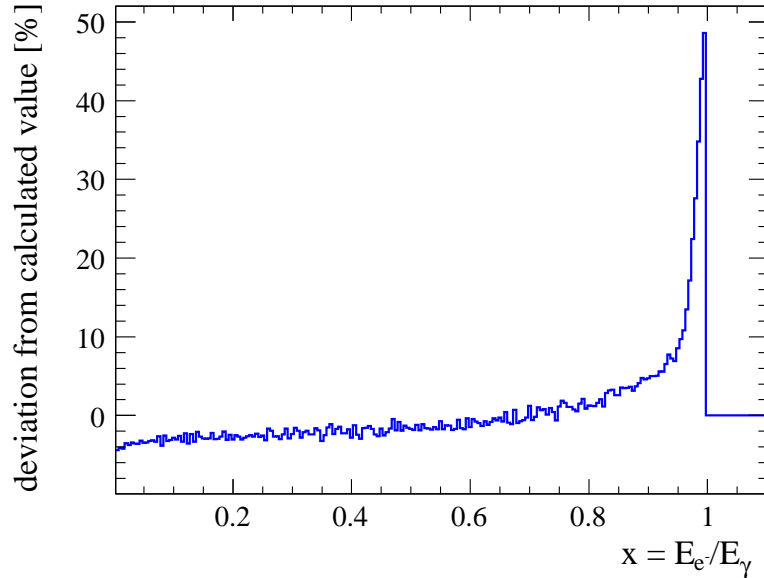


Figure 7.28: Percent deviation of the differential cross-section convoluted with energy losses and detector resolution from the calculated value.

One can see that for electrons or positrons with energy fraction  $0.9 < x < 1.0$ , the percent difference between calculated cross-section and the one modified by energy losses and detector resolution is changing rapidly ( $5\% < r < 50\%$ ). Hence, for this region of  $x$  one could expect up to  $2 - 5\%$  discrepancy between experimental cross-sections and theory (modified by energy losses and resolution) due to the uncertainty of the *GEANT4* calculation of the energy

losses (see Figure 7.29).

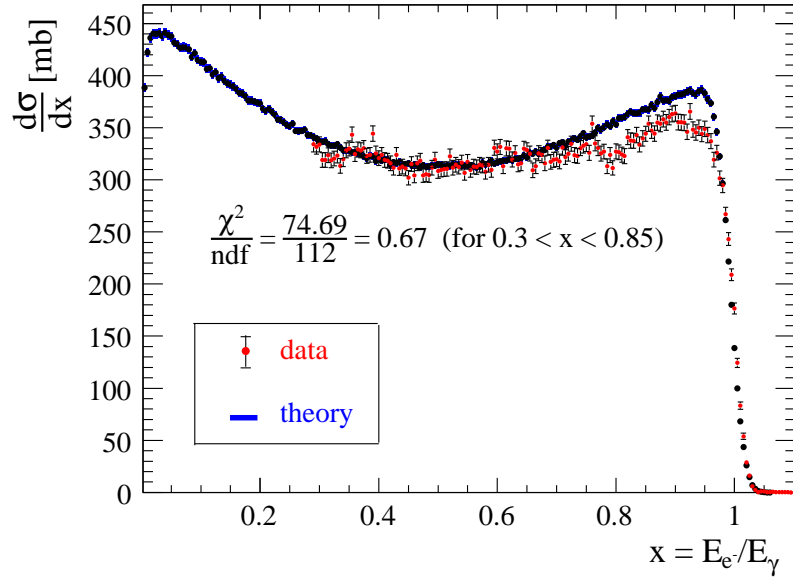


Figure 7.29: Differential cross-section for  $e^+e^-$ -production extracted on electron arm.

To minimize the potential systematic errors, it is preferable to compare the experiment and theory for  $x_{min} < x < x_{max}$  where the effect of the energy losses on the cross-section is less than 5%. The differential cross-section for pair-production, shown in Figures 7.30 - 7.33, extracted on electron as well as on positron arms, demonstrate a sub-percent agreement between the theoretical and experimental values of the cross-section integrated for  $0.4 < x < 0.755$ .

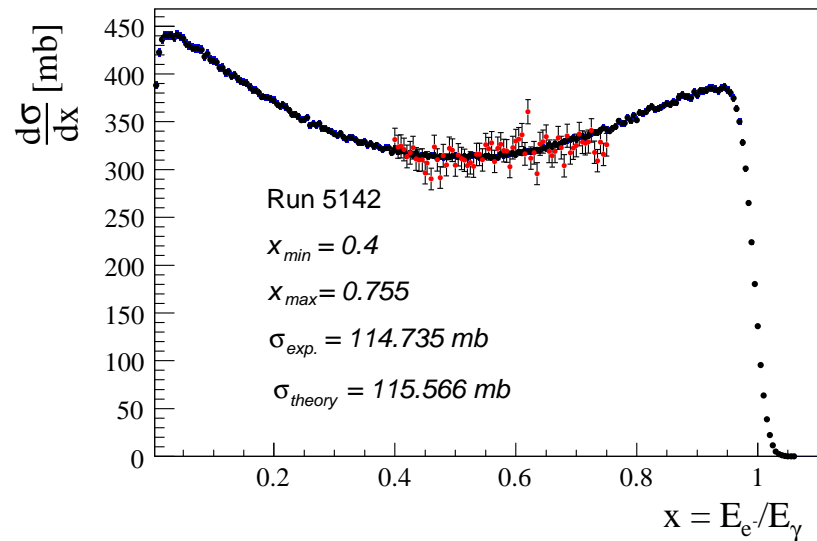


Figure 7.30: Differential cross-section for  $e^+e^-$ -production run #5142 extracted on electron arm.

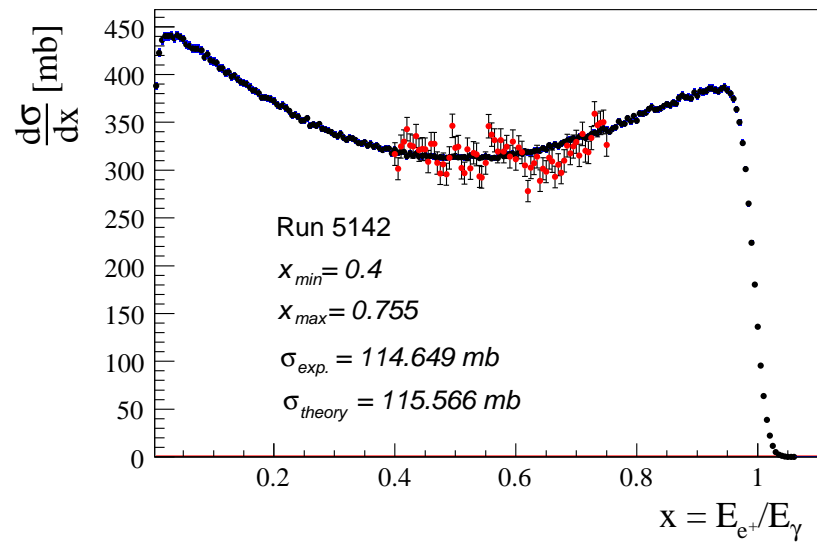


Figure 7.31: Differential cross-section for  $e^+e^-$ -production run #5142 extracted on positron arm.

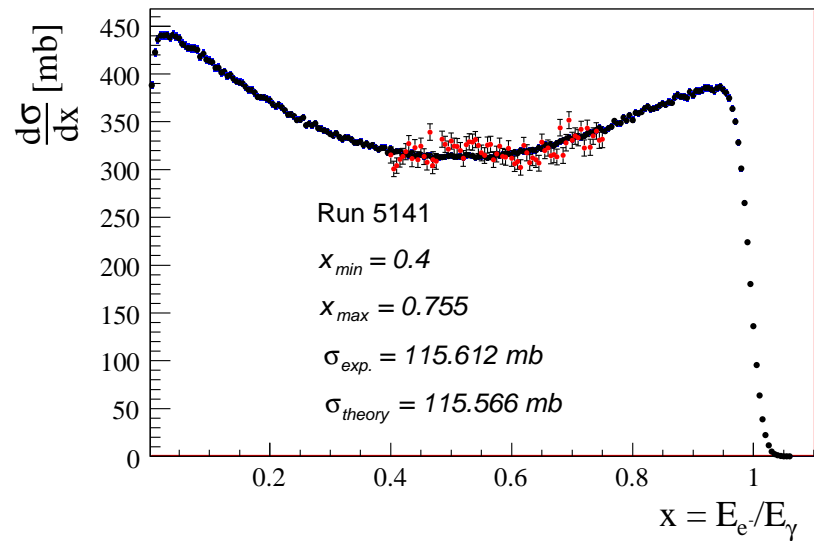


Figure 7.32: Differential cross-section for  $e^+e^-$ -production run #5141 extracted on electron arm.

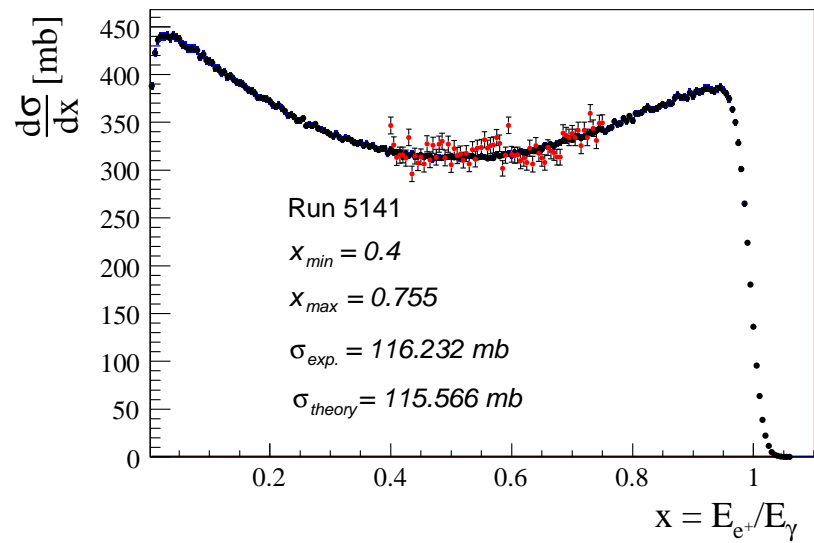


Figure 7.33: Differential cross-section for  $e^+e^-$ -production run #5141 extracted on positron arm.

## 7.8 Error Evaluation and Summary

Table 7.5 lists the theoretical and experimental pair production cross-sections for various runs integrated between  $x_{min}$  and  $x_{max}$ . Where  $x$  is the fraction of energy of the incident photon carried by the electron ( $x = E_{e^-}/E_\gamma$ ).

Table 7.5: Pair production cross-section integrated between  $x_{min}$  and  $x_{max}$ .

Run Number	particle	$x_{min}$	$x_{max}$	$\sigma_{exp}$ (mb)	$\sigma_{theory}$ (mb)	$(1 - \sigma_{exp}/\sigma_{theory})$ (%)
5142	$e^-$	0.3	0.85	181.90	185.75	2.10
5314	$e^-$	0.3	0.85	188.57	185.75	-1.52
5142	$e^-$	0.4	0.85	149.31	152.70	2.22
5314	$e^-$	0.4	0.85	154.71	152.70	-1.32
5141	$e^-$	0.4	0.85	152.28	152.70	0.27
5141	$e^-$	0.4	0.76	115.62	115.57	-0.04
5141	$e^+$	0.4	0.76	116.23	115.57	-0.57
5142	$e^-$	0.4	0.76	115.62	115.57	0.72
5142	$e^+$	0.4	0.76	116.23	115.57	0.80

- Statistical error in the yield.

Table 7.6: Statistical error for the  $e^+e^-$  yields extracted between  $x_{min}$  and  $x_{max}$ .

Run Number	particle	$x_{min}$	$x_{max}$	$dY (\%)$
5142	$e^-$	0.3	0.85	0.21
5314	$e^-$	0.3	0.85	0.24
5142	$e^-$	0.4	0.85	0.23
5314	$e^-$	0.4	0.85	0.27
5141	$e^-$	0.4	0.85	0.27
5141	$e^-$	0.4	0.76	0.30
5141	$e^+$	0.4	0.76	0.30
5142	$e^-$	0.4	0.76	0.44
5142	$e^+$	0.4	0.76	0.44

- Error in the number of carbon atoms per unit area – (0.05%).

The number of atoms per unit area -  $n$  is given by:

$$n = \frac{N_{atoms}}{A} = \frac{\rho \ell}{m} \quad (7.1)$$

where  $A$  is the cross-section of the beam,  $\rho$  is the density of the target material,  $\ell$  is the target thickness and  $m$  is the mass of the atom of the target material. For the carbon target of the PrimEx experiment one has  $\ell = 0.966 \text{ cm} (\pm 0.039\%)$  and  $\rho = 2.198 \text{ g/cm}^3 (\pm 0.014\%)$  [27]. Thus for the carbon target the number of atoms per unit area is  $n_{C^{12}} = 1.066 \times 10^{23} \text{ cm}^{-2} (\pm 0.053\%)$ .

- Error in the photon flux.

For details on error evaluation procedure for photon flux see Sections 6.4 and 6.5. The systematic error in the photon flux determination, arising from the systematic uncertainty in the measurement of the absolute tagging ratios and the uncertainty in electron counting due to beam intensity variations, is 0.97%.

The statistical error on the photon flux, in pair-production data, has a small contribution (0.06%) from error on absolute tagging ratios and is dominated by the electron counting statistics. The combination of both is given in Table 7.7:

Table 7.7: Statistical error on the number of photons for pair-production runs.

Run Number	$N_\gamma$	$dN_\gamma$ (%)
5142	1.19797e+07	0.34
5314	8.62907e+06	0.40
5141	8.59525e+06	0.40

- Error from the background subtraction.

As previously discussed the background from Compton electrons is significant in the region of  $x = E_{e^-}/E_\gamma > 0.9$  (see Figure 7.26). Figure 7.34 shows that the relative contribution of the Compton electrons under the electron arm for  $0.3 < x < 0.85$  is not larger than 0.3%. Hence, a conservative 50% error in determination of the Compton electron background, due to low statistics of generated events, results in 0.15% or less error on the pair-production cross-section.

The background due to Compton photons in the region  $0.3 < x < 0.85$  is completely eliminated by cuts:  $E_{lepton} > 1.2$  GeV and  $|Y_{lepton}| < 5$  cm.

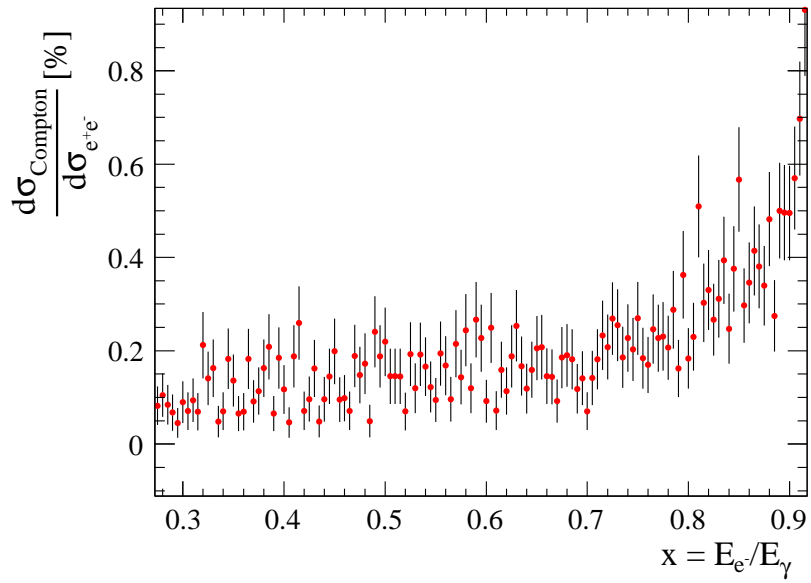


Figure 7.34: Simulated ratio of Compton and pair-production yields for  $0.3 < x < 0.85$ .

- Error from the HyCal resolution.

To study the effect of the HyCal resolution a *GEANT4* simulation was used. The integrated cross-section for pair-production was calculated for  $0.3 < x < 0.85$  while smearing the energy of the particles with a gaussian distribution. The width of the gaussian has been varied between 0.016 and 0.03 in increments of 0.002 to mimic the resolution of the calorimeter (1.6 – 3.0%). As one can see from Table 7.8 the effect of the detector resolution on the cross-section, in the studied region of  $x$ , is less than 0.12%.

Table 7.8: Effect of detector resolution on  $e^+e^-$  cross-section integrated between  $x_{min} = 0.3$  and  $x_{max} = 0.85$ .

Smearing parameter (%)	$\sigma$ (mb)
1.6	185.746
1.8	185.788
2.0	185.856
2.2	185.833
2.4	185.828
2.6	185.841
2.8	185.957
3.0	185.896

- Error from the multi-photon events (see Section 7.4).

The cross-section calculation was repeated for run #5142 accepting only events with one photon reconstructed in the tagger. The photon flux was recalculated ( $N_\gamma = 230001$  and  $dN_\gamma = 0.54\%$ ). The procedure resulted in  $e^+e^-$  cross-section of 182.014 (mb) for  $x_{min} = 0.3$  and  $x_{max} = 0.85$  with a statistical error on the yield of (0.35%). The obtained cross-section is in good agreement (within the statistical errors) with the value listed in Table 7.5. However, to be conservative one can assume an error of 0.06% due to photon reconstruction ambiguity.

- Error from HyCal calibration.

If one assumes that all other effects have been accounted for or they are constant over time, the error on the cross-section, due to drifting detector gains, can be inferred by comparing the cross-sections from various runs integrated between the same values of  $x_{min}$  and  $x_{max}$  (see Table 7.5). Assuming independent errors, one has an upper limit of 1.92% for  $0.3 < x < 0.85$  and an upper limit of 0.53% for  $0.4 < x < 0.76$  for the error due to detector calibration (plus all other time dependent systematic effects).

Tables 7.9 and 7.10 summarizes the errors on the experimental cross-sections listed in Table 7.5.

Table 7.9: Summary of errors integration region  $0.3 < x < 0.85$ .

	Effect	Error (%)
Statistical	Yield statistics	run dependent ( $\sim 0.25$ )
	Photon flux ( $R_{absolute}$ and electron counting)	run dependent ( $\sim 0.37$ )
Systematic	Photon flux ( $R_{absolute}$ and electron counting)	0.97
	Number of Carbon atoms in the target	0.05
	Background subtraction	0.15
	HyCal resolution	0.12
	Photon misidentification/double counting	0.06
	HyCal calibration	$< 1.92$
Total		$\sim \pm 0.44(stat.) \pm 2.16(sys.)$

Table 7.10: Summary of errors for integration region  $0.4 < x < 0.76$ .

	Effect	Error (%)
Statistical	Yield statistics	run dependent ( $\sim 0.44$ )
	Photon flux ( $R_{absolute}$ and electron counting)	run dependent ( $\sim 0.37$ )
Systematic	Photon flux ( $R_{absolute}$ and electron counting)	0.97
	Number of Carbon atoms in the target	0.05
	Background subtraction	0.15
	HyCal resolution	0.12
	Photon misidentification/double counting	0.06
	HyCal calibration	$\sim 0.53$
Total		$\sim \pm 0.58(stat.) \pm 1.13(sys.)$

- Error on the calculated (theoretical) cross-section.

As already mentioned in Section 7.2, the difference in the theoretical value of the cross-section due to the choice of the atomic screening formfactor is on the order of  $\sim 1\%$ .

The experiment is being compared to a theoretical cross-section convoluted with energy losses in the target. *GEANT4* provides an accuracy of  $5 - 10\%$ . To evaluate the effect of this error on the “convoluted theory”, the energy losses in the simulation were artificially varied by  $\pm 10\%$  and the theoretical cross-section was recalculated for region  $0.3 < x < 0.85$  resulting in  $\sim 0.32\%$  difference.

Thus the estimated uncertainty on the theory convoluted with energy losses in the target is  $1.05\%$ .

Given the above considerations, the experimentally obtained cross-section, for  $0.4 < x < 0.76$  is in remarkable agreement with theory.

Copyright © Aram Teymurazyan 2008

## CHAPTER : 8 SUMMARY

The Jefferson Lab Hall-B PrimEx experiment is intended to measure the absolute cross-section for neutral pion photo-production in the Coulomb field of a nucleus, *i.e.* the Primakoff process, with a precision of  $\sim 1.4\%$ . The cross-section measurement enables the extraction of the radiative decay width of the neutral pion (see Equation 1.3), which is predicted by the chiral anomaly and can be calculated exactly in the limit of massless quarks [5] (see Equation 1.2). Recent calculations, considering the real world values of quark masses, in  $\chi$ PT [2], [1] and in QCD sum rule approach [3] predict a neutral pion radiative width of 8.1 eV ( $\pm 1.0\%$ ) and 7.93 eV ( $\pm 1.5\%$ ) respectively. Finally, the fundamental nature of the chiral anomaly in QCD makes the PrimEx experiment arguably one of the most important tests of low energy QCD and  $\chi$ PT possible with a few  $GeV$  photons.

The PrimEx experiment used  $4.9 - 5.5$  GeV photons from the Thomas Jefferson National Accelerator Facility Hall-B photon tagging facility to create  $\pi^0$ s. To achieve its goal of  $\sim 1.4\%$  total error on the neutral pion lifetime measurement the PrimEx experiment requires a knowledge of the absolute normalization, (*i.e.* the photon flux) of the cross-section to 1% or better (see Table 1.1). Such a high precision pushes the limits of the photon tagging technique in regards to the determination of the absolute photon flux.

This dissertation has explored the photon flux determination and monitoring procedure which enabled the determination of the absolute tagged photon flux on the target for the Jefferson Lab Hall-B PrimEx experiment with systematic uncertainty of  $\sim 0.97\%$  (total uncertainty  $\sim 1.0\%$ ).

The photon flux determination for PrimEx experiment involves absolute calibration of the Hall-B tagger with a Total Absorption Counter (see Chapter 4), a novel technique for rate

determination for the tagging counters (see Chapter 6) and monitoring of the relative flux with a newly built Pair Spectrometer (see Chapter 5). A specially designed software package (*PFLUX* – for PrimEx flux) ensures a seamless integration of yield extraction and photon flux determination procedures.

The cross-section normalization procedure for the PrimEx experiment was verified by measuring absolute cross-section for  $e^+e^-$  production with a  $< 2\%$  accuracy (see Tables 7.9 and 7.10), while achieving an agreement with theory at the level of  $< 2\%$  (see Table 7.5).

Here I would also like to summarize in detail the three independent analysis philosophies used by the PrimEx collaboration to extract the neutral pion radiative width. All three methods handle quantities like: the  $\pi^0$  production angle, the invariant mass of two photons from a  $\pi^0$  decay, the elasticity and the HyCal - Tagger coincidence timing in a unique way to obtain distribution of neutral pion yields over  $\pi^0$  production angles in the range  $0 - 3.5^\circ$ . The three analyzes conducted by PrimEx collaboration should be considered quasi-independent since the data sets that they are applied to are greatly overlapping.

To arrive at the four, aforementioned, key concepts used by all three analysis methods one considers following experimentally measured parameters:  $E_{\gamma_0}$  - the energy of incident photon, “tdiff” - the time difference between the HyCal total sum trigger and signal in the Tagger,  $E_{\gamma_1}$ ,  $E_{\gamma_2}$ ,  $(x_1, y_1, z)$  and  $(x_2, y_2, z)$  - the energies and the positions of the two photons from the  $\pi^0$  decay.

- First the data are divided into  $0.01^\circ$  bins of  $\pi^0$  production angle  $\theta_{\pi^0}$ , *i.e.* the angle between  $Z$ -axis and the momentum of the outgoing  $\pi^0$ :

$$\theta_{\pi^0} = \sqrt{\theta_x^2 + \theta_y^2} \quad (8.1)$$

where  $\theta_i = \frac{E_{\gamma_1}i_1 + E_{\gamma_2}i_2}{(E_{\gamma_1} + E_{\gamma_2})z}$  and  $i = x, y$ .

- Then the  $2\gamma$ -invariant mass is constructed for all the possible combinations of cluster pairs reconstructed in HyCal for a given event:

$$m_{2\gamma} = \sqrt{2E_{\gamma_1}E_{\gamma_2}(1 - \cos\theta_{1,2})} \quad (8.2)$$

where  $\theta_{1,2} = \frac{x_1x_2 + y_1y_2 + z^2}{\sqrt{(x_1^2 + y_1^2 + z^2)(x_2^2 + y_2^2 + z^2)}}$  is the angle between the lines connecting the two clusters on the surface of HyCal with the center of the target.

- The elasticity parameter for two clusters is defined as:  $e = \frac{E_{\gamma_1} + E_{\gamma_2}}{E_{\gamma_0}}$ .
- Finally, the HyCal - Tagger coincidence timing is defined in the same way as the “tdiff” spectra in Sections 7.4 and 7.6, *i.e.* the difference in times reconstructed for Tagger and HyCal total sum trigger.

Figure 8.1 shows the correlation between elasticity and the invariant mass for two clusters on the surface of HyCal. In Figure 8.1 one can easily notice a vertical band of inelastic pions and a horizontal band of elastic two cluster events that do not reconstruct to the neutral pion mass. In the world of idealized experimental equipment one would expect to see a tight spot at elasticity 1 and  $m_{2\gamma} \simeq 135$  MeV, but due to finite resolution of the HyCal the spot is transformed into a diagonal line which indicates that if one of the clusters in the pair registers a slightly smaller energy in the calorimeter then the reconstructed  $2\gamma$  invariant mass will also

be slightly less than the tabulated value for  $m_{\pi^0}$  and vice versa a larger energy corresponds to larger invariant mass.

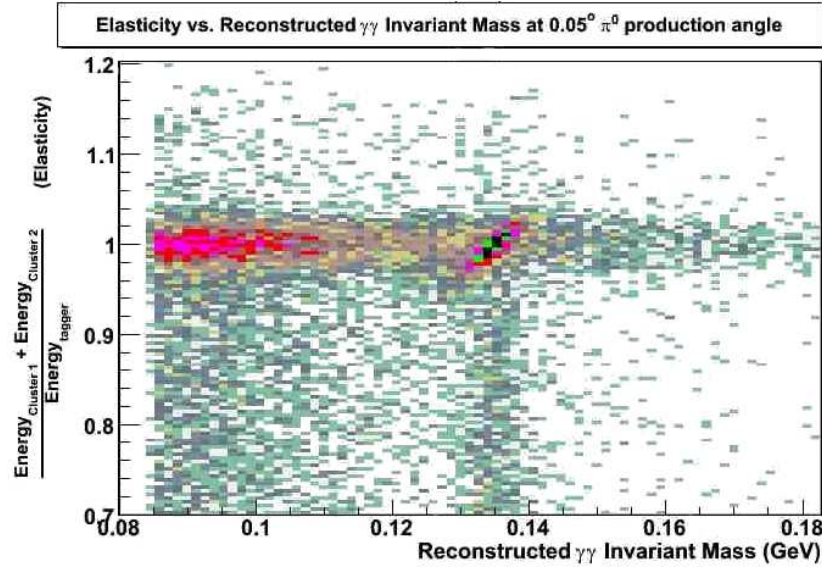


Figure 8.1: The correlation between elasticity and the invariant mass for two clusters on the surface of HyCal at  $\theta_{\pi^0} = 0.05^\circ$ .

A major difference in the analyzes arises from the method each one of them is using to identify the neutral pions, in a given angular bin  $\Delta\theta_{\pi^0}$ , from the pool of multi-hit events recorded in the calorimeter per trigger:

Analysis method 1: To select the combinations of a Tagger photon and a HyCal cluster pair for each trigger, *i.e.* to identify the  $\pi^0$  events, a method of maximum likelihood is used. First the spectra for timing,  $2\gamma$  invariant mass and elasticity are fitted with a signal (a double Gaussian) + background (polynomial) to obtain normalized line-shapes of each of the distributions, which are used as probability distribution functions ( $PDF$ ). Then a “total”  $PDF$  is constructed as product of individual  $PDF$ ’s:  $PDF_{total} = PDF_{timing} \times PDF_{invariantmass} \times$

$PDF_{elasticity}$ . The  $PDF_{total}$  serves as a “Likelihood” function for the event selection. Since each of the line-shapes is normalized, the total probability distribution function can only take values between 0 and 1. By evaluating  $PDF_{total}$  for each possible combination of  $E_{\gamma_0}$ , “tdiff”,  $E_{\gamma_1}$ ,  $E_{\gamma_2}$ ,  $(x_1, y_1, z)$  and  $(x_2, y_2, z)$  the entries with the value of  $PDF_{total}$  closest to 1 are selected. A plot of elasticity - invariant mass dependence is filled using the selected combinations (see Figure 8.1). As a final step towards the  $\pi^0$  yield extraction the entries in the elasticity-mass plot are projected onto an axis perpendicular to the line of correlation between the elasticity and  $2\gamma$ -invariant mass, greatly enhancing the signal to noise ratio. The obtained distribution is used for yield extraction.

Analysis method 2: First, a preselection of cluster pairs in HyCal is performed by requiring a cut  $m_{2\gamma} > 85$  MeV. The analysis showed that 92% of all events that pass the requirement of having at least one cluster pair with invariant mass above 85 MeV have one and only one cluster pair that passes the cut. In case of multiple cluster pairs the one with invariant mass closest to  $m_{\pi^0} \simeq 135$  MeV is picked.

To match the selected cluster pairs with a photon reconstructed in HyCal the “tdiff” spectrum is examined, much like in the case of  $e^+e^-$ -production analysis (see Section 7.4, Figure 7.6), and the photon with “tdiff” closest to the distribution mean within  $\pm 4\sigma$  is selected.

The variables  $E_{\gamma_0}$ , “tdiff”,  $E_{\gamma_1}$ ,  $E_{\gamma_2}$ ,  $(x_1, y_1, z)$  and  $(x_2, y_2, z)$  corresponding to the selected combinations of Tagger photons and HyCal cluster pairs are passed to the next stage of the analysis.

An elasticity cut is used to identify the coherent pion production channels. To account for possible accidental timing coincidences between cluster pairs in HyCal and photons registered

in the Tagger the elasticity spectrum of out-of-time events is studied and subtracted bin-by-bin with an appropriate scaling factor. The resulting distribution is fitted with a signal (double Gaussian) + background (3rd order polynomial) function and the number of entries in the peak is regarded as the number of elastic  $\pi^0$ 's. This procedure is repeated for each of the bins in invariant mass spectrum resulting in a invariant mass spectrum of elastic events.

Finally, the  $2\gamma$  invariant mass spectrum of the elastic events is fitted with a signal (double Gaussian) + background (3rd order polynomial) function and the integral number under the peak is regarded as the final number of elastic neutral pions (for a particular angle).

It is worth noting that this procedure is very lengthy and tedious and depending on the number of bins in each spectrum may, require that  $\sim 2 \times 10^3$  fits are performed.

Analysis method 3: The HyCal cluster pairs are preselected for each trigger event by requiring a cut  $m_{2\gamma} > 90$  MeV. All possible cluster pairs above the 90 MeV threshold are considered to be  $\pi^0$  candidates. To identify the corresponding photon from the number hits reconstructed in the Tagger, a  $\pm 4$  ns window is set up around the mean value of the “tdiff” distribution and the photon with “tdiff” value closest to the mean is selected.

The energy information of the selected HyCal cluster pairs and the Tagger photons are used in kinematic fitting to the energy conservation condition  $E_{\gamma_0} = E'_{\gamma_1} + E'_{\gamma_2}$ , where  $E'_{\gamma_1}$  and  $E'_{\gamma_2}$  are the corrected energies of the clusters registered in HyCal:

$$E'_{\gamma_i} = E_{\gamma_i} + \Delta E_{\gamma_i} \quad (8.3)$$

where  $i = 1, 2$  and  $\frac{\Delta E_{\gamma_1}}{\Delta E_{\gamma_2}} = \frac{E_{\gamma_1}}{E_{\gamma_2}}$ .

The number of  $\pi^0$  events is obtained by fitting the  $2\gamma$  invariant mass distribution constructed using the corrected cluster energies.

Each of the three methods is repeated for every  $\pi^0$  production angular bin  $\Delta\theta_{\pi^0}$  to obtain the angular distribution of  $\pi^0$ .

As an example the experimental yields obtained using the second method are shown in Figure 8.2 as a function of the pion-production angle [40].

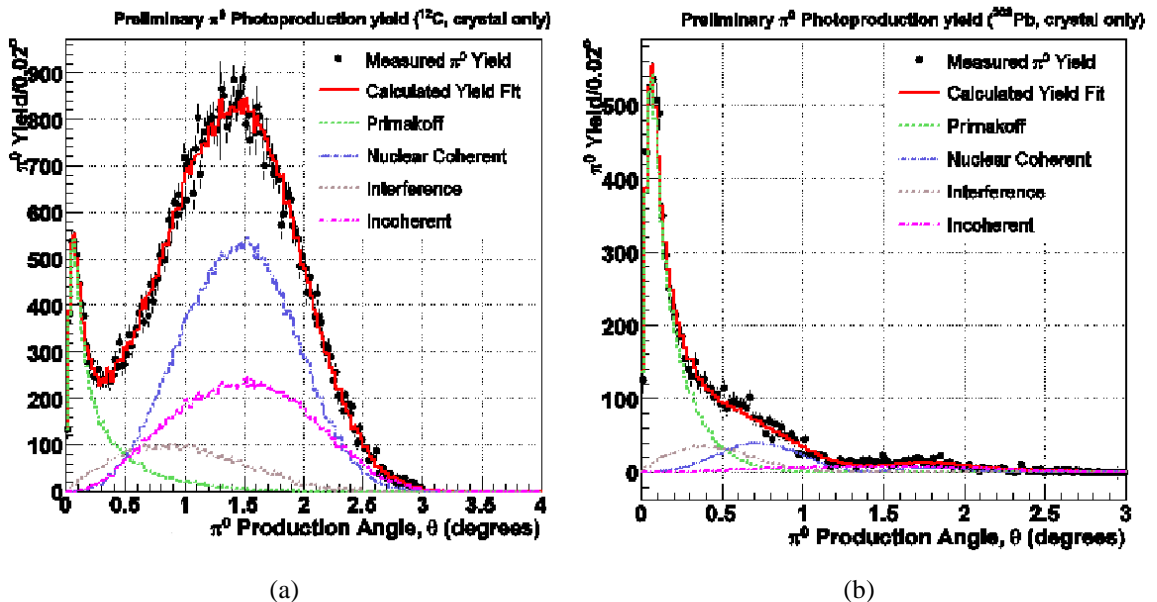


Figure 8.2: Pion photo-production yield as a function of production angle: on (a) carbon target and (b) lead target.

By normalizing the tagged  $\pi^0$  yields, extracted in the PrimEx experiment, to the tagged photon flux according to Equation 3.1 a pion photo-production cross-section is obtained.

The preliminary result of the PrimEx experiment for the  $\pi^0$  radiative width is:  $\Gamma_{\pi^0 \rightarrow \gamma\gamma} = 7.93 \text{ eV} \pm 2.1\%(\text{stat.}) \pm 2.0\%(\text{sys.})$ . It is in good agreement with current state of the art theoretical predictions and with the world average ( $7.84 \text{ eV} \pm 7.1\%$ ). The collaboration is

continuing the effort in order to further understand contributions from various physics backgrounds (see Section 1.4) and reduce the systematic errors.

Copyright © Aram Teymurazyan 2008

## APPENDIX : A ERROR PROPAGATION FOR A RATIO OF CORRELATED NUMBERS

In Equations 3.2 and 3.4 for the absolute and relative tagging ratios introduced in Chapter 3, the numerator is a subset of the denominator. Thus, the two numbers are correlated and the ordinary equations for the uncertainty in a ratio cannot be applied.

To make the following discussion more general, let us introduce the terms hit, miss and total number of trials. In our particular case hits would be the number of  $\gamma \cdot e$  (or  $e^+e^- \cdot e$ ) coincidences, misses would be the number of electrons in the tagger that did not have a partner photon (or  $e^+e^-$  pair) in the TAC (or Pair Spectrometer). If we denote the number of hits  $a$  and the number of misses  $b$  the total number of trials will be  $a + b$ . Using these definitions, the tagging ratio can be presented in the following form:

$$R = \frac{a}{a + b} = \frac{1}{1 + b/a} \quad (\text{A.1})$$

where the number of "hits"  $a = R(a + b)$  and the number of "misses"  $b = (1 - R)(a + b)$

Note that "hits" and "misses" are mutually exclusive classes of events and thus  $a$  and  $b$  are uncorrelated, so their uncertainties can be propagated in a straightforward way.

From the definition of  $R$ , it follows that its partial derivatives with respect to  $a$  and  $b$  will be:

$$\frac{\partial R}{\partial a} = \frac{b}{(a + b)^2} \quad \text{and} \quad \frac{\partial R}{\partial b} = -\frac{a}{(a + b)^2} \quad (\text{A.2})$$

Let  $da$  and  $db$  be the uncertainties in  $a$  and  $b$ . Then in general:

$$dR = \sqrt{\left(\frac{\partial R}{\partial a}da\right)^2 + \left(\frac{\partial R}{\partial b}db\right)^2} = \frac{1}{(a + b)^2} \sqrt{b^2(da)^2 + a^2(db)^2} \quad (\text{A.3})$$

Assuming  $a$  and  $b$  follow Poisson statistics, we set  $da = \sqrt{a}$  and  $db = \sqrt{b}$ . Then Equation A.3 yields:

$$dR = \frac{1}{(a+b)^2} \sqrt{b^2a + a^2b} = \sqrt{R \frac{1-R}{a+b}} \quad (\text{A.4})$$

By examining the two extreme cases of  $\frac{b}{a} \ll 1$  and  $\frac{b}{a} \gg 1$  we get:

$$\text{First case } \frac{b}{a} \ll 1 \implies R = \frac{1}{1+b/a} \sim 1 \implies dR \sim \sqrt{\frac{1-R}{a+b}}$$

$$dR \sim \frac{\sqrt{b}}{a+b} \quad (\text{A.5})$$

$$\text{Second case } \frac{b}{a} \gg 1 \implies 1-R = \frac{1}{1+a/b} \sim 1 \implies dR \sim \sqrt{\frac{R}{a+b}}$$

$$dR \sim \frac{\sqrt{a}}{a+b} \quad (\text{A.6})$$

The first case when the number of hits is far greater than the number of misses is relevant for the case of absolute tagging ratio where a typical tagging efficiency is 95% or more. The second case where the number of hits is much less than the number of misses is relevant when dealing with relative tagging ratio where only 0.5% of photons are tagged by the PS.

## APPENDIX : B WEIGHTED AVERAGE

Here for reference purposes I want to bring the formulas for weighted mean and the error in the weighted mean. The derivation of the equations can be found in any standard text book for error analysis, for example [41].

Having a set of measurements  $x_i$  for an observable  $x$  and each of them having an error  $dx_i$  the weighted mean and its error are given by:

$$x_{average} = \frac{\sum x_i / (dx_i)^2}{\sum 1 / (dx_i)^2} = \sum w_i \cdot x_i \quad (B.1)$$

where  $w_i = \frac{1 / (dx_i)^2}{\sum 1 / (dx_i)^2}$ .

$$dx_{average}^2 = \frac{1}{\sum 1 / (dx_i)^2} \quad (B.2)$$

## APPENDIX : C DAQ ELECTRONICS AND TRIGGER SETUP

### C.1 Lecroy 1877 multi-hit TDC

For quick reference I am listing some of technical characteristics of Lecroy 1877 TDC modules that were used through PrimEx run. For the complete list specifications please refer to the 1877 data sheet [42].

- 96 ECL differential input channels per module. Minimum pulse width  $10\text{nsec}$  FWHM (must be greater than 1 time bin width)
- Least Significant Bit (LSB) of 500 ps
- Full Scale from 0 to  $32.768\ \mu\text{s} \pm 0.0025\%$ ; programmable in steps of 8 ns
- Maximum differential non-linearity  $\pm 0.2$  LSB (typical)
- Full scale integral non-linearity less than 25 ppm
- Conversion time of 800 ns per hit within the programmed full scale;  $1.6\ \mu\text{s}$  minimum
- Ability to record timing information for rising and/or falling edges
- Can measure two edges separated by as little as 10 ns. No two pulse edges should be closer than 10 ns. This implies a lower limit on the double pulse resolution of 20 ns
- Can operate in either Common Start or Common Stop mode; for PrimEx the TDC were operating in Common Stop mode which allows to save on delay cable costs
- Has a programmable LIFO memory of up to 16 hits per channel per event

## APPENDIX : D LIVE2/LIVE1 PROBLEM

Analysis showed that the values of  $Live1$  and  $Live2$  (gated and ungated scalers driven by  $200kHz$  clocks) recorded in the data are compromised due to a hardware design flaw.

From time to time the value of  $Live2$  jumps by  $2^{16}$  or by  $2^{24}$  or by  $2^{16} + 2^{24}$  and then it self corrects. The simplest way to correct this is to look at the difference in  $Live2$  for two adjacent events and subtract the corresponding number.

In addition to the anomaly described above  $Live1$  goes through jumps of  $2^8$ . This anomaly is cumulative and doesn't correct itself over time. To correct the value of  $Live1$  we again look at the difference  $Live1_i - Live1_{i-1}$  and make sure that it satisfies the following criteria: 1) It is smaller than  $Live2_i - Live2_{i-1}$ , 2) It is positive. And also we require that  $Live1 < Live2$ .

If any of this conditions is not satisfied we subtract or add  $2^8 = 256$  until all 3 criteria are satisfied.

It has been shown that to a very good approximation ( $\sim 0.02\%$ ) one can assume that the data acquisition has a fixed dead time of 4.9 scaler counts per event ( $\sim 25\mu s$ ). Then the value of  $Live1$  can be calculated if one knows the value of  $Live2$ :

$$Live1_i = Live1_{i-1} + Live2_i - Live2_{i-1} - 4.9 \text{ (algorithm suggested by Eric Clinton).}$$

or

$Live1_i = Live2_i - n \times 4.9$  where  $n$  is the number of events. All three methods agree within  $\sim 0.02\%$ .

## APPENDIX : E PFLUX PACKAGE, WHAT IT CAN DO AND HOW TO USE IT

To link the data analysis and the photon flux calculation the “PFLUX” package was created<sup>1</sup>.

The “PFLUX” package uses the information about 5-second intervals of a run which is stored in *MySql* database. The information for each interval is loaded into a “C” structure:

```
typedef struct{
    int run;
    int interval_id;
    int start_event;
    int end_event;
    unsigned int d_live1;
    unsigned int d_live2;
    int n_trigs;
    int tdc_window;
    int n_e[MAX_TCH];
    INTERVAL_STATUS_t status;
    bool analyzed;
    float fraction;
    unsigned int first_time;
    unsigned int last_time;
}interval_info_t;
```

where `#define MAX_TCH 61` – is the number of T-counters, `INTERVAL_STATUS_t status` – is a “C” enum with possible values of “GOOD”, “BAD” and “UNKNOWN”:

```
enum INTERVAL_STATUS_t{
    GOOD,
    BAD,
    UNKNOWN
};
```

---

<sup>1</sup>The text in Appendix E assumes basic knowledge of “C” and “C++” programming languages

*unsigned int first\_time* – is the value recorded by the ungated scaler for the start event of the interval, *unsigned int last\_time* – is the value recorded by the ungated scaler for the current event of the interval, *bool analyzed* – is true if at least one event in the interval is analyzed and *float fraction* – is the fraction of the time length of the interval that has been analyzed. If for any reason only a part of an interval is analyzed this variable is used to scale the flux of the interval accordingly. The rest of the variable names are self-explanatory.

As any part of PrimEx software PFLUX package consists of four main functions:

```
void pflux_init(void);

void pflux_brun(int RunNumber, Banks_t *banks);

INTERVAL_STATUS_t pflux_evnt(Banks_t *banks);

void pflux_erun(Banks_t *banks);

extern Pflux* pflux;

extern Pflux* ClockFlux;

extern Pflux* OutOfTimeFlux;
```

The back-bone of PFLUX package is the Pflux class:

```
class Pflux{

private:

    interval_info_t element;
    VIntervalInfo_t v_interval_info;
    tagging_ratio_t tagging_ratio;
    ETij_t ETij[MAX_TCH];
    Banks_t *b;
    MYSQL *mysql_handle_ptr;
    bool loaded_interval_info;
    bool loaded_et_fractions;
```

```

float livetime_sigma;
int rate_beam_trip;
int num_bad;
int leakage_corr;
char flux_table_name[150];
int run_number;

public:
Pflux(Banks_t *banks, const char* table_name);
virtual  $\tilde{P}$ flux(){};  

bool LoadIntervalInfo(int RunNumber);
bool GetLoadStatus();
bool LoadETFractions();
bool GetETLoadStatus();
void SetIntervalStatus();
INTERVAL_STATUS_t GetStatus();
Eflux_t GetEFlux();
flux_t CorrectLeakage(flux_t f);
flux_t GetFlux();
VIntervalInfo_t GetIntervalInfoVector();
};

```

where `VIntervalInfo_t v_interval_info` – is a vector of type “`typedef std::vector<interval_info_t> VIntervalInfo_t`” holding the information about 5-second intervals into which the run was divided.

```

#define MAX_ECH 767
typedef struct{
    double ratio[61];
    double error[61];

```

```

}tagging_ratio_t;

typedef struct{
    double Aij[MAX_ECH];
    double d_Aij[MAX_ECH];
}ETij_t;

typedef struct{
    double flux_i[MAX_TCH];
    double flux_i_err[MAX_TCH];
    double TotalFlux;
    double TotalFlux_Err;
}flux_t;

typedef struct{
    double flux_i[MAX_ECH];
    double flux_i_err[MAX_ECH];
    double TotalFlux;
    double TotalFlux_Err;
}Eflux_t;

```

The PFLUX package is managed via a standard PrimEx configuration file (*ascii* XML file) of form:

```

<?xml version="1.0"?>
<pconfig>
<beam_trip>1</beam_trip>
<livetime_sigma>3.0</livetime_sigma>
<num_bad>2</num_bad>
<leakage_corr>1</leakage_corr>
<flux_output>1</flux_output>
<Eflux_output>1</Eflux_output>

```

`</pconfig>`

The *beam\_trip*, *leakage\_corr*, *flux\_output* and *Eflux\_output* are flags.

To disable a functionality of a *PFLUX* package one needs to set the respective flag to

0. By default the package will try to determine the data regions corresponding to beam trips and cut them out. To disable this feature the *beam\_trip* variable has to be set to 0 in the configuration file. It is also possible to set the number of intervals to be cut out after each beam trip by changing the *num\_bad* variable. Keep in mind that each interval is 5 seconds.

## APPENDIX : F SYSTEMATIC ERRORS DUE TO BEAM INSTABILITY

Using a sampling technique for detector rate determination can lead to overcounting if sampling times are correlated with the source intensity. More specifically, if the trigger rate is beam dependent, the number of samples taken per unit time will then also be beam dependent. Thus, if we have more samples at high rates than at low rates, the average rate we calculate will be higher than the true average.

This effect can be evaluated for some cases of simple models of beam intensity variation.

Assuming hits in the tagger are dominated by good electrons, the tagger rates will increase linearly with the beam current:

$$R_{det} \propto I_{beam} \quad (\text{F.1})$$

The main PrimEx trigger is formed by a coincidence of Tagger and HyCal signals and since the HyCal rate itself is proportional to the beam intensity the HyCal-Tagger coincidence rate will be proportional to the  $I_{beam}^2$ :

$$R_{trigger} \propto I_{beam}^2 \quad (\text{F.2})$$

The number of hits a detector sees over the course of the run will then be:

$$N_{hits} = \int_0^T w R_{det} R_{trigger} dt = C \int_0^T I_{beam}^3 dt \quad (\text{F.3})$$

where  $w$  is the out of time window width and  $T$  is the total live-time of the run.  $C$  is a proportionality constant which includes  $w$ .

Beam Current Oscillation: Assume a beam current of the form  $I_{beam} = I_o \pm \alpha \sin \omega t$ . The frequency  $\omega$  is assumed to be large enough that many oscillations occur over the course of a run yet small enough that the rate is essentially constant over the sampling window ( $7\mu\text{s}$  for PrimEx).

Integration yields:

$$N_{hits} = CT \left( I_o^3 + \frac{3}{2} I_o \alpha^2 \right) \quad (\text{F.4})$$

The first term gives the number of hits which would be recorded for the case when  $\alpha = 0$ .

The fractional increase in the number of hits recorded is then given by:

$$\frac{N_{hits}^{measured} - N_{hits}^{actual}}{N_{hits}^{actual}} = \frac{3}{2} \left( \frac{\alpha}{I_o} \right)^2 \quad (\text{F.5})$$

Take, for example, the case when  $\alpha$  is 10% of  $I_o$ . The number of hits recorded will be increased by  $3/2(0.10I_o/I_o)^2 = 0.015$  or 1.5%.

Beam Current Drift: Occasionally, a very slow drift can be observed in the beam current that becomes significant over time. Assuming a beam current of the form  $I_{beam} = I_o \pm \beta t$ , the above calculation can be repeated for an integration period of  $-T/2$  to  $T/2$  yielding:

$$N_{hits} = CT \left( I_o^3 + \frac{1}{4} \beta^2 I_o T^2 \right) \quad (\text{F.6})$$

The fractional increase in the number of hits due to beam drift is then given by:

$$\frac{N_{hits}^{measured} - N_{hits}^{actual}}{N_{hits}^{actual}} = \frac{1}{4} \left( \frac{\beta T}{I_o} \right)^2 \quad (\text{F.7})$$

As an example, consider a period for which the beam drifted down/up by 10% before it was corrected. The number of recorded hits will be overcounted by  $\frac{1}{4}(0.10I_o/I_o)^2 = 0.0025$  or  $\sim 0.25\%$ .

## APPENDIX : G PAIR-PRODUCTION RUN SUMMARY

Table G.1: List of pair-production data runs.

Run Number	PS dipole current	PS dipole field	$E_{e^\pm}$ min.	$X_{e^\pm}$ min.
5141	400 Amps	0.293 Tesla $\times$ m	1.695 GeV	35.09 cm
5142	300 Amps	0.220 Tesla $\times$ m	1.272 GeV	35.05 cm
5314	300 Amps	0.220 Tesla $\times$ m	1.272 GeV	35.05 cm

Table G.2: Photon flux per energy bin for run # 5142.

Bin ID	$N_\gamma$	$dN_\gamma$ % stat.
1	1.00912e+06	1.15677
2	1.34007e+06	1.01321
3	1.21228e+06	1.06531
4	1.27925e+06	1.0794
5	1.20561e+06	1.12393
6	1.27202e+06	1.09326
7	1.20309e+06	1.10741
8	1.23055e+06	0.936823
9	1.14727e+06	1.00236
10	1.08047e+06	1.07486

Table G.3: Photon flux per energy bin for run # 5314.

Bin ID	$N_\gamma$	$dN_\gamma$ % stat.
1	749503	1.35845
2	898607	1.24468
3	895686	1.25398
4	964175	1.25614
5	913906	1.30781
6	892976	1.3121
7	904427	1.29246
8	895388	1.11379
9	796927	1.21291
10	717473	1.32302

Table G.4: Photon flux per energy bin for run # 5141.

Bin ID	$N_\gamma$	$dN_\gamma$ % stat.
1	709491	1.3778
2	906463	1.22736
3	913135	1.2328
4	935250	1.25878
5	882046	1.31909
6	884500	1.3082
7	907838	1.2776
8	880465	1.10602
9	845264	1.16828
10	730794	1.29755

## BIBLIOGRAPHY

- [1] J. L. Goity, A. M. Bernstein, and B. R. Holstein, “The decay  $\pi^0 \rightarrow \gamma\gamma$  to next to leading order in chiral perturbation theory,” *Phys. Rev.*, vol. D66, pp. 076014, 2002.
- [2] B. Moussallam, “Chiral sum rules for  $L_{(6)}^{WZ}$  parameters and its application to  $\pi^0, \eta, \eta'$  decays,” *Phys. Rev. D*, vol. 51, no. 9, pp. 4939–4949, May 1995.
- [3] B. L. Ioffe and A. G. Oganessian, “Axial anomaly and the precise value of the  $\pi^0 \rightarrow 2\gamma$  decay width,” *Phys. Lett.*, vol. B647, pp. 389–393, 2007.
- [4] H. Primakoff, “Photo-Production of Neutral Mesons in Nuclear Electric Fields and the Mean Life of the Neutral Meson,” *Phys. Rev.*, vol. 81, no. 5, pp. 899, Mar 1951.
- [5] J. F. Donoghue, E. Golowich, and B. R. Holstein, “Dynamics of the standard Model,” 1992.
- [6] J. S. Bell and R. Jackiw, “A PCAC puzzle:  $\pi^0 \rightarrow \gamma\gamma$  in the sigma model,” *Nuovo Cim.*, vol. A60, pp. 47–61, 1969.
- [7] Stephen L. Adler, “Axial vector vertex in spinor electrodynamics,” *Phys. Rev.*, vol. 177, pp. 2426–2438, 1969.
- [8] Barry R. Holstein, “Chiral Perturbation Theory: a Primer,” 1995.
- [9] Johan Bijnens, Albert Bramon, and Fernando Cornet, “Pseudoscalar Decays into Two Photons in Chiral Perturbation Theory,” *Phys. Rev. Lett.*, vol. 61, no. 13, pp. 1453–1456, Sep 1988.

[10] John F. Donoghue, B. R. Holstein, and Y. C. Lin, “The reaction  $\gamma\gamma \rightarrow \pi^0\pi^0$  and chiral loops,” *Phys. Rev. D*, vol. 37, no. 9, pp. 2423–2430, May 1988.

[11] R. M. et. al. Barnett, “Review of Particle Physics,” *Phys. Rev. D*, vol. 54, no. 1, pp. 1–708, Jul 1996.

[12] H. W. Atherton et al., “Direct measurement of the lifetime of the neutral pion,” *Phys. Lett.*, vol. B158, pp. 81–84, 1985.

[13] A. Browman et al., ,” *Phys. Rev. Lett.*, vol. 33, pp. 1400, 1974.

[14] G. Bellettini et al., ,” *Il Nuovo Cimento*, vol. 66, no. 1, pp. 243, 1970.

[15] Kryshkin et al., ,” *Sov. Phys.*, vol. 40, no. 6, pp. 1037, 1970.

[16] G. von Dardel et al., “Mean life of the neutral pion,” *Phys. Lett.*, vol. 4, no. 1, pp. 51, 1963.

[17] D. A. et. al. Williams, “Formation of the pseudoscalars  $\pi^0$ ,  $\eta$ , and  $\eta'$  in the reaction  $\gamma\gamma \rightarrow \gamma\gamma$ ,” *Phys. Rev. D*, vol. 38, no. 5, pp. 1365–1376, Sep 1988.

[18] G. Bellettini et al., ,” *Il Nuovo Cimento*, vol. 40, no. 4, pp. 1139, 1965.

[19] A. M. Bernstein, “Measurements of pion properties and production amplitudes: Probing confinement scale QCD,” *Nucl. Phys.*, vol. A623, pp. 178c–188c, 1997.

[20] PrimEx Collaboration, “Proposal,” , no. 1, December 1998.

[21] S. Gevorkyan et. al., “Photoproduction of  $\pi^0$  messons off nuclei,” [http://www.jlab.org/primex/primex\\_notes/pr.pdf](http://www.jlab.org/primex/primex_notes/pr.pdf), June 2007.

[22] S. Gevorkyan *et. al.*, “ $\pi^0$  photoproduction off light nuclei,” [http://www.jlab.org/primex/primex\\_notes/light.pdf](http://www.jlab.org/primex/primex_notes/light.pdf), July 2007.

[23] S. Gevorkyan *et. al.*, “Incoherent Photoproduction of  $\pi^0$  Messons off Nuclei,” [http://www.jlab.org/primex/primex\\_notes/inc.pdf](http://www.jlab.org/primex/primex_notes/inc.pdf), August 2007.

[24] K. Gottfried and D. R. Yennie, “Vector mesons and nuclear optics,” *Phys. Rev.*, vol. 182, pp. 1595–1601, 1969.

[25] D. I. Sober et al., “The bremsstrahlung tagged photon beam in Hall B at JLab,” *Nucl. Instrum. Meth.*, vol. A440, pp. 263–284, 2000.

[26] H. Bethe and W. Heitler, “On the Stopping of fast particles and on the creation of positive electrons,” *Proc. Roy. Soc. Lond.*, vol. A146, pp. 83–112, 1934.

[27] R. Miskimen P. Martel, “Analysis of PrimEx targets,” , no. 28, Nov 2004.

[28] V. Batarin *et. al.*, “Precision Measurement of Energy and Position Resolutions of the BTeV Electromagnetic Calorimeter Prototype,” *NIM. A*, vol. 510, pp. 248, 2003.

[29] JLab Data Acquisition Group, “CODA User’s manual,” [http://coda.jlab.org/user\\_guid.htm](http://coda.jlab.org/user_guid.htm).

[30] P. Ambrozewicz, “Beam Quality Study,” [http://www.jlab.org/primex/primex\\_notes/beam-quality/pnote.pdf](http://www.jlab.org/primex/primex_notes/beam-quality/pnote.pdf), March 2007.

[31] A. Korchin, “Electron-positron production in kinematics conditions of PrimEx,” Private communications, August 2006.

[32] G. Moliere, ,” *Z. Naturforsch*, vol. A 2, pp. 133, 1947.

[33] Yung-Su Tsai, “Pair Production and Bremsstrahlung of Charged Leptons,” *Rev. Mod. Phys.*, vol. 46, pp. 815, 1974.

[34] H.-J. Werner, P. J. Knowles, R. Lindh, F. R. Manby, M. Schütz, P. Celani, T. Korona, G. Rauhut, R. D. Amos, A. Bernhardsson, A. Berning, D. L. Cooper, M. J. O. Deegan, A. J. Dobbyn, F. Eckert, C. Hampel, G. Hetzer, A. W. Lloyd, S. J. McNicholas, W. Meyer, M. E. Mura, A. Nicklass, P. Palmieri, R. Pitzer, U. Schumann, H. Stoll, A. J. Stone, R. Tarroni, and T. Thorsteinsson, “MOLPRO, version 2006.1, a package of ab initio programs,” 2006, see <http://www.molpro.net>.

[35] H. Davies, H. A. Bethe, and L.C. Maximon, ,” *Phys. Rev.*, vol. 93, pp. 788, 1954.

[36] “PrimEx data bank definitions,” <http://clasweb.jlab.org/cgi-bin/cvsweb/cvsweb.cgi/src/libraries/include/bankdef.xml?cvsroot=PrimEx>.

[37] Liyan Jiang, “Event Configuration of PrimEx Data,” , no. 49, August 2007.

[38] Geant4 Collaboration, “Physics Reference Manual,” <http://geant4.web.cern.ch/geant4/UserDocumentation/UsersGuides/PhysicsReferenceManual/html/PhysicsReferenceManual.html>.

[39] Geant4 Collaboration, “User Guides for Application Developer,” [http://geant4.web.cern.ch/geant4/UserDocumentation/UsersGuides/ForApplicationDeveloper/html/ch05s02.html#programlist\\_PhysProc\\_1](http://geant4.web.cern.ch/geant4/UserDocumentation/UsersGuides/ForApplicationDeveloper/html/ch05s02.html#programlist_PhysProc_1).

[40] D. McNulty, “ $\pi^0$  Cross Section analysis: Methods and Results,” Unpublished, July 2007.

[41] Philip R. Bevington and D. Keith Robinson, *Data Reduction and Error Analysis for the Physical Sciences*, McGraw-Hill, New York, 2nd Edition, 1992.

[42] LeCroy Corporation, “1877 Multihit Time-to-Digital Converter,”  
<http://www.lecroy.com/lrs/dsheets/1877.htm>.

**Full Name**

Aram Teymurazyan

[REDACTED]

[REDACTED]

[REDACTED]

[REDACTED]

**Education**

B.S. in Physics, with honors, Yerevan State University, Armenia, (2000)  
M.S. in Physics, University of Kentucky, USA, (2005)  
Ph.D. in Physics, University of Kentucky, USA (in progress)

**Awards, Honors and Professional Society Memberships**

Academic Excellency Award, Yerevan State University (1999)  
National Nuclear Physics Summer School scholarship (2005)  
Member of American Physical Society (2003)

**Professional Schools**

“National Nuclear Physics Summer School 2005”, June 6-17, Berkeley, CA, (2005)  
“Geant4 Tutorial at JLab”, May 22-26, Jefferson Lab, Newport News, VA, (2006)

**Positions**

April 2001 - December 2007	Research Assistant, Department of Physics and Astronomy, University of Kentucky
December 2007 - Present	Postdoctoral Research Associate, Department of Physics, University of Massachusetts, Amherst

**Publications**

1. “Light ray displacements due to air temperature gradient”, A.A. Grigoryan and A. Teymurazyan, ALICE Internal Note, ALICE-INT-2000-13, CERN, (2000).
2. “Search for  $\Theta^+(1540)$  pentaquark in high statistics measurement of  $\gamma p \rightarrow K^0 K^+ n$  at CLAS”, M. Battaglieri et al., Phys.Rev.Lett.96:042001, (2006).
3. “Search for the  $\Theta^+$  pentaquark in the reaction  $\gamma d \rightarrow p K^- K^+ n$ ”, B. McKinnon et al., Phys.Rev.Lett.96:212001, (2006).

4. “Search for  $\Theta^{++}$  pentaquarks in the exclusive reaction  $\gamma p \rightarrow K^+ K^- p$ ”, V. Kubarovskiy et al., Phys.Rev.Lett.97:102001, (2006).
5. “Search for the  $\Theta^+$  pentaquark in the reactions  $\gamma p \rightarrow K^0 K^+ n$  and  $\gamma p \rightarrow K^0 K^0 p$ ”, R. De Vita et al., Phys.Rev.D74:032001, (2006).
6. “Energy calibration of the JLab bremsstrahlung tagging system”, S. Stepanyan, S. Bo- yarinov, H. Egiyan, L. Guo, D. Dale, M. Gabrielyan, L. Gan, A. Gasparian, A. Glamazdin, B. Mecking, I. Nakagawa, A. Teymurazyan, M.H. Wood, NIM, Section A: Accelerators, Spectrometers, Detectors and Associated Equipment, Volume 572, Issue 2, 11 March, Pages 654-661, (2007).

### Contributed Abstracts and Conference talks

1. “High Precision Photon Flux Control with the PrimEx Pair Spectrometer”, Aram Tey- murazyan, PrimEx Collaboration, DNP03 Meeting of the American Physical Society, Tucson, Arizona (2003).
2. “Precision Photon Flux Determination for the Jefferson Lab PrimEx Experiment”, Aram Teymurazyan, PrimEx Collaboration, 2nd Joint Meeting of the Nuclear Physics Divisions of the APS and The Physical Society of Japan September 18-22, Maui, Hawaii (2005).
3. “A Precision Measurement of the Pair Production Cross Section in the Jefferson Lab PrimEx Experiment”, Aram Teymurazyan, PrimEx Collaboration, DNP06 Meeting of the American Physical Society, Nashville, Tennessee (2006).
4. “A Precision Measurement of the Pair Production Cross Section in the Jefferson Lab PrimEx Experiment”, Aram Teymurazyan, PrimEx Collaboration, Anual April Meeting of the American Physical Society, Jacksonville, Florida (2007).

---

Aram Teymurazyan

---

Date